EUV Microscopy with a Tabletop High Harmonic Generation Source: Generalizing Coherent Diffractive Imaging to Extended Samples in Transmission, Reflection, and Hyperspectral Modalities

by

Bosheng Zhang

B.S., University of Science and Technology of China, 2007

A thesis submitted to the

Faculty of the Graduate School of the

University of Colorado in partial fulfillment

of the requirements for the degree of

Doctor of Philosophy

Department of Physics

2015

This thesis entitled:
EUV Microscopy with a Tabletop High Harmonic Generation Source: Generalizing Coherent Diffractive Imaging to Extended Samples in Transmission, Reflection, and Hyperspectral Modalities
written by Bosheng Zhang
has been approved for the Department of Physics

Prof. Margaret M. Murnane

Prof. Henry C. Kapteyn

Date

The final copy of this thesis has been examined by the signatories, and we find that both the content and the form meet acceptable presentation standards of scholarly work in the above mentioned discipline.

Zhang, Bosheng (Ph.D., Physics)

EUV Microscopy with a Tabletop High Harmonic Generation Source: Generalizing Coherent Diffractive Imaging to Extended Samples in Transmission, Reflection, and Hyperspectral Modalities

Thesis directed by Profs. Margaret M. Murnane and Henry C. Kapteyn

Imaging at the nanoscale is of great interest for applications in materials science, nanoscience and biology. The microscopy method developed in this thesis combines a tabletop coherent EUV/X-ray source based on high harmonic generation, and an image-forming method based on coherent diffractive imaging. This microscopy method offers truly diffraction-limited resolution; however, previous work has been limited to thin, isolated samples in transmission mode. This thesis work extends this tool for imaging non-isolated samples, and for working in reflection mode to image surface features of thick samples. The quantitative phase information of the reflection image enables surface profilometry capability with sub-nanometer precision. The microscope developed in this work is also demonstrated to have hyperspectral capability with simultaneous multi-wavelength illumination, without the need for wavelength scanning or energy-resolved detectors. In the future, by taking advantage of the short-pulse nature of the high harmonic illumination, this microscope will be able to image nanoscale ultrafast dynamics with 10 femtosecond temporal resolution, opening the door for imaging at the space-time limits.

Dedication

To my mother Guozhen Wang, my father Shihuan Zhang, and my wife Fengmei Liu.

Acknowledgements

First of all, I would like to thank my advisors, Margaret Murnane and Henry Kapteyn for their vision, advice, support, and encouragement. They have provided me access to various resources, opportunities for skill development, connections with experts in both academia and industry, and valuable experiences such as patent application.

I feel fortunate to have Dan Adams and Matt Seaberg as my colleagues throughout the majority of my PhD career. Much of the work in this thesis would not have been possible without their many ideas, suggestions, and direct contribution in experiments. I also owe them a lot for their work on the lasers. I have benefited from Dan's strong leadership, and excellence in both science and project management. I thank him for pushing and helping me to achieve and for teaching me various things including UI design. He demonstrates to me a spirit of getting the job done no matter what it takes, which is truly touching and stimulating. Matt has been a partner that is creative, forward-thinking, and knowledgable with great ability in both experiments and theories, and he is a go-to guy when I want ideas, suggestions, or a fruitful and inspiring discussion. Great challenges have been less daunting with him on the team. Dennis has made great contributions to part of this thesis work. He became an invaluable member of the team with his high work ethic, and versatile skills in both hardware and software. Although Liz joined the group not as long ago, she has already become well-known for a lot of things, especially fabrication of a sample that has brought us a series of successful results presented in this thesis work. I am hopeful that ultrafast dynamic imaging, a holy grail that has driven me and other previous members, is now possible with the project in the good hands of those two and other younger members. Days and nights with

the imaging team when we made the breakthroughs will always be a memorable experience that I am proud of.

Tenio was my mentor when I started in the KM group. I want to thank him for teaching me HHG both before and after I joined the imaging team. I also want to thank Ming-Chang, Xibin, and Isabell for teaching me various things before I started working on imaging. Thanks to all KM group members that I have worked with for help and company. Thanks to Justin, Weilun, Eric, and Farhad for collaboration. I have to thank the instrument, electronics, and computing staff who have helped and taught me, and who have made JILA a wonderful place to work at: Dave, Todd, James, Hans, Kim, Ariel, Blaine, Tracy, J.R..

Thanks to friends: Chenjie, Wei, Cong, Jing, Hongcheng, Bo, Linqiang, Xia, Yan, Hao, Qing, Long, Xiaoshi, Jianfeng, Honghua and many others that I don't have room to list, for help, company, and fun time.

Thanks to my parents and my wife for their love, encouragement and support.

Contents

Chapter

Tables

Table

Figures

Figure

Chapter 1

Introduction

In December of 1959, Richard Feynman gave a talk titled "There's Plenty of Room at the Bottom" [1] at an annual meeting of the American Physical Society at Caltech. In this famous lecture, Feynman laid the conceptual foundations for the field now called nanotechnology when he imagined a day when things could be miniaturized – when huge amount of information could be encoded onto increasingly small spaces, and when machinery could be made considerably more compact. Feynman's vision has been proven by the development of many scientific and technological fields, such as materials science, and electronics: machines and devices have been made on ever-decreasing length scales to make them faster, cheaper and more efficient or to exploit the peculiar quantum mechanical properties. For these, and many other fields such as biology, microscopy is the basic, and perhaps the most import, tool to investigate and classify small structures on the nanometer scale. It has become one of the few methodologies applied to nearly every field of science and technology in use today.

This chapter will discuss two key components of every microscopy (or more generally imaging) technique: imaging probes (or illumination sources), and image-forming methods. This discussion provides a context to introduce the unique microscopy technique developed in this thesis, one that combines coherent extreme ultraviolet (EUV) from high harmonic generation (HHG) as the imaging probe, and coherent diffractive imaging (CDI) as the image forming method. Following the discussion on microscopy, this chapter will provide an overview of this thesis.

1.1 Imaging probes and image-forming methods

The first microscope is usually credited to Zacharias Jansen in Middleburg, Holland, around the year 1595. Since then, various techniques have been developed in the field of of microscopy, or more generally imaging. Imaging techniques can be analyzed and classified based on their two key components: the type of probe used to interact with the sample to be imaged, and the method used to form an image, as shown in Fig. 1.1.

The first key component of every imaging technique is the probe it uses. Essentially, imaging is about mapping of the interaction between the selected probe and the object to be imaged, and the type of probe used directly determines its contrast mechanism. Furthermore, the probe type can put an inherent limit of the resolution by its wavelength. Far field imaging systems have a diffraction-limited resolution given by (using the Rayleigh Criterion):

$$r = \frac{0.61\lambda}{\mathrm{NA}}. \tag{1.1}$$

In addition, the choice of probe determines how thick a sample can be imaged by its penetration depth.

In principle, to image a sample, any type of wave or particles can be used as the probe. As shown in Fig. 1.1, the following probes have been used for imaging:

(1) Light or photons. This probe type has imaging contrast mainly based on elastic scattering of the photon by the sample, or some excited processes such as fluorescence. It can further classified based on the wavelength of the illuminating photons, such as visible light, EUV, X-ray, etc.

Visible light microscopy (or light microscopy, optical microscopy) is the oldest and probably the most familiar one to us – after all, human beings' eyeball imaging system relies on this probe type. It is used extensively in microelectronics, biotechnology, pharmaceutic research, mineralogy and microbiology. Its resolution is limited to $\approx$ 200 nm due to the relatively long wavelength.

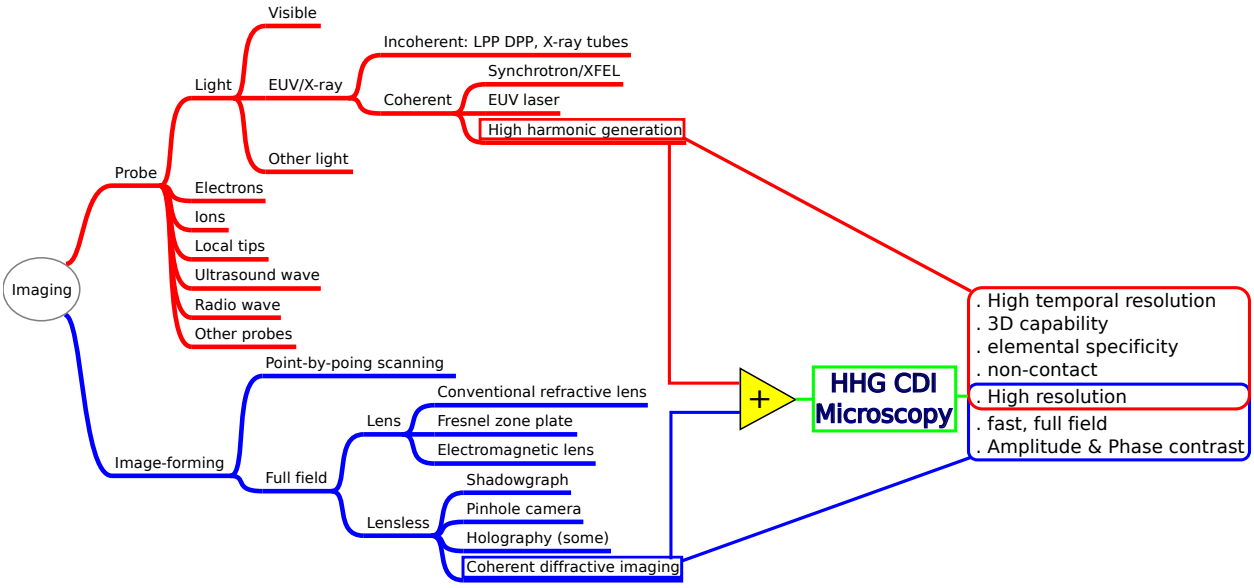

Figure 1.1: Classification of imaging techniques based on their two key components: probes (illumination sources) and image-forming methods. The microscopy in this thesis work combines high harmonic generation as the probe and coherent diffractive imaging as the image-forming method, and have combined advantages from these components.

A fluorescence microscope uses fluorescence and phosphorescence instead of the conventional transmitted or reflected light for imaging. Super-resolved fluorescence microscopy overcomes the diffraction limit in optical microscopy and brings it into the nanodimesion, opening up important applications in biology and life sciences.

Shorter wavelength probes, such as EUV or X-ray, can yield higher resolution. Several image forming methods can be applied to this probe type, including scanning transmission X-ray microscopy (STXM), transmission X-ray microscopy(TXM) [2] and CDI [3]. X-ray microscopy can image with elemental and chemical contrast. It also has three-dimensional imaging capability due to the long penetration depth of X-rays.

(2) Electrons. Due to the electron's short wavelength, electron microscopes have a much higher resolution than optical microscopes. There are several types of electron microscopes: scanning electron microscope (SEM), transmission electron microscope (TEM), scanning transmission electron microscope (STEM), etc. In SEM, interaction of the electrons with the specimen result in several possible products, including low-energy secondary electrons and high-energy backscattered electrons, light emission (cathodoluminescence) or X-ray emission, all of which provide signals carrying information about the properties of the specimen surface, such as its topography and composition. TEM can image with a really high resolution of below 0.5 Å [4] but is limited to thin samples ($\approx$ 100 nm or less).

(3) Ions. A representative example is scanning helium ion microscope. Ions have even shorter wavelengths, and do not suffer from a large excitation volume, so an ion microscope can have even higher resolution than SEM. It usually has a better material contrast too.

(4) Local tips such as a mechanical tip used in atomic force microscopy (AFM), a well-established technique for surface profilometry. Here "local tips" refer to the probes used in scanning probe microscopy (SPM). They represent a special category of imaging probes, including a large variety of probes that that interact with the object locally through different types of interaction, such as atomic force, magnetic force, etc.

(5) Other probes include ultrasound wave used in sonography for imaging body structures, radio waves together with magnetic fields used in magnetic resonance imaging (MRI), etc.

The second key component of every imaging technique is the image-forming method it uses. As shown in Fig. 1.1, both point-by-point scanning and full field imaging techniques exist. In point-by-point scanning techniques, either the beam, such as in SEM, or the sample, such as in STXM, AFM or other SPM, can be raster scanned to form a two-dimensional image. Full field imaging techniques include those with an image forming optics, such as a lens, and those without (termed "lensless" here). The type of lens includes conventional refractive lenses used in optical microscopy, Fresnel zone plates used in TXM, electromagnetic lenses used in electron or ion microscopy; In these imaging techniques, the lens design is the core issue for improving resolution and decreasing aberration.

A simple example of lensless, full field imaging techniques is the shadowgraph imaging used in X-ray radiography. A pinhole camera is also a lensless imaging technique. Two import techniques in this category include some types of holographic imaging (such as in-line holography invented by Gabor [5]) and CDI [6]. While it is possible for these two techniques to employ certain optics or lenses to condense the illumination onto the sample, the image-forming process itself does not rely on the lenses. CDI uses computer algorithms to replace lenses to form an image, as will be seen in Chapter 3.

The microscopy developed in this thesis combines coherent EUV/X-ray generated from HHG as the imaging probe and CDI as the image forming method. As shown in Fig. 1.1, advantages of EUV/X-ray from HHG as a probe include high temporal resolution of 10 fs due to its short pulse duration, 3D capability, elemental specificity because many elements have their resonance frequencies in this wavelength range, non-contact working mode, and higher resolution offered by shorter wavelengths compared to conventional optical microscopy. CDI as an image-forming method have advantages, such as truly diffraction limited resolution without aberration from image-forming optics or limitation from the NA of the optics, inherently much faster than point-by-point

scanning methods because it is a full field technique, and it provides quantitative amplitude and phase information at the same time, enabling comprehensive and definitive characterization of the sample. Combining HHG and CDI would lead to a microscope that combines the advantages from both sides.

1.2 Overview of this thesis

HHG CDI microscopy was first demonstrated in 2007, by Richard Sandberg, Ariel Paul *et al.* from our group [7]. In 2011, my colleagues Matt Seaberg, Dan Adams *et al.* demonstrated a record, 22 nm resolution imaging with a 13 nm HHG source [8]. Both of these results are for isolated samples in transmission mode with monochromatic light. This thesis will focus on further developments of this microscopy method, including generalizing it to extended samples in transmission, reflection, and hyperspectral modalities.

The two key components of this microscopy, coherent EUV/X-ray from HHG as the probe, and coherent diffractive imaging as the image-forming methods, are described in Chapter 2 and Chapter 3. The following chapters will discuss the results with this microscopy method. CDI was conventionally limited to small, isolated samples, and has very limited success in reflection geometry which is important for imaging surfaces, and structures on thick substrates. Chapter 4 will discuss the first demonstration of generalizing it to non-isolated samples with a HHG source. Chapter 5 will discuss the first demonstration of a general-purpose reflection CDI microscope based on ptychography. Chapter 6 will discuss results on further improvement of reflection ptychography CDI. They enable high lateral and axial resolution surface imaging, with excellent imaging fidelity compared with well-established methods such as SEM and AFM. Chapter 7 will discuss results on hyperspectral imaging with multi-colored HHG combs. Instead of monochromatic illumination, hyperspectral ptychography imaging uses multiple colors to illuminate the sample. The incoherent sum of intensities from different colors are decomposed by the ptychography algorithm, enabling spectromicroscopy with separate responses of the sample at each illuminating color. Finally, in Chapter 8, ideas for future work with this microscope are discussed.

Chapter 2

Imaging Probe: High Harmonic Generation Producing Coherent EUV/X-ray

This chapter describes the first of the two key components for our unique microscopy: coherent EUV/X-ray from high harmonic generation used as the imaging probe. First, the constrast mechanism is discussed for this probe. Then the theory of the high harmonic generation is described. Finally, relevant properties of this imaging probe are discussed.

2.1 Coherent EUV/X-ray imaging contrast mechanism

The response of materials to electromagnetic radiation can be characterized by their index of refraction $n(\omega)$, where ω is the frequency of the radiation. For the spectral range of EUV or X-ray, $n(\omega)$ is typically written as [9]:

$$n(\omega) = 1 - \delta + i\beta \tag{2.1}$$

where

$$\begin{aligned} \delta &= \frac{n_a r_e \lambda^2}{2\pi} f_1^0(\omega) \\ \beta &= \frac{n_a r_e \lambda^2}{2\pi} f_2^0(\omega) \end{aligned} \tag{2.2}$$

where n_a is the average density of atoms, r_e is the classical electron radius which is about 2.8×10^{-15}m, λ is the wavelength of the radiation. Here $f_1^0(\omega)$ and $f_2^0(\omega)$ refer to the real and the imaginary parts of the complex atomic scattering factor:

$$f^0(\omega) = \sum_s \frac{g_s \omega^2}{\omega^2 - \omega_s^2 + i\gamma\omega}. \tag{2.3}$$

where γ measures the phenomenological damping force, ω_s is the resonance frequency associated with electron energy level s, g_s is the so-called "oscillator strength", which in the simple semi-

classical model is the number of electrons. We see that $n(\omega)$ depends on the material's composition and the density in the sample.

For a transmission geometry, if the sample is thin enough to satisfy the projection approximation [10], the exit surface wave E_{out} for a coherent incident wave E_{in} can be computed by a multiplication:

$$E_{\text{out}}(x', y') = E_{\text{in}}(x', y') \cdot t(x', y') \tag{2.4}$$

where

$$t(x', y') = e^{-k_0 \int \beta(x', y', z')\, \mathrm{d}z'} e^{-ik_0 \int \delta(x', y', z')\, \mathrm{d}z'} \tag{2.5}$$

Here the phase of $E_{\text{out}}(x', y')$ is relative to the phase corresponding to vacuum of the same thickness. The sample would show an amplitude contrast of $e^{-k_0 \int \beta(x', y', z')\, \mathrm{d}z'}]$, and a phase contrast of $-k_0 \int \delta(x', y', z')\, \mathrm{d}z'$ in its two-dimensional exit wave. Spatial variation of the sample's composition, density, or thickness if the complex wave E_{out}, or the complex transmission function $t(x', y')$ is to be imaged, which is true in coherent diffractive imaging.

For a reflection geometry, E_{out} can be written as:

$$E_{\text{out}}(x', y') = E_{\text{in}}(x', y') \cdot r(x', y') \tag{2.6}$$

where

$$r(x', y') = r_m(x', y') \cdot \exp(i \frac{-4\pi h(x', y') \cos\theta_i}{\lambda}) \tag{2.7}$$

or

$$r(x', y') = |r_m(x', y')| \cdot \exp\left[i(\phi \left(r_m(x', y') + \frac{-4\pi h(x', y') \cos\theta_i}{\lambda} \right) \right]. \tag{2.8}$$

Here $r_m(x', y')$ is the complex reflection efficient form the material of the reflecting surface itself, $h(x', y')$ is the surface height distribution, and θ_i is the angle of incidence. r_m is determined by $n(\omega)$ through Fresnel equations. So coherent imaging of $E_{\text{out}}(x', y')$ or $r(x', y')$ will show contrast from both the composition and the height profile.

2.2 Theory of high harmonic generation

After seeing the contrast mechanism of imaging with coherent EUV/X-ray light, let us see how to generate them. Four approaches exist for generating coherent radiation at these short wavelengths: synchrotrons, free electron lasers, EUV/soft X-ray lasers and high harmonic generation (HHG). Compared with synchrotrons and free electron lasers, HHG is a very compact source that can be put on a tabletop. EUV/Soft X-ray lasers have pulse durations of $\approx$ picosecond, while HHG has a much shorter pulse duration, on the order of 10 fs or less, allowing for much higher temporal resolution.

HHG, as an extreme nonlinear process that upconverts the driving laser frequency to its high orders, was first observed in late 1980's [11, 12]. Typically it is driven by ultrafast lasers composed of an oscillator that generates femtosecond pulses with low pulse energy, and an amplifier that increases the pulse energy to the mJ level. HHG can be understood on two levels: the microscopic, single atom level, which explains the emission of high energy photons, and the macroscopic level where phase-matching is considered.

2.2.1 Microscopic three-step model

On a microscopic, single atom level, the emission of high-energy photons in HHG can be explained with a semi-classical, three-step model [13] that is quite analogous to what happens in X-ray tubes. The photos and schematics of these two sources are compared in Fig. 2.1. In an X-ray tube, as illustrated by Fig. 2.1(b), electrons in the cathode are first ionized, then accelerated in the strong electric filed provided by the high voltage between the cathode and the anode, and finally collide with the anode and emitting the high kinetic energy they have gained from the external electric field. The three steps (ionization, acceleration, and collision) are roughly what happen in HHG on a single atom level. A HHG source in a waveguide geometry is illustrated in Fig. 2.1(d). Intense femtosecond laser pulses with a linear polarization (recent work shows circular polarization can also work [14]) are focused into a waveguide that is filled with a certain type of noble gases,

such as argon or helium. The electrons of the noble gas atoms are first ionized by the strong field of the laser. The the free electrons are accelerated by the electric field of the laser pulse, and as the electric field oscillates and changes direction, the electrons will deaccellerate, turn back to the parent ions, and finally collide and recombine with the ions. At recombination, the energy is released in the form of high-energy photons, typically in the EUV or X-ray range. Depending on at the phase of the electric field at the moment of ionization, the calculated energy released can be as high as:

$$h\nu_{\max} \approx I_p + 3.17U_p \tag{2.9}$$

where I_p is the ionization potential of the atoms, and U_p is the so-called ponderomotive potential of the laser field, defined as

$$U_p = \frac{e^2E^2}{4m_e\omega_0^2} \tag{2.10}$$

where e is the electron charge, E is the linearly polarized electric field amplitude, ω_0 is the laser carrier frequency and m_e is the electron mass.

2.2.2 Macroscopic phase matching

Macroscopically, HHG requires phase matching to be efficient, similar to other nonlinear optics processes, such as second harmonic generation, sum and difference frequency generation, parametric amplification and oscillation. Phase matching for HHG means emissions from atoms at different positions along the propagation axis are in phase, so the beam adds up coherently. The phase mismatch Δk is defined as:

$$\Delta k = qk_1 - k_q \tag{2.11}$$

where q is the harmonic order, k_1 is the wave number for the driving fundamental frequency, and k_q is the wave number for qth harmonic. Δk has contributions from three parts: the neutral atoms, the plasma due to ionization, and the waveguide geometry(in contrast to free space that is phase mismatch free). It can be written as [15, 16]:

$$\Delta k \approx q\frac{u_{11}^2\lambda_1}{4\pi a^2} - qP(1-\eta)\frac{2\pi}{\lambda_1}(\Delta\delta + n_2) + qP\eta N_a r_e \lambda_0 \tag{2.12}$$

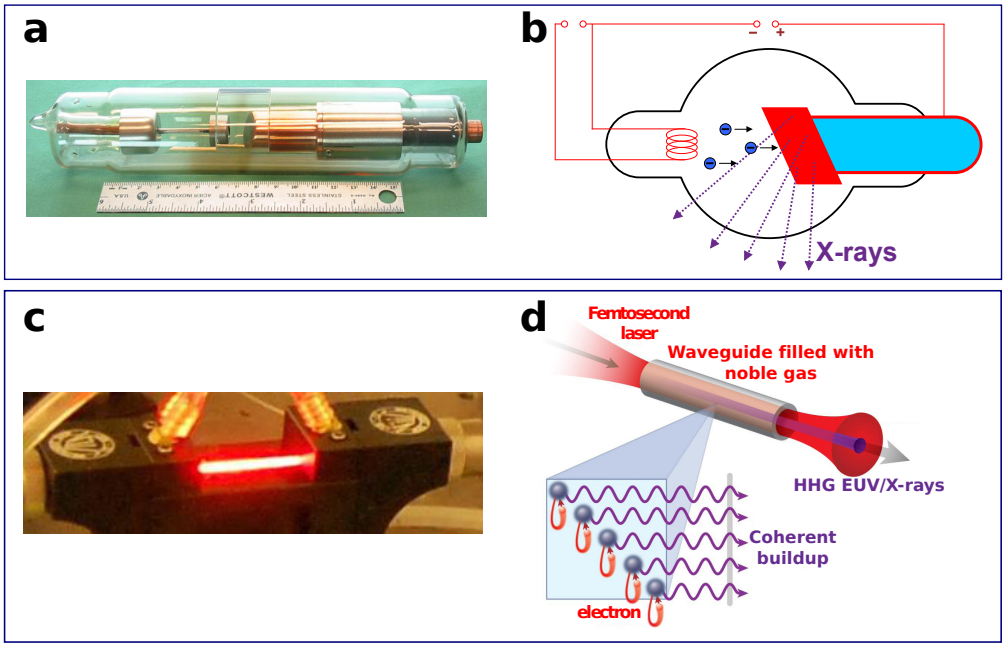

Figure 2.1: A comparison between an X-ray tube and a HHG source that has a waveguide geometry. A photo and a schematic are shown in (a) and (b) for an X-ray tube, and in (c) and (d) for a HHG source.

where we assumed the light is coupled into EH_{11} mode described by the Bessel J_0 function, and u_{11} is the root for the first zero, λ_1 is the fundamental (first order) wavelength, a is the waveguide radius, P is the pressure in atmospheres, $\Delta\delta$ is the difference in index of refraction of the neutral gas at the fundamental and the qth order harmonic wavelengths, η is the ionization percentage, N_a is the number density of the gas at one atmosphere, and r_e is the classical electron radius. We have used the approximation the harmonic order $q \gg 1$, and at EUV/X-ray wavelengths, the index of refraction is close to 1. The two main parameters used in experiments to achieve phase matching are the pressure of the noble gas, and the pulse energy which affects the ionization percentage η. The specific parameters can be found in later chapters on experimental results.

2.3 Properties of HHG

EUV or X-rays produced by HHG are spatially coherent, in contrast to incoherent X-ray radiation from X-ray tubes. It is driven by a laser which is spatial coherent, and the propagation in the waveguide can purify the spatial modes of the coupled laser light. With Young's double slit measurement, this source exhibits spatial coherence across nearly the whole beam extent in the EUV [17] and X-ray [18] wavelengths.

A typical HHG spectrum is shown in Fig. 2.2 [19]. Usually, several harmonics with odd orders are phase matched simultaneously. As estimated from the spectrometer measurement represented by the dashed line in Fig. 2.2, for each harmonic, $\lambda/\Delta\lambda \approx 100$. Usually only one harmonic is selected through multilayer mirrors. Imperfect monochromaticity causes blurring of diffraction fringes at high diffraction angles, thus a decrease of spatial resolution in diffractive imaging. A discussion with a specific experimental situation will be presented in Chapter 4.

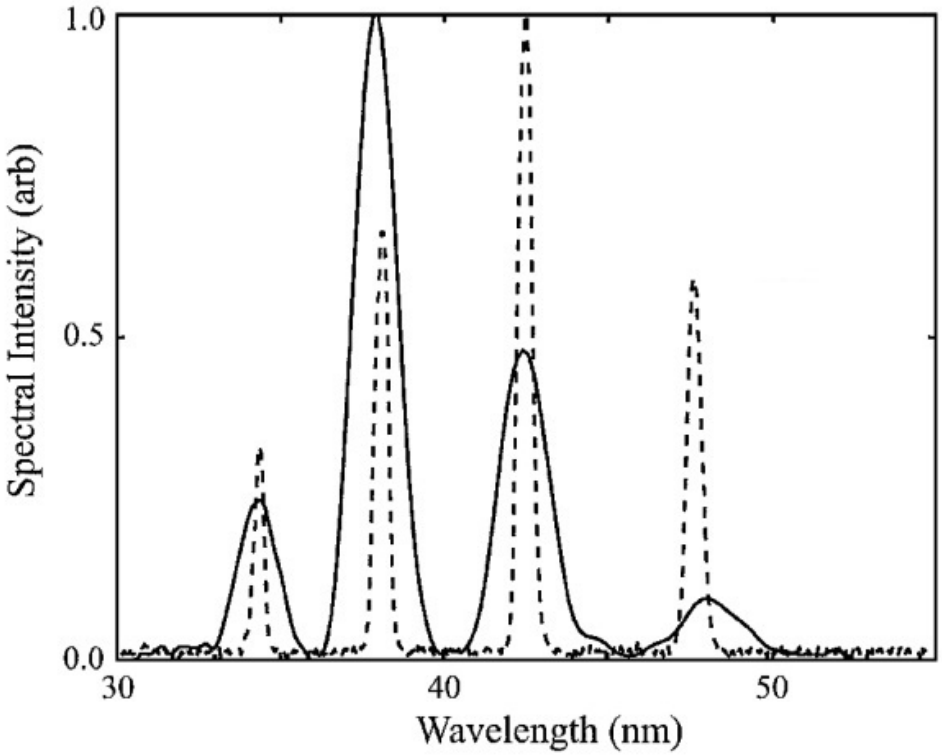

Figure 2.2: A representative HHG spectrum in the EUV range obtained from a spectrometer (dashed curve) and from a double-pinhole measurement. Figure adapted from [19].

Chapter 3

Image-forming Method: Coherent Diffractive Imaging

Coherent diffractive imaging (CDI) [3, 6] is the image forming method of the microscopy developed in this thesis work. Also called "lensless imaging", CDI is a computational imaging technique that replaces image forming optic(s) with a computational algorithm. As illustrated in Fig. 3.1, in CDI, a coherent beam of wavelike particles, such as photons or electrons, is incident on the object to be imaged, and the diffraction magnitude is measured on a pixel-array detector. With the measured diffraction magnitude, and additional known constraints about the sample, iterative algorithms are applied to retrieve the phase of the diffraction that is missing during the measurement of the magnitude. With both the magnitude and the phase of the diffraction, and the mathematical relationship of the complex diffraction field from the object, the image is calculated, with both amplitude and phase contrast.

This chapter will first provide a historical review of the CDI techniques including both single-diffraction CDI and ptychography CDI [20]. The next two sections will discuss two theoretical aspects of CDI: the diffraction theory, and iterative algorithms for diffraction phase retrieval. The section on the diffraction theory aims to establish a systematic framework, which covers different diffraction formulas, the approximations they use, and their ranges of applicability. This section aims to make it clear which diffraction formula to use with given experimental conditions. The section on iterative algorithms will explain how to retrieve phase for the measured diffraction modulus using iterative algorithms.

After the theories behind CDI, this chapter will discuss the numerical implementation of

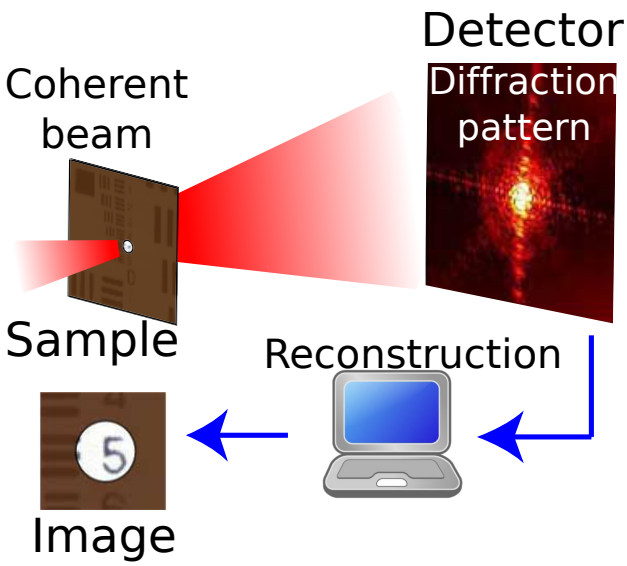

Figure 3.1: Illustration of the coherent diffractive imaging technique. A spatially-coherent beam illuminates the sample, and the diffracted intensity is measured on a pixel-array detector. Then iterative algorithms are applied to retrieve the phase that cannot be physically measured for the diffracted wave, and reconstruct an image of the sample.

these theories in CDI.

3.1 Review of CDI developments

Here the CDI techniques divided into two categories: single-diffraction CDI and ptychography CDI. To reconstruct a 2D image of the sample, only one diffraction pattern is needed in single-diffraction CDI, while multiple diffractions measured at different scanning positions are needed in ptychography CDI.

3.1.1 Single-diffraction CDI

In 1895, Röntgen discovered X-ray and in 1912 Laue discovered X-ray diffraction from crystals. Afterwards, the field of X-ray crystallography developed rapidly, and became an important tool for identifying the atomic and molecular structures of a crystal. Since many materials can form crystals — such as salts, metals, minerals, semiconductors, as well as various inorganic, organic and biological molecules — X-ray crystallography has been fundamental in many scientific fields. It is used to reveal the structure and function of biological molecules, including vitamins, drugs, proteins, and nucleic acids. For example, in 1953, Watson and Crick suggested the double-helix model of DNA structure using this tool.

X-ray crystallography was the first experimental discipline to face up to the consequences of lost phase: when the diffraction was measured, only the amplitude (intensity, or flux) can be physically measured but not the phase. Had both the amplitude and the phase of the complex wave been known, the wave can then be directly propagated back from the detector plane to the sample position to get an image. Indeed, this type of inverse problem — the reconstruction of an object from measurements of its scattered intensity — has occupied physicists for over a century, and arises in fields as varied as optics, astronomy, medical tomographic imaging, holography, electron microscopy, and particle scattering, besides X-ray crystallography. Fortunately for crystalline structures, there is usually large quantities of stereochemical *a priori* information making phase retrieval much more tractable than for generalized, non-crystalline structures.

Extending X-ray crystallography to a general diffraction imaging technique started in 1952, when Sayre [21] observed that Bragg diffraction undersamples the diffraction intensity pattern relative to Shannon's theorem, and noted out that there may be enough information in the diffraction itself to uniquely solve the diffracting object, if only one could measure midway between Bragg peaks. In 1980, he pointed out [22] that a single isolated non-peoriodic object permits such a higher density sampling scheme. He envisaged extending X-ray crystallography to general imaging of non-periodic samples using diffraction — the method known as coherent diffractive imaging (CDI) now. However, Sayre's early work does not prove that a properly sampled far-field diffraction pattern would necessarily yield sufficient information to determine an image of the object, primarily because it does not deal with issues of the independence of the additional measurements. In 1978, Fienup, working independently of Sayre, argued that [23] it should be possible to reconstruct an object form its Fourier modulus, and proposed some iterative algorithms (input-output approach) that built on the Gerchberg-Saxton algorithm developed in 1972. In 1982, Bates published a paper on the existence of a unique solution for the phase recovery problem [24]. He argued that the diffraction from an isolated object would certainly lead to a unique solution apart from some trivial ambiguities (lateral translation, complex conjugate, spatial inversion, and absolute phase). In early 1980's, Fienup's further development of iterative algorithms with feedback [25] produces a remarably sucessful optimization method for phase retrieval. The iterations can be viewed as Bregman projections in Hilbert space, and this insight has allowed theoreticians to analyze and improve on the baisc Fienup algorithm [26].

On the experimental side, the successful demonstration of X-ray CDI did not happen until 1999, by Miao *et al.* on a synchrotron source [6]. There was great effort from my group to move CDI from the huge light sources to our unique, tabletop HHG source. In 2007, Richard Sandberg, Ariel Paul *et al.* from our group first demonstrated it with a tabletop, high harmonic EUV source [7]. In 2011, my colleagues Matt Seaberg, Dan Adams *et al.* demonstrated a record, 22 nm resolution imag with a 13 nm HHG source [8].

Conventional CDI does have a serious limitation: it is applicable to samples that are small

and isolated. In 2008, Abbey *et al.* demonstrated the keyhole CDI method, which successfully removed the isolation limitation. Two factors contribute to its success: first, instead of requiring the sample to be isolated, it uses isolated illumination by putting an aperture in the beam. The beam maintained a sharp edge and a finite support when it propagated to the sample plane. So although the sample is not isolated, the exit surface wave is, making the isolation constraint in the sample plane still valid. Second, instead of illuminating the sample with plane wave, they used a beam with a phase curvature. This phase curvature provides a low-resolution in-line hologram image of the sample, and also contributes to eliminate ambiguities and facilitates convergence of the iterative algorithm. I, together with Matt, Dan *et al.*, demonstrated keyhole CDI with HHG [27], with results shown in Chapter 4. Dennis Gardner, I and other members of the group also demonstrated apertured illumination CDI, which is a more demanding yet more straightforward approach, is based on the same idea of isolating the illumination instead of isolating the sample.

To date, single-diffractin (non-ptychographical) CDI has been used to extract the structure and dynamics of a variety of objects, including biological samples [28, 29], nanocyrstals [30, 31], strain fields inside a nanocrystal [32] and integrated circuits [33].

3.1.2 Ptychography CDI

Instead of retrieving phase from a single-diffraction pattern, ptychography CDI (or just ptychography) [20] scans the sample relative to the beam, with overlap in between adjacent scans. The overlap , instead of the isolation constraint in single-diffraction CDI, provides redundant information that allows the phase problem to be solved.

Ptychography CDI has gone through a quite different history than conventional CDI. Between about 1968 and 1973, Hoppe [34–38] conceived the concept of ptychography to solve the phase recovery problem in crystallography. The concept uses convolution theorem, and in German, "convolution" shares the same meaning with "folding", for which the Greek word is "ptycho"; hence the name "ptychography". In 1989 and 1992, Bates and Rodenburg published two papers on the Wigner distribution deconvolution method used to recover the phase for general, non-crystalline

structures, and in 1996, Chapman demonstrated this method using an X-ray source [39]. In 2004, Rodenburg and Faulkner introduced and demonstrated a faster and more efficient iterative method for ptychographic phase retrieval [40, 41], later known as ptychographical iterative engine (PIE). This method was demonstrated with X-ray in 2007 by Rodenburg *et al.* In 2008, Thibault *et al.* discovered that not only the object, but also the illumination beam can be solved with ptychography [42]. This has pushed the capability of the ptychography CDI to a new level. A detailed account of the history of ptychography can be found in Ref. [43].

In 2014, we demonstrated for the first time generalized CDI in a reflection geometry with HHG [44], as shown in Chapter 5. Afterwards, together with Dennis Gardner and Dan, I demonstrated reflection CDI with high lateral and axial resolution, and unprecedented quality. The images from our microscope compare favorably with those from well-established microscopy methods, such as SEM and AFM. It has a unique, powerful contrast mechanism, making it a promising tool for surface metrology. This work is covered in Chapter 6. Another exciting result involves hyperspectral imaging: the sample is illuminated with multiple colors at the same time and the incoherent sum is detected; then a computational method is used to decouple the incoherent sum, and separate the reponse of the sample at different wavelengths. This spectromicroscopy method exploits the power of computational imaging, and has no need for an energy-resolved detector, and serial scanning of wavelengths. This work is covered in Chapter 7.

3.2 Diffraction theory

After the review of historical developments in the previous section, this section focuses on the first theoretical aspect of CDI – diffraction theory. I will first review the history of diffraction theory. Then I will provide a short derivation of the key diffraction formulas for different experimental conditions. Most of these formulas can be found in textbooks covering the topic of diffraction [45,46], while some are new results; all of them are put in a coherent, systematic framework. After this section, it should be clear to the readers which diffraction formula to use for the specific CDI experimental condition they are faced with.

3.2.1 History of diffraction theory

The origin of diffraction theory can be dated back to 1660, when Italian scientist Francesco Maria Grimaldi coined the word "diffraction" and was the first to record accurate observations of the phenomenon. Since then, the understanding of diffraction has deepened along with the development of theories on the nature of the light. Table 3.1 showcases a short summary of key milestones, extracted from Refs. [45, 47].

3.2.2 Wave equations from Maxwell's equations

We start from Maxwell's equations (Eq. 6.6 in Ref. [46], with the same notations) which govern electromagnetic phenomena in the classical (non-quantum) regime:

$$\begin{aligned} \vec{\nabla} \cdot \vec{D} &= \rho \\ \vec{\nabla} \cdot \vec{B} &= 0 \\ \vec{\nabla} \times \vec{E} &= -\partial_t \vec{B} \\ \vec{\nabla} \times \vec{H} &= \vec{J} + \partial_t \vec{D} \end{aligned} \tag{3.1}$$

, where

$$\begin{aligned} \vec{B} &= \mu_0 \vec{H} + \vec{M}, \\ \vec{D} &= \epsilon_0 \vec{E} + \vec{P} \end{aligned} \tag{3.2}$$

In terms of vector potential $\vec{A}$ and scalar potential Φ which relate to the fields $\vec{E}$ and $\vec{B}$ in the following way:

$$\begin{aligned} \vec{B} &= \vec{\nabla} \times \vec{A} \\ \vec{E} &= -\nabla \Phi - \partial_t \vec{A} \end{aligned} \tag{3.3}$$

and which we choose to satisfy the Lorenz condition:

$$\vec{\nabla} \cdot \vec{A} + \frac{1}{c^2} \partial_t \Phi = 0 \tag{3.4}$$

, then the wave equations are:

$$\begin{aligned} (\nabla^2 - \tfrac{1}{c^2} \partial_{tt}) \Phi &= -\tfrac{\rho}{\epsilon_0} \\ (\nabla^2 - \tfrac{1}{c^2} \partial_{tt}) \vec{A} &= -\mu_0 \vec{J} \end{aligned} \tag{3.5}$$

Table 3.1: Key milestones in the history of diffraction theory.

Year	Event
1660	Grimaldi coined the word "diffraction" and recorded accurate observation of the diffraction phenomenon for the first time.
1678	Huygens proposed the principle named after him: "Every point on a wave-front may be considered a source of secondary spherical wavelets which spread out in the forward direction at the speed of light. The new wave-front is the tangential surface to all of these secondary wavelets."
1704	Newton published *Opticks*, in which he proposed the particle theory of light.
1801	Young performed the double slit experiment, strengthened the wave theory of light.
1818	Fresnel published his famous memoir on the Diffraction of Light, calculated the distribution of light in diffraction patterns with excellent accuracy based on work by Hyugens and Young.
1860	Maxwell identified light as electromagnetic wave, and in the following two years published an early form of equations named after him.
1882	Kirchhoff formulated the so-called Huygens-Fresnel principle.
1896	Sommerfeld modified Kirchhoff's formula using Green's function, resulting in Rayleigh-Sommerfeld diffraction theory, a rigorous solution for two-dimensional scalar diffraction problem.
1939-1947	Stratton, Chu, Schelkunoff and Smythe [48–50] formulated vectorial diffraction theory.

For radiation generation problems, we consider situations where there are free sources of charge and current; while for radiation diffraction or propagation problems, we consider a volume inside which there are no free sources of charge and current: $\rho = 0$, $\vec{J} = 0$. Then in terms of potentials, the wave equations become:

$$\begin{aligned}(\nabla^2 - \tfrac{1}{c^2}\partial_{tt})\Phi = 0 \\ (\nabla^2 - \tfrac{1}{c^2}\partial_{tt})\vec{A} = 0\end{aligned} \tag{3.6}$$

In terms of elctric field $\vec{E}$, the wave equation is:

$$[\nabla^2 - \epsilon_0\mu_0\partial_{tt}]\vec{E} = \nabla(\vec{\nabla}\cdot\vec{E}) + \mu_0\partial_{tt}\vec{P} + \partial_t\vec{\nabla}\times\mu_0\vec{M} \tag{3.7}$$

In terms of electric displacement field $\vec{D}$, the wave equation is:

$$\nabla^2\vec{D} - \epsilon_0\mu_0\partial_{tt}\vec{D} = -\vec{\nabla}\times(\vec{\nabla}\times\vec{P}) + \epsilon_0\partial_t\vec{\nabla}\times\mu_0\vec{M} \tag{3.8}$$

The above three wave equations form the bases for all the further treatment of the diffraction regime in this section. We will use Eq. 3.6 for two-dimensional (2D) vectorial diffraction theory, and Eq. 3.7 for 2D scalar diffraction theory. Here "two-dimensional" means diffraction is calculated against a two-dimensional distribution of fields, usually on the "exit surface". We will use Eq. 3.8 for three-dimensional (3D) diffraction theory; here "three-dimensional" means the diffraction is calculated against the three-dimensional distribution of certain properties of the scatterers.

3.2.3 2D Scalar Diffraction Theory with Green's function approach: Rayleigh-Sommerfeld diffraction integral

Scalar diffraction theory ignores the vector nature of the electromagnetic fields. To be specific, boundary conditions lead to coupling between $\vec{E}$ and $\vec{H}$ and between different components of $\vec{E}$ [48, 51]. This treatment simplifies the problem, and turns out to provide accurate enough result when the feature dimension of the scattering object is much larger than the wavelength. Mathematically, we set the magnetic response $\vec{M} = 0$ in Eq. 3.7. We also consider the situation where the

medium is isotropic and linear dielectric with $\chi(\vec{r})$ being the electric susceptibility, then we can write $\vec{P} = \epsilon_0\chi(\vec{r})\vec{E}$. Eq. 3.7 thus becomes

$$[\nabla^2 - \epsilon_0\mu_0\partial_{tt}]\vec{E} = -2\nabla(\vec{E}\cdot\nabla\ln n) + \chi(\vec{r})\epsilon_0\mu_0\partial_{tt}\vec{E} \tag{3.9}$$

We write $\vec{E} = \vec{E}(\vec{r},t)$ as the combination of its monochromatic components:

$$\vec{E} \equiv \vec{E}(\vec{r},t) = \int \mathrm{d}\omega\vec{E}(\vec{r},\omega)e^{-i\omega t} \tag{3.10}$$

and plug it in the wave equation above, then we have:

$$[\nabla^2 + k_0^2]\vec{E}_\omega = \vec{f_s} \tag{3.11}$$

where $\vec{E}_\omega(\vec{r}) \equiv \vec{E}(\vec{r},\omega)$ and f_s denotes the source term:

$$\vec{f_s}(\vec{r}) = -\chi(\vec{r})k_0^2\vec{E}_\omega - \nabla(\vec{E}_\omega\cdot\nabla\ln(1+\chi(\vec{r}))). \tag{3.12}$$

We are going to use Green's function approach to solve the wave equation Eq. 3.11, but before doing that, we should keep in mind that Green's theorem is applicable for functions that are continuous over a complete bounding surface. Again, the boundary conditions at the sharp edges on the scattering object, which necessitate the consideration of the vectorial nature of the electromagnetic field, can also make the field discontinuous at these places.

Consider a Green's function, which satisfies $[\nabla^2 + k^2]G(\vec{r},\vec{r}') = \delta(\vec{r}-\vec{r}')$, with V denoting a volume containing the position $\vec{r}$ in consideration, we can write:

$$\begin{aligned}
\vec{E}_\omega(\vec{r}) &= \textstyle\int_V \mathrm{d}\vec{r}'\vec{E}_\omega(\vec{r}')\delta(\vec{r},\vec{r}') = \int_V \mathrm{d}\vec{r}'\vec{E}_\omega(\vec{r}')(\nabla^2+k^2)G(\vec{r},\vec{r}') \\
&= \textstyle\int_V \mathrm{d}\vec{r}'\vec{E}_\omega(\vec{r}')(\nabla^2+k^2)G(\vec{r},\vec{r}') - G(\vec{r},\vec{r}')\big\{(\nabla^2+k^2)\vec{E}_\omega(\vec{r}') - \vec{f_s}(\vec{r}')\big\} \\
&= \textstyle\int_V \mathrm{d}\vec{r}'[\vec{E}_\omega(\vec{r}')\nabla'^2G(\vec{r},\vec{r}') - G(\vec{r},\vec{r}')\nabla'^2\vec{E}_\omega(\vec{r}')] + \int_V \mathrm{d}\vec{r}G\vec{f_s}
\end{aligned} \tag{3.13}$$

Applying Green's theorem to the above euqation leads to

$$\vec{E}_\omega(\vec{r}) = \oint_S \mathrm{d}\vec{r}'(G(\vec{r},\vec{r}')\partial_n'\vec{E}_\omega(\vec{r}') - \vec{E}_\omega(\vec{r}')\partial_n'G(\vec{r},\vec{r}')) + \int_V \mathrm{d}\vec{r}'G\vec{f_s} \tag{3.14}$$

where S is the surface enclosing the chosen volume V, ∂_n' is the directional derivative along $\vec{n}$, the normal vector of surface S pointing to inside V.

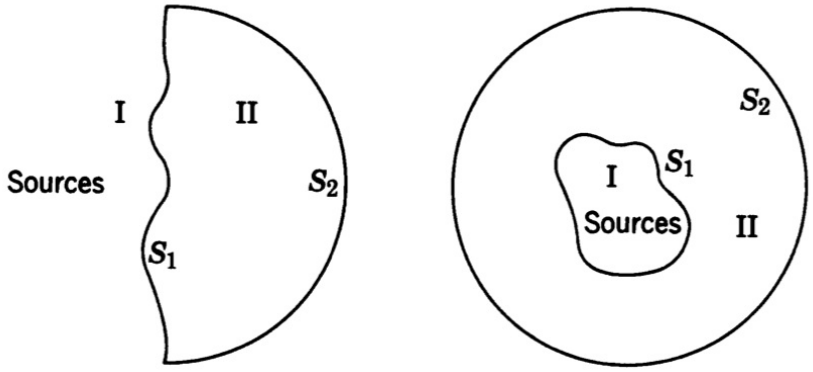

Figure 3.2: Diffraction geometries for homogenous volume and inhomogeneous volume. Region I contains the scattering sources. Region II is the diffraction region. Figure adapted from [46].

There are two possible diffraction geometries as shown in Fig. 3.2: homogeneous and inhomogeneous geometries. First we consider the homogeneous case where the volume under consideration contains no scattering sources ($\vec{f_s} = 0$), then Eq. 3.11 becomes the homogeneous Helmholtz equation:

$$[\nabla^2 + k^2]\psi = 0 \tag{3.15}$$

where we use ψ to denote a scalar component of $\vec{E}$, and the solution Eq. 3.14 becomes:

$$\psi(r) = \int_S \mathrm{d}\vec{r}'(G(\vec{r},\vec{r}')\partial'_n\psi(\vec{r}') - \psi(\vec{r}')\partial'_n G(\vec{r},\vec{r}')) \tag{3.16}$$

We choose the Green's function to be Dirichlet Green's function:

$$G = G_D \equiv G_{\mathrm{RS}-} = -\frac{1}{4\pi}(\frac{e^{ikR}}{R} - \frac{e^{ik\tilde{R}}}{\tilde{R}}) \tag{3.17}$$

where $R = |\vec{r} - \vec{r}'|$, $\tilde{R} = |\vec{r} - \tilde{\vec{r}}'|$, $\tilde{\vec{r}}'$ is the image of the $\vec{r}'$ relative to S_1 surface. It satisfies:

$$\begin{cases} G_{\mathrm{RS}-}\big|_{\vec{r}'\in S_1} = 0 \\ \partial_n G_{\mathrm{RS}-}\big|_{\vec{r}'\in S_1} = 2\partial_n G_K\big|_{S_1} \end{cases} \tag{3.18}$$

where

$$G_K(\vec{r},\vec{r}') = -\frac{1}{4\pi}\frac{e^{ikR}}{R} \tag{3.19}$$

is the Green's function used in Kirchhoff diffraction integral.

If we choose S_2 to be part of an infinitely large sphere, then with Sommerfeld radiation condition $\lim_{r'\to+\infty} r'(\partial_{n'} + ik)\psi(\vec{r}') = 0$, the surface integral has contribution only from S_1, but not from S_2. We then get *the first Rayleigh-Sommerfeld solution*, also called *Rayleigh-Sommerfeld diffraction integral*:

$$\psi_{\mathrm{RS}-}(\vec{r}) = \int_{S_1} \mathrm{d}\vec{r}'\psi(\vec{r}')\frac{1}{i\lambda}\frac{e^{ikR}}{R}\frac{z}{R}(1 - \frac{1}{ikR}) \tag{3.20}$$

where λ is the wavelength; $\vec{r}'$ is a source position; $\vec{r}$ is the position where we calculate the diffraction. For practical use, we usually choose S_1 to be a flat surface immediately after an object that is basically a two-dimensional object, the so-called exit surface. The geometry is illustrated in Fig. 3.3.

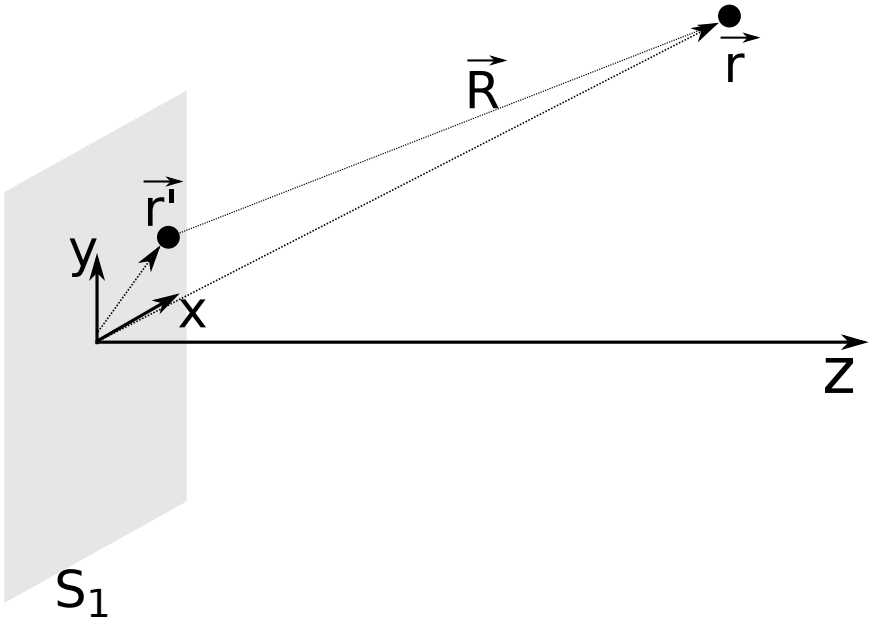

Figure 3.3: Diffraction geometry.

3.2.4 Approximations of Rayleigh-Sommerfeld diffraction integral

While Rayleigh-Sommerfeld diffraction integral shown in Eq. 3.20 is the rigorous solution for the scalar diffraction problem, it is difficult for numerical calculation. In this section, I will discuss two situations in which it can be approximated into formulas that are easy for numerical implementation. Both situations meet the following two conditions:

$$\begin{aligned} r &\gg r' \\ r &\gg \lambda \end{aligned} \tag{3.21}$$

where $r' = |\vec{r}'|$; $r = |\vec{r}|$.

In the first situation, there is an additional *paraxial* condition:

$$\frac{\sqrt{x^2+y^2}}{z} \ll \sqrt[4]{\frac{\lambda}{z}}. \tag{3.22}$$

Then Rayleigh-Sommerfeld diffraction integral Eq. 3.20 can be approximated by *Fresnel diffraction integral*:

$$\psi(x,y) \approx \frac{1}{i} e^{ikz} e^{i\frac{k}{2}\frac{1}{z}(x^2+y^2)} \frac{1}{\lambda z} \mathcal{F}[e^{i\frac{k}{2}\frac{1}{z}(x'^2+y'^2)} \psi(x',y')|_{S_1}]\big|_{(f_x=\frac{1}{\lambda}\frac{x}{z}, f_y=\frac{1}{\lambda}\frac{y}{z})}. \tag{3.23}$$

Here $\mathcal{F}$ denotes Fourier transform, and it is evaluated at a spacial frequency (f_x, f_y) depending on the coordinate of the position under consideration (x, y).

In the second situation, the additional condition is the *far field* condition:

$$r \gg z_R \equiv \frac{\pi r'^2}{\lambda} \tag{3.24}$$

Here I call z_R the Rayleigh range of the sample, similar to the definition of "Rayleigh range" for a Gaussian beam with waist radius r'. Then Rayleigh-Sommerfeld diffraction integral Eq. 3.20 can be approximated by what is termed *far field diffraction integral* in this thesis:

$$\psi(x,y) \approx \frac{e^{ikr}}{i} (\frac{1}{\lambda}\frac{z}{r^2}) \mathcal{F}[\psi|_{S_1}]\big|_{(f_x=\frac{1}{\lambda}\frac{x}{r}, f_y=\frac{1}{\lambda}\frac{y}{r})}. \tag{3.25}$$

Surprisingly, this situation is not treated in most textbooks, but it is more useful for the experiments covered in this thesis work than the frequently mentioned "Fraunhofer diffraction formula" in the literature. The latter requires both far field condition and the paraxial condition to be true, so it is limited to low NA situation.

3.2.5 2D Scalar diffraction with angular spectrum approach

Besides Green's function approach, there is another approach to solve the homogeneous Helmholtz equation Eq. 3.15: the so-called angular spectrum approach [45]. While Green's function approach works in the real space, the angular spectrum approach works in the Fourier space. We decompose the field at a certain plane with constant z into its plane wave components by using two-dimensional Fourier transform: $\psi(x,y,z) = \mathcal{F}^{-1}\{A(f_x,f_y,z),x,y\} = \iint \mathrm{d}f_x\,\mathrm{d}f_y e^{i2\pi(f_x x+f_y y)}A(f_x,f_y,z)$. We plug this in Eq. 3.15, and for the angular spectrum $A(f_x,f_y,z)$ we get:

$$(\partial_z^2 + f_z^2)A(f_x,f_y,z) = 0 \tag{3.26}$$

where

$$f_z = \sqrt{1-(\frac{1}{\frac{1}{\lambda}}f_x)^2-(\frac{1}{\frac{1}{\lambda}}f_y)^2}. \tag{3.27}$$

The solution is:

$$\begin{aligned} A(f_x,f_y,z) &= A(f_x,f_y,0)H(f_x,f_y) \\ H(f_x,f_y) &= e^{i2\pi f_z z}. \end{aligned} \tag{3.28}$$

For sub-wavelength spatial frequencies, or $\sqrt{f_x^2+f_y^2} > \frac{1}{\lambda}$, f_z is imaginary, and the wave experiences exponential decaying rather than increase of the phase when propagating along z and is called evanescent wave.

3.2.6 2D vectorial diffraction

Boundary conditions on the sample introduces coupling between $\vec{E}$ and $\vec{H}$, as well as their various scalar components. Scalar diffraction theory ignores this coupling and entails some degree of error. This error is significant when feature size is on the same order of the wavelength. Another scenario in which we should probably use vectorial diffraction theory is when polarization matters, such as a reflection geometry with non-normal incidence.

For vectorial diffraction solution, we start from wave equations Eq. 3.6, and with the aid of

a Green's function subject to Neumann boundary condition:

$$\vec{A} = \int_{S_1} \mathrm{d}s((-\frac{1}{2\pi}\frac{e^{ikR}}{R})\vec{n}\cdot\nabla\vec{A}) \tag{3.29}$$

In terms of $\vec{B}$, the above equation is equivalent to:

$$\vec{B} = \frac{1}{2\pi}\nabla\times\int_{S_1} \mathrm{d}s\frac{e^{ikR}}{R}\vec{n}\times\vec{B} \tag{3.30}$$

And based on symmetry between $\vec{B}$ and $\vec{E}$, we have (for $z>0$, $\vec{E}=\vec{E}_{\text{diff}}$ in Ref. [46] Eq. 10.101):

$$\vec{E} = \frac{1}{2\pi}\nabla\times\int_{S_1} \mathrm{d}s\frac{e^{ikR}}{R}\vec{n}\times\vec{E} \tag{3.31}$$

Under the same conditions we derive the far field diffraction integral Eq. 3.25, the above vectorial diffraction integral can be approximated by the following far-field vectorial diffraction formula:

$$\vec{E} = \frac{e^{ikr}}{i}\frac{1}{\lambda r}\mathcal{F}[E|_{S_1}](\vec{n}\times\hat{\epsilon}_i)\times\hat{r} \tag{3.32}$$

3.2.7 Non-normal incidence

Momentum transfer plays an important role in the evaluation of diffraction. In the framework constructed in this section, it is a natural result of Fourier shift theorem. For non-normal incidence, the exit surface (S_1: $z'=0$) wave has a linear phase shift across the plane, which we factor out in the following way:

$$\psi(x',y',z'=0) = e^{i2\pi(f_{0,x}x'+f_{0,y}y'}\psi_0(x',y') \tag{3.33}$$

Among the several two-dimensional scalar diffraction integrals that can be approximated using Fourier transforms, we choose the far field diffraction integral Eq. 3.25 for an example. We get:

$$\psi(x,y) \approx \frac{e^{ikr}}{i}(\frac{1}{\lambda}\frac{z}{r^2})\mathcal{F}[e^{i2\pi(f_{0,x}x'+f_{0,y}y'}\psi_0(x',y')]\big|_{(f_x=\frac{1}{\lambda}\frac{x}{r},f_y=\frac{1}{\lambda}\frac{y}{r})}. \tag{3.34}$$

With Fourier shift theorem:

$$\psi(x,y) \approx \frac{e^{ikr}}{i}(\frac{1}{\lambda}\frac{z}{r^2})\mathcal{F}[\psi_0(x',y')]\big|_{(f_x=\frac{1}{\lambda}\frac{x}{r}-f_{0,x},f_y=\frac{1}{\lambda}\frac{y}{r}-f_{0,y})}. \tag{3.35}$$

We see that the Fourier transform is performed at the "momentum transfer" frequencies, in other words, the final spatial frequency subtracting the initial spatial frequency.

3.2.8 3D diffraction with volume integral

This thesis mainly works on 2D imaging; yet, for completeness and comparison with 2D, the 3D diffraction is also discussed here. If the volume we choose contains the scatters, as shown in the second panel in Fig. 3.2, then we would work with the inhomogeneous wave equation Eq. 3.8 with the right-hand side unequal to 0.

Similar to the way we get Eq. 3.14 for $\vec{E}_\omega$, for $\vec{D}_\omega$:

$$\vec{D}_\omega(\vec{r}) = \oint_S \mathrm{d}\vec{r'}(G(\vec{r},\vec{r'})\partial'_n\vec{D}_\omega(\vec{r'}) - \vec{D}_\omega(\vec{r'})\partial'_n G(\vec{r},\vec{r'})) + \int_V \mathrm{d}\vec{r'} G\vec{f}_{sD} \tag{3.36}$$

where

$$\vec{f}_{sD} = -\vec{\nabla}\times(\vec{\nabla}\times\vec{P}) - i\omega\epsilon_0\mu_0\vec{\nabla}\times\vec{M} \tag{3.37}$$

With S chosen to be infinitely large sphere, using Sommerfeld radiation condition, the surface integral would vanish. We choose the Green's function $G = G_k$ as defined in Eq. 3.19, then under the conditions:

$$\begin{aligned} r &\gg r' \\ r &\gg z_R \end{aligned} \tag{3.38}$$

we have:

$$\vec{D}_s(\vec{r}) = \frac{1}{4\pi}\frac{e^{ikr}}{r}k^2\mathcal{F}[\vec{f}_{sD1}]|_{\vec{f}=\frac{1}{\lambda}\hat{r}} \tag{3.39}$$

where

$$f_{sD1} = \vec{n}\times\vec{P}\times\vec{n} - \frac{1}{c}\vec{n}\times\vec{M} \tag{3.40}$$

The total field $\vec{D} = \vec{D}_0 + \vec{D}_s$, where D_0 is the incident wave, and D_s is the scattered save. We then use *Born approximation*:

$$\vec{D}_s \ll \vec{D}_0 \tag{3.41}$$

which means the scattering wave is much weaker than the indicident wave. For linear and isotropic medium, weak scattering means $\chi \ll 1$ and $\chi_B \equiv \mu - 1 \ll 0$. Then the source term can be approximated by:

$$f_{sD1} \approx \vec{n}\times\chi\vec{D}_0\times\vec{n} - \frac{1}{c}\vec{n}\times(\chi_B c\frac{1}{ik}\vec{\nabla}\times\vec{D}_0) \tag{3.42}$$

Equation 3.39 with the source term approximated by Eq. 3.42 provides the solution of diffraction under Born approximation with a 3D integral.

For 3D CDI, there are two approaches. In the first approach, 2D diffraction slices are assembled into a 3D diffraction volume, then images are reconstructed with phase retrieval algorithms with diffraction formulas similar to the one given above (assembling before reconstructing). This approach is used in Ref. [52] for example. For the X-ray wavelength, the index of refraction is close to 1; and if the sample is relatively thin as is true in this work, the Born approximation condition is satisfied, while for other cases, it can fail. Then it is favorable to use the second approach: First 2D projection images are reconstructed at different orientation angles; then using the computed tomography approach to obtain the 3D structure (reconstructing before assembling). The second approach is used in several works on ptychographic X-ray computed tomography [53, 54].

3.2.9 Summary of 2D diffraction formulas

Here I give a summary of the 4 key results and their conditions for 2D diffraction problems. They are Fresnel diffraction integral, far field scalar diffraction integral, angular spectrum diffraction formula, and far field vectorial diffraction integral, respectively:

$$\vec{E}(\vec{r}) = \begin{cases} \frac{1}{i}e^{ikz}e^{i\frac{k}{2}\frac{1}{z}(x^2+y^2)}\frac{1}{\lambda z}\mathcal{F}[e^{i\frac{k}{2}\frac{1}{z}(x'^2+y'^2)}\vec{E}|_{S_1}], & \text{Fresenl, } r \gg \max[r', \lambda]; \frac{\sqrt{x^2+y^2}}{z} \ll \sqrt[4]{\frac{\lambda}{z}} \\ \frac{e^{ikr}}{i}\frac{z}{\lambda r^2}\mathcal{F}[\vec{E}|_{S_1}] & \text{Far field scalar, } r \gg \max[r', \lambda]; z \gg \frac{\pi r'^2}{\lambda} \\ \mathcal{F}^{-1}\left[\exp[i2\pi\frac{1}{\lambda}z\sqrt{1-(\frac{1}{\frac{1}{\lambda}}f_x)^2-(\frac{1}{\frac{1}{\lambda}}f_y)^2}]\cdot\mathcal{F}[\vec{E}|_{S_1}]\right] & \text{Angular spectrum,} \\ \frac{e^{ikr}}{i}\frac{1}{\lambda r}\mathcal{F}[E|_{S_1}](\vec{n}\times\hat{\epsilon}_i)\times\hat{r} & \text{Far field vectorial, } r \gg \max[r', \lambda]; z \gg \frac{\pi r'^2}{\lambda} \end{cases} \tag{3.43}$$

For numerical calculations, there might be more constraints on their applicability range. For example, although the angular spectrum diffraction formula is a rigorous across the whole space, difficulty is met when it is applied to far field. This is because the transfer function has fast oscillation in the phase and cannot be well sampled in this situation.

For Fresnel diffraction integral, it is convenient if the diffraction plane has a field of view at least that of the sample plane; in other words: $\lambda z/\Delta x_{\mathrm{Smp}} > D_{\mathrm{Smp}}$. So

$$z > z_F \equiv \frac{\Delta x_{\mathrm{Smp}}}{\lambda} D_{\mathrm{Smp}} \tag{3.44}$$

The applicability of different diffraction formulas is shown in Fig. 3.4.

3.3 Iterative algorithms for diffraction phase retrieval

This section discusses the second part of the theories behind CDI: the iterative algorithms that retrieve the phase of diffraction patterns. The basic idea is illustrated in Fig. 3.5. Each full iteration cycle, or updating cycle, is composed of two successive single projections: the projection onto the detector plane constraint set, or the modulus constraint set, P_m; and the projection onto the sample domain constraint set P_s.

Both single-diffraction CDI and ptychography CDI makes use of the same detector-plane constraint: the modulus constraint, meaning that the modulus of the diffracted field has to be equal to what is measured by the detector. They differ in the sample plane constraints: single-diffraction CDI makes use of finite support constraint while ptychography CDI uses "overlap constraint". In this section, each of these three constraints and its corresponding projection is investigated separately first. Then algorithms that assemble two successive single projections into a full iteration cycle are presented.

For ease of discussion, the relationship between the sample plane and the detector plane can be expressed as:

$$U = \mathcal{T} u \tag{3.45}$$

where

- u is a quantity related to the sample to be reconstructed;
- U is a quantity related to the detected diffraction intensity (or counts);
- $\mathcal{T}$ is a transform, or a propagator that calculates U from u.

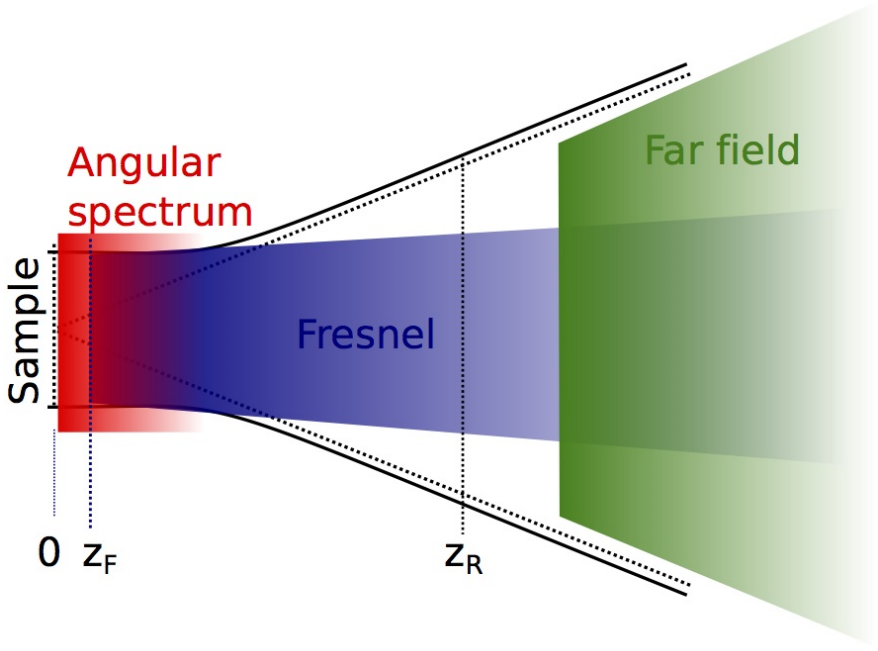

Figure 3.4: Applicability of different diffraction formulas for numerical calculations. Angular spectrum formula performs well in the near field; Fresnel diffraction integral performs well after z_F for low numerical aperture; Far field diffraction integral, both scalar and vectorial, should be preferred for the far field region for any numerical aperture.

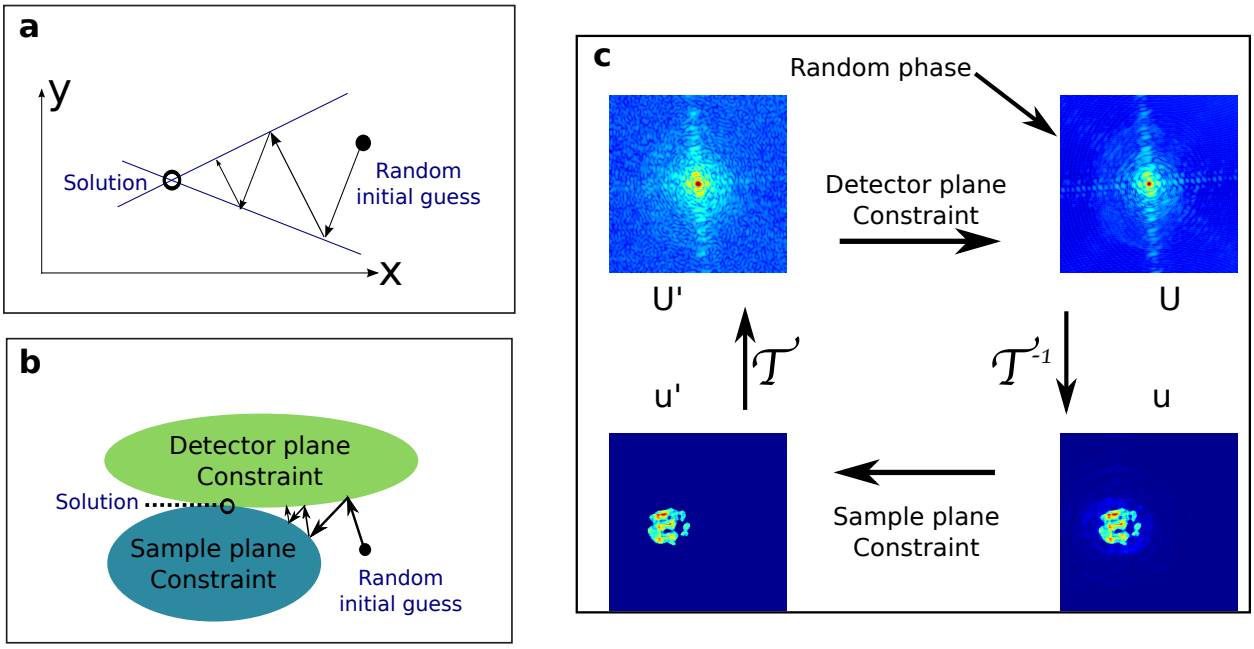

Figure 3.5: Illustration of the iterative phase retrieval algorithms used in CDI. (a) A simple example for solving two linear equations. A random staring point, after successive projections to one and then the other line, finally will arrive at the intersection which is the solution subject to the two constraint sets represented by the two lines. (b) In CDI, a random guess is first projected to the detector plane constraint set, then to the sample plane constraint set to finish a full updating cycle. After many iterations, the solution is found at the intersection of the two constraint sets. (c) A simple specific implementation of the approach of iterative projections in CDI. The phase is not measured on the detector, so a random phase distribution is assigned to the measured modulus to form E_{Detector} as a staring point. The complex wave is then propagated to the sample plane using a transform $\mathcal{T}$ based on diffraction theory. Then the sample plane constraint is applied. The new sample field E_{Sample} is then propagated to the detector plane with $\mathcal{T}$. The phase of the updated E_{Detector} is kept while its modulus is replaced by the measured one, to form a new wave on the detector. This process is repeated until the algorithm converges.

3.3.1 Projection onto the modulus constraint set on the detector plane

For P_m, assuming u is the exit surface wave (here we focus on two-dimensional diffraction) to be reconstructed, projection to the modulus constraint set simply requires the modulus of U to be replaced with the measured modulus, $|U|_m$. This projection, or updating rule, can be expressed as:

$$P_m u = \mathcal{T}^{-1}[|U|_m \exp\{i\phi(\mathcal{T}[u])\}] \tag{3.46}$$

Basically, we propagate u from the sample plane to the detector plane to get U, keep its phase while replacing its magnitude with the measured values, and then propagate back to finish this single projection.

3.3.2 Projection onto the support constraint set on the sample plane in single-diffraction CDI

For P_s in single-diffraction CDI, it is the projection to the support constraint set: the exit surface wave u has to have a finite support S, outside which $u = 0$. The realization of this projection $P_{s,\text{Support}}$is very straightforward: we simply set u outside S to be zero:

$$P_s u = S \cdot u \tag{3.47}$$

where S is the mask for the support; it is 1 inside the support and 0 outside the support. There are several ways to obtain S. It can be from an image of the sample from a lower resolution, optical microscope, although this method requires a separate measurement. It can be from the autocorrelation, which is at most twice the object size. Marchesini [55] devised an automatically updating method, the "shrink-wrap" method that works really well. In this method, the support is created by thresholding the amplitude $|u|$ at a certain level (4%, for example) followed by convoving with a Gaussian function.

In practice, the finite support constraint alone does not work well enough. Indeed, it is simply not a powerful enough constraint. Combinations with other sample-plane constraints based on some *a priori* information greatly enhances the convergence of the iterative reconstruction. One

typical example of this extra sample-plane constraint is the positivity constraint, or more generally, the phase constraint: the phase of the sample or the exit-surface wave is within a certain range. In Ref. [27], I provided a unified approach that combines the projections to the conventional amplitude constraint and the phase constraint in the sample plane. Besides the amplitude support, one can create an additional "phase support" S_{Phase}. For pixels that have their phase within the known range, $S_{\text{Phase}} = 1$, and otherwise it is 0. We use the new combined support, which is the product of $S = S_{\text{Amplitude}}$ and S_{Phase}, instead of only $S_{\text{Amplitude}}$ when doing projection P_s as shown in Eq. P_s. For objects for which phase variation is much less than 2π, or any essentially binary object, this approach can be readily applied. In our keyhole CDI results shown in Chapter 4, we used this approach in our reconstruction.

3.3.3 Projection onto the "overlap" constraint set on the sample plane in ptychography CDI

P_s in ptychography CDI is the projection to the "overlap" constraint set: for any two diffractions at two scan positions that have overlap, the retrieved phases have to yield reconstructed sample images that are the same in the overlapped region.

For the transmission geometry, specifically for j^{th} scanning position R_j, Eq. 2.4 can be written as:

$$E_{t,j}(\vec{r}') = E_i(\vec{r}') \cdot t(\vec{r}' - \vec{R}_j) \tag{3.48}$$

or

$$t(\vec{r}' - \vec{R}_j) = \frac{E_i^*(\vec{r}')}{|E_i(\vec{r}')|^2} E_{t,j}(\vec{r}') \tag{3.49}$$

where E_i^* means the complex conjugate of E_i.

There can be two types of ptychographical projection derived from the above simple equation: the parallel projections algorithm [42], and the extended ptychographical iterative engine (ePIE) [56]. Both the sample and the incident beam can be reconstructed by ptychography algorithms.

(1) In parallel projections algorithm, t is updated using data from all the positions by a single

step:

$$\begin{cases} t(\vec{r}') = \frac{\sum_j E_i^*(\vec{r}'+\vec{R}_j)E_{t,j}(\vec{r}'+\vec{R}_j)}{\sum_j |E_i(\vec{r}'+\vec{R}_j)|^2} \\ E_i(\vec{r}') = \frac{\sum_j [E_{t,j}(\vec{r}')\cdot t^*(\vec{r}'-\vec{R}_j)]}{\sum_j |t(\vec{r}'-\vec{R}_j)|^2} \end{cases} \tag{3.50}$$

(2) In ePIE, t and Ei are updated at one scanning position after another, in a serial version.

$$\begin{cases} t_{n+1}(\vec{r}' - R_j) = t_n(\vec{r}' - R_j) + \alpha \frac{E_i^*(\vec{r}')}{\max |E_i(\vec{r}')|^2}[E_{t,j,n+1}(\vec{r}') - E_{t,j,n}(\vec{r}')] \\ E_{i,n+1}(\vec{r}') = E_{i,n}(\vec{r}') + \beta \frac{t^*(\vec{r}'-\vec{R}_j)}{\max |t(\vec{r}'-\vec{R}_j)|^2}[E_{t,j,n+1}(\vec{r}') - E_{t,j,n}(\vec{r}')] \end{cases} \tag{3.51}$$

where α and β are relaxation parameters; subscripts n and $n+1$ means the nth and $n+1$th iteration.

In this section, E_t plays the same role as the previously used symbol u, both meaning the exit-surface wave. With the updated E_i and t provided above, their multiplication will provide the updated E_t or u, completing a full single projection $P_{s,\text{Ptychography}}$. It is not explicitely given here, as it is more convenient to use the above updating formulas Eq. 3.50 or Eq. 3.51.

The above discussion in the transmission geometry can be easily extended to the reflection geometry by replace t with r.

3.3.4 Combining two projections for a full iteration cycle

Given projections onto a single constraint set, either on the detector plane, or on the sample plane, different algorithms exist to combine the two successive consecutive projections to form a full iteration of reconstruction (or updating): error reduction (ER) [25], hybrid input-output (HIO) [25], relaxed averaged alternating reflections (RAAR) [57], and difference map [26]. The combined projections for these different algorithms are presented in Table 3.3.4. A good review and comparison of these different algorithms can be found in Ref. [58] by Marchesini. In this paper, Marchesini also gave an intuitive explanation of how these projections work, by providing a geometric representations, with two straight lines representing the two constraint sets, and their intersection representing the desired solution. This geometric representation is shown in Fig. 3.6

Table 3.2: Summary of different algorithms for two successive projections. β is a relaxation parameter. $[P_1, P_2]$ can be either $[P_m, P_s]$ or $[P_s, P_m]$.

Algorithm	Combined projection
Error reduction	P_1P_2
Hybrid input-output	$((1+\beta)P_s - \beta)P_m + 1 - P_s$
Relaxed averaged alternating reflections	$\frac{1}{2}\beta((2P_s-1)(2P_m-1)+1) + (1-\beta)P_m$
Difference map	$1 + \{P_1[(\beta+1)P_2 - 1] - P_2[(\beta-1)P_1 + 1]\}$

In this thesis work, for single-diffraction CDI, the RAAR algorithm is used most frequently; while for ptychography CDI, ePIE projection Eq. 3.51 combined with the error reduction algorithm is chosen for image reconstruction.

3.4 Numerical implementations

To numerically implement the phase retrieval algorithms described in the previous section, it is desirable to find u, $|U|_m$ (magnitude of U from the measurement), and $\mathcal{T}$ that satisfies:

$$|\mathcal{T}u| = |U|_m \tag{3.52}$$

where

(1) the whole equation $U = \mathcal{T}u$ is equivalent to one of the diffraction formulas given in Eq. 3.43.

(2) U is some quantity that can be derived from the counts on the detector;

(3) u is some quantity that relates to the sample;

(4) $\mathcal{T}$ is a transform that can be realized by the Fast Fourier Transform (FFT) algorithm which is computationally efficient.

To achieve this, it is first necessary to establish the relationship between the detector counts distribution N with the electric field complex amplitude $\vec{E}$, since the diffraction formulas in Eq. 3.43 are written in terms of electric field.

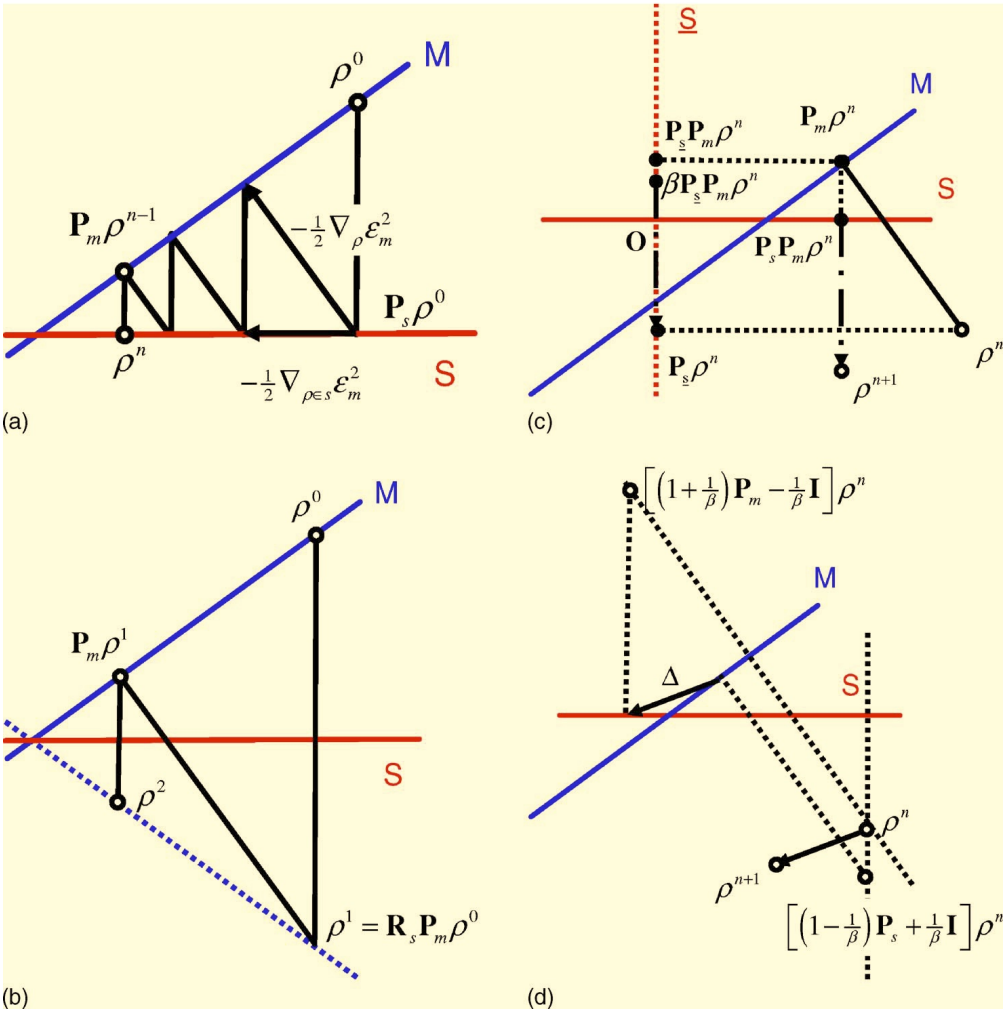

Figure 3.6: Geometric representation of combined projections onto two constraint sets that are represented by two lines intersecting. (a) Error reduction algorithm. (b) HIO algorithm. (c) Error reduction algorithm with a reflector rather than a projector. (d) Difference map algorithm. The symbol ρ here plays the same roles as u in the text. Figure adapted from Marchesini [58].

$$N(\vec{r}) = \eta \Delta t p^2 \hat{n} \cdot \frac{1}{h\nu} \vec{S}(\vec{r}) \tag{3.53}$$

where $N(\vec{r})$ means the count on a detector pixel located at position $\vec{r}$, η is the efficiency for the detector pixel to convert a photon to a count, Δt is the exposure time, p is the width of the pixel which is assumed to be square, $\hat{n}$ is the normal vector of the detector, ν is the frequency of the beam, and $\vec{S}$ is the time-averaged Poynting vector of the beam. Since

$$\vec{S}(\vec{r}) = \frac{1}{2Z_0} |E(\vec{r})|^2 \hat{k} \tag{3.54}$$

where Z_0 is the impedence of free space $\sqrt{\mu_0/\epsilon_0} \approx 377\,\Omega$; $\hat{k}$ is normalized wave vector. Then

$$|E(\vec{r})| = \sqrt{\frac{1}{\eta \frac{1}{h\nu} \frac{1}{2Z_0} p^2}} \sqrt{\frac{1}{\hat{n}_{CCD} \cdot \hat{k}} \frac{N(\vec{r})}{\Delta t}} \tag{3.55}$$

Now that the relationship between the directly measured counts N and the electric field amplitude $|E|$ is established, we can combine it with the diffraction formulas shown in Eq. 3.43. Here we choose the far field scalar diffraction formula for discussion, and the extension to other formulas is straightforward.

$$\begin{aligned} |E_{\mathrm{Det}}(\vec{r})| &= \sqrt{\frac{1}{\eta \frac{1}{h\nu} \frac{1}{2Z_0} p^2}} \sqrt{\frac{1}{\hat{n}_{CCD} \cdot \hat{k}} \frac{N(\vec{r})}{\Delta t}} \\ &= \left| [\tfrac{1}{i} e^{ikr}] \tfrac{z}{\lambda r^2} \mathcal{F}[E_{\mathrm{Smp}}] \big|_{f_x \equiv \frac{1}{\lambda} \frac{x}{z_{ds}} - f_{0x}, f_y \equiv \frac{1}{\lambda} \frac{y}{z_{ds}} - f_{0y}} \right| \end{aligned} \tag{3.56}$$

It is then useful to examine the relationship between Fourier transform and the FFT algorithms used in numerical calculations. In MATLAB, for example, it is evaluated with the function "fft2" for the two-dimensional case. It is useful to see the exact relationship between Fourier transform and what FFT provides. We consider a two-dimensional complex function $g(x, y)$, sampled on a grid with uniform distance in both x and y directions:

$$\begin{aligned} x_{j_x} &= x_1 + (j_x - 1)\Delta x, \quad j_x = 1, 2, \ldots N_x \\ y_{j_y} &= y_1 + (j_y - 1)\Delta y, \quad j_y = 1, 2, \ldots N_y \end{aligned} \tag{3.57}$$

Then, the Fourier transform can be calculated with "fft2" using:

$$\mathcal{F}[g(x, y)] = \Delta x \Delta y [\text{fftshift fft2 ifftshift } g(x, y)] \tag{3.58}$$

where "fftshift" is the function shifting the zero frequency to the center of the grid, and "ifftshift" is inverse function. The corresponding spatial frequency grid is:

$$\begin{aligned} f_{x,j_{f_x}} &= f_{x,1} + (j_{f_x} - 1)\Delta f_x, \quad j_{f_x} = 1, 2, \ldots N_x; \\ f_{y,j_{f_y}} &= f_{y,1} + (j_{f_y} - 1)\Delta f_y, \quad j_{f_x} = 1, 2, \ldots N_x. \end{aligned} \tag{3.59}$$

Here $\Delta f_x = \frac{1}{N_x \Delta x}$, $\Delta f_y = \frac{1}{N_y \Delta y}$, $f_{x,1} = -\text{floor}[\frac{N_x}{2}]$, $f_{y,1} = -\text{floor}[\frac{N_y}{2}]$. For convenience, we define

$$\text{FT}_2 \equiv \text{fftshift fft2 ifftshift} \ . \tag{3.60}$$

Then Eq. 3.58 becomes:

$$\mathcal{F}[g(x,y)] = \Delta x \Delta y \text{FT}_2[g(x,y)] \tag{3.61}$$

Using the derived relationship shown in Eq. 3.61, Eq. 3.56 can be rewritten as:

$$\left| \text{FT}_2[c_{\text{NFT}} E_{\text{Smp}}] \right|_{f_x = \frac{1}{\lambda}\frac{x}{r} - f_{0x}, f_y = \frac{1}{\lambda}\frac{y}{r} - f_{0y}} = \frac{\lambda r^2}{z} \sqrt{\frac{1}{\hat{n} \cdot \hat{k}} \frac{N(\vec{r})}{\Delta t}} \tag{3.62}$$

where the constant $c_{\text{NFT}} = \Delta x_{\text{Smp}} \Delta y_{\text{Smp}} \sqrt{\eta \frac{1}{h\nu} \frac{1}{2Z_0} p^2}$ So for far field scalar diffraction, u, U_m, and T in search are:

(1) $u = c_{\text{NFT}} E_{\text{Smp}}$ (proportional to ESW E_{Smp}) immediately the sample plane.

(2) $U_m = \frac{\lambda r^2}{z} \sqrt{\frac{1}{\hat{n} \cdot \hat{k}} \frac{N(\vec{r})}{\Delta t}}$; After this calculation from $N(\vec{r})$, it should be then remapped from a unequally spaced spatial frequency grid $f_x = \frac{1}{\lambda}\frac{x}{r} - f_{0x}, f_y = \frac{1}{\lambda}\frac{y}{r} - f_{0y}$ to a chosen uniformly spaced spatial frequency grid which is required by FFT. This procedure is described in Ref. [59]. More recently, I together with others have filed a provisional application for a patent on a faster and potentially more accurate version [60]. The increased speed offered by this version is important for fast diffractive imaging, especially real-time diffractive imaging.

Usually some pre-processing steps for the raw measured diffraction patterns need to happen beforehand, such as removing the dark frame background, removing hot pixels due to cosmic rays with median filtering, and combining short(unsaturated) and long(saturated) exposures for high dynamic range (HDR).

(3) $\mathcal{T} = \mathrm{FT}_2$.

We will see in Chapter 4 that u and $\mathcal{T}$ can be slightly modified so that the amplitude or phase support constraint can be directly imposed.

The remapping used in obtaining U_m can be easier to understand with the help of Ewald sphere analysis. Figure 3.7 illustrates the way that spatial frequencies mapped onto the detector grid for three different situations: normal incidence with low numerical aperture, normal incidence with high numerical aperture, non-normal incidence with high numerical aperture. We see that along with the increasing of the numerical aperture (or scattering angle), the mapping from frequency to the detector grid is not linear anymore. The diffraction pattern needs to be remapped to a linear grid to be compatible with the FFT algorithm.

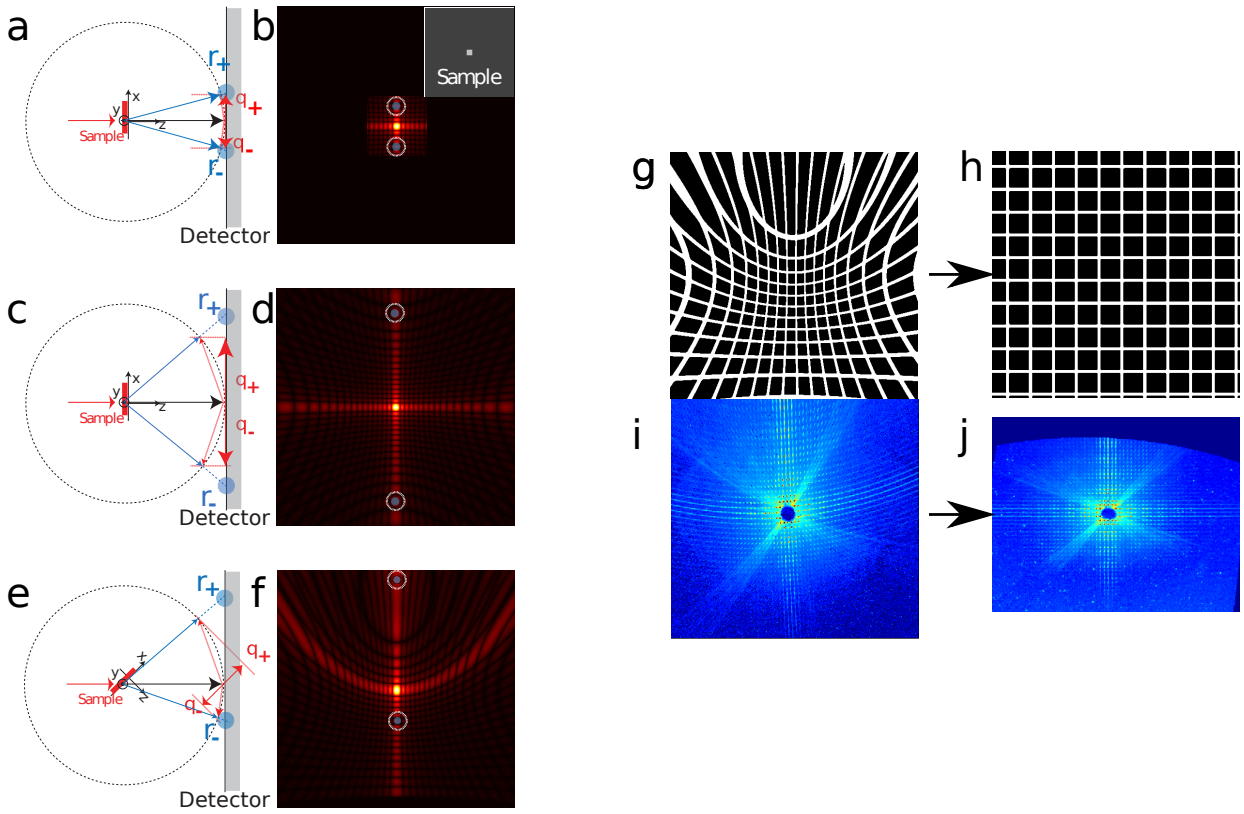

Figure 3.7: Illustration of the mapping from spatial frequencies to the detector grid for three different situations. (a) Normal incidence with small angle scattering. (b) Simulated diffraction pattern for a square mask function. The mapping from spatial frequency $q_{\pm}$ to the detector grid is symmetric and linear. (c) and (d) are for normal incidence but with high angle scattering. The mapping from $q_{\pm}$ to the detector grid is nonlinear but still symmetric. (e) and (f) are for non-normal incidence, high angle scattering. The mapping is nonlinear, and asymmetric. The calculated nonlinear frequency grid is shown in (g), and the chosen equally spaced spatial frequency grid is shown in (h). The measured diffraction pattern (i) leads to a corrected one shown in (j), after remapped from grid (g) to (h), to be compatible with the FFT algorithm.

Chapter 4

Keyhole CDI for Extended Samples in Transmission

Single-diffraction CDI requires the sample to be on a finite support, or isolated, which presents a severe limitation to this imaging method. Several techniques have been developed to overcome this limitation, including ptychography CDI [61], keyhole CDI [62], and apertured illumination CDI [59]. As we have seen previously, in ptychography CDI, adapted from an electron beam technique and later demonstrated using a synchrotron light source [61], a beam is scanned across an object. The additional information provided by the overlap between adjacent scans is then used to reconstruct one large field-of-view image. Keyhole CDI, first demonstrated using light from a synchrotron source, uses a FZP focusing optic with smaller diameter than the incident beam to confine the illumination on the sample [62]. Finally, apertured illumination CDI projects an image of an aperture onto the sample plane to ensure isolated illumination. This technique requires high quality focusing optics and also a precise determination of the imaging plane of the aperture, and has been demonstrated using a He-Ne laser [59].

In this chapter, initial attempts for imaging extended samples with apertured illumination CDI are described. While we achieved success with visible light, we were not able to implement this approach with HHG sources, as this technique is more demanding than keyhole CDI. The next following sections will focus on our implementation of the keyhole CDI technique with a HHG source. It enabled the first general tabletop EUV coherent microscope that can image extended, non-isolated, non-periodic, objects. By implementing keyhole coherent diffractive imaging with curved mirrors and a tabletop high harmonic source, we achieve improved efficiency of the imaging

system as well as more uniform illumination at the sample, when compared with using Fresnel zone plates. Moreover, we show that the unscattered light from a semi-transparent sample can be used as a holographic reference wave, allowing quantitative information about the thickness of the sample to be extracted from the retrieved image. Finally, we show that excellent tabletop image fidelity is achieved by comparing the retrieved images with scanning electron and atomic force microscopy images, and show superior capabilities in some cases.

4.1 Apertured illumination CDI: first attempts for imaging extended samples

As discussed before, conventional CDI relies on the samples to satisfy the "isolation constraint", or "support constraint", i.e., features exists in a small, isolated region, outside which, the electric field is zero. Instead of requiring the sample to be isolated, we transform the beam so it is isolated in a finite area, and ideally has a relatively sharp edge to form a top-hat shape. Our first attempt to implement this idea is to directly image an aperture to the sample plane, which we term "apertured illumination CDI" (AICDI).

In order to implement and test the AICDI technique and data processing algorithms, we first developed a proof-of-concept system using a polarized 632.8 nm HeNe laser. A schematic diagram of the setup is shown in Fig. 4.1(a). First we spatially filter and collimate the beam to overfill a 300 μm wide circular aperture. The aperture is imaged to the sample plane using a one-to-one 4f imaging system. A positive lens placed directly after the sample sends the scattered light into the Fourier plane at the CMOS detector (Mightex Systems MCE-B013, 5.2 μm pixel size). In general the positive lens after the sample is unnecessary, however, the detectors used in this experiment were small enough that a demagnification of the far field was required in order to use a wavelength as large as 633nm. The aperture size is selected to satisfy the oversampling criterion, where the distance between the lens and the detector is 11.6 mm, corresponding to an NA of 0.22 for with our 5.3 mm diameter detector.

We illuminated a bundle of suspended, 26 μm diameter copper wires with an image of the aperture (Fig. 4.1(a) inset). An example of a scatter pattern obtained is shown in Fig. 4.1(b). The

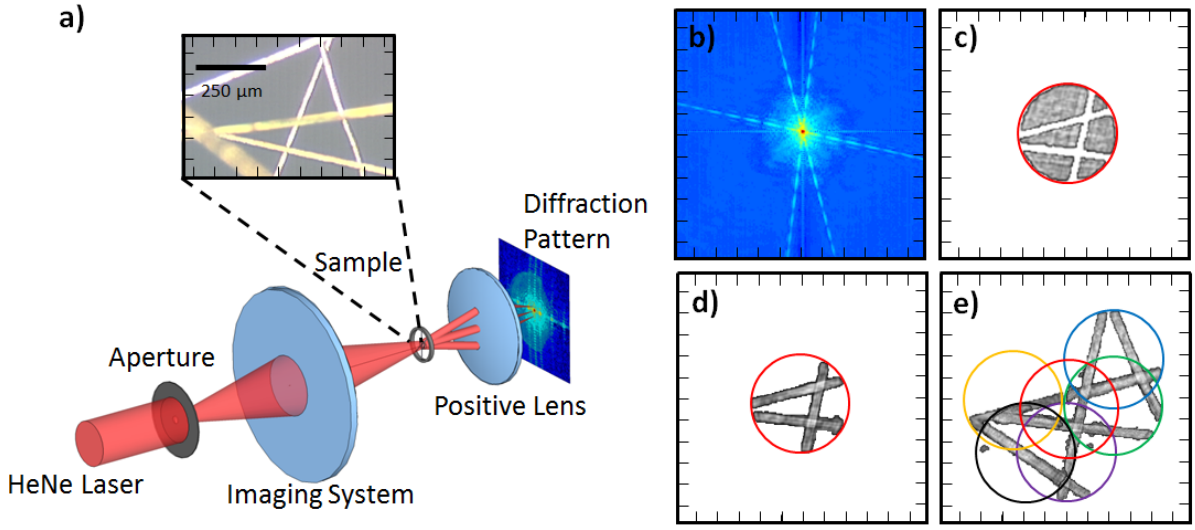

Figure 4.1: The apertured illumination CDI scheme isolates an extended transparent sample by imaging a aperture onto the sample plane. (a) A schematic of the setup, including a traditional bright-field microscope image of the sample. (b) The scatter pattern recorded by the detector in the Fourier plane scaled by the fourth root. (c) The exit surface wave reconstructed from the scatter pattern. The circle outlines the area illuminated by the aperture. (d) A reconstruction when the illumination is subtracted out. (e) Overlay of the images from many scan positions. The circles represent the outline of the aperture illumination at different scan positions. Figure reproduced from Gardner *et al.* [59].

scatter pattern we obtain is proportional to the modulus of the Fourier transform of the illuminated portion of the sample. We use the RAAR algorithm as outlined in Ref. [57] (including the correct form of non-negativity, a fast ramp in the feedback parameter and a modified amplitude constraint) with "shrinkwrap" [55] to recover the phase. With the recovered phase, we are able to reconstruct the exit surface wave (Fig. 4.1(c)). This technique constitutes a bright-field imaging microscope. If instead we first record the scattered light with the sample removed (leaving the rest of the system unchanged) and reconstruct the electric field at the image plane of the aperture, then during the reconstruction process we can subtract the complex amplitude of the illumination at the detector plane per iteration. Subtracting out the illumination results in the wires appearing bright instead of dark (Fig. 4.1(d)); this constitutes a dark-field microscope. By scanning the sample in a plane perpendicular to the optical axis, we are able to reconstruct different areas of the extended sample independently. With overlap between the scan positions, we can register adjacent reconstructions to build up a large-area, high-resolution image. Figure 4.1(e) shows a number of reconstructions of this sample, which were overlaid in post-processing. Colored circles indicate the area that was illuminated by the imaged aperture for each individual reconstruction.

4.2 Keyhole CDI for extended samples

In keyhole CDI, an aperture is inserted into the beam to isolate the illumination, similar to apertured-illumination CDI. However, it does not require the aperture to be exactly imaged onto the sample plane. Instead, the sample is put wherever there is significant phase curvature, which helps for the robustness of reconstruction [62, 63]. This techniqure requires the phase of the beam to be characterized carefully.

First, we demonstrated keyhole CDI with a tabletop HHG EUV source using a sample with an opaque background. A schematic diagram of the setup in the imaging chamber is shown in Fig. 4.2(a). We focused a 25 fs pulse duration, 1 mJ pulse energy, 3 kHz repetition-rate, Ti:sapphire laser beam with wavelength centered around 780 nm, into a 150 μm diameter hollow waveguide filled with Ar gas to generate phase-matched, spatially coherent, harmonics at wavelengths near 29

nm. After the waveguide, the HHG beam and CDI microscope were in medium vacuum ($\approx 10^{-6}$ torr) to avoid absorption of the EUV light from air. We used a pair of silicon mirrors oriented at near the Brewster's angle for the 780 nm light to effectively absorb the unconverted 780 nm light while reflecting the EUV beam. The 780 nm light was further filtered out by two 200 nm thick aluminum filters. The harmonics of only odd orders [18] are separated in energy by about 3 eV (twice of the fundamental 780 nm photon energy), and only one harmonic (27th order) was selected and focused on the sample with a flat and a curved EUV multilayer mirror (radius of curvature 25 cm). The EUV mirrors have a full width at half maximum (FWHM) bandwidth of 2.1 eV centered around 43.2 eV (corresponding to a wavelength of $\lambda = 28.7$ nm). Typically, a single EUV harmonic at this photon energy has a FWHM bandwidth of about 0.4 eV (a representative spectrum of EUV harmonics can be found in [19]), corresponding to a longitudinal coherence length of $L_c = \lambda^2/\Delta\lambda = 3.1$ μm. This means that for a field of view (FOV) D at the sample, the maximum scattering angle $\theta_{\max}$, limited by finite L_c, is determined by $\tan\theta_{\max} = 2L_c/D$ (See [64]. Notice here we use a different definition of L_c, and do not use the approximation of $\tan\theta \approx \theta$ when θ is small). For all the experiments performed in this paper, $D \leq 25$ μm. For $D = 25$ μm, the NA is required to be ≤ 0.3, which is greater than the experimental NA used in this section (0.23) as well as that in next section (0.20).

The EUV mirror pair has generally higher throughput than the FZP used in conventional keyhole CDI, while also inducing a curved wavefront that is very beneficial for the reconstruction algorithm [65]. The non-normal incidence of the HHG beam on the EUV curved mirror produces some astigmatism in the beam. A 50 μm diameter pinhole was placed about 2 mm before the horizontal focus (x-focus) to introduce a sharp edge on the HHG beam and enforce the isolation requirement on the illumination, rather than the sample. We measured the positions of the x-focus and y-focus with ±50 μm accuracy by use of the pinhole as a knife-edge scanner. The separation of x-focus and y-focus was measured to be ≈ 0.55 mm. The sample was composed of a 100 nm thick gold layer (which has a negligible transmission of 5×10^{-5} for 28.7 nm light), deposited on a thin Si_3N_4 membrane. Features were etched into the gold layer, as shown in the dark areas in Fig.

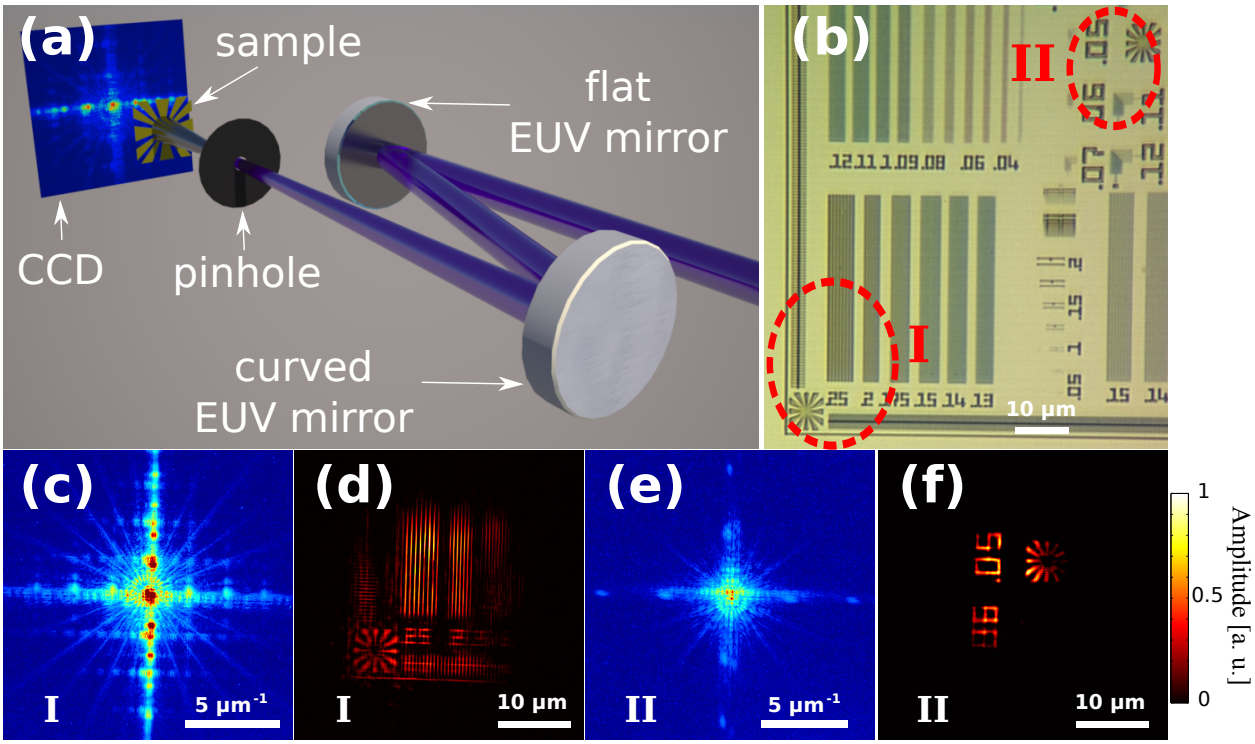

Figure 4.2: Tabletop EUV keyhole CDI of a sample with an opaque background. (a) Setup in the CDI vacuum chamber. The EUV mirror with a 25 cm radius of curvature focuses the HHG beam, and puts a curved wavefront on the sample. A pinhole placed before the x- and y-foci introduces a sharp edge onto the beam. (b) Image of the sample using a high magnification optical microscope. Two regions of interest, I and II, are circled, with corresponding measured diffraction patterns (cropped and centered) shown in (c) and (e), and their corresponding reconstructions of the electric field amplitude (normalized to unity at maximum with arbitrary units) shown in (d) and (f). The color map as shown on the right of (f) is shared by (d) and (f). Figure reproduced from Zhang *et al.* [27].

4.2(b). Keyhole CDI enables the imaging of any region of interest on such an extended sample; here we selected region I and region II as indicated in Fig. 4.2(b). The imaging FOV can be adjusted by placing the sample at different distances from the focus positions, which corresponds to different HHG beam spot sizes. For the measured diffraction shown in Figs. 4.2(c) (for region I) and 4.2(e) (for region II), the sample was placed 1.3 mm and 0.9 mm downstream of the circle of least confusion (the midpoint of x- and y- foci) respectively, resulting in a FOV of $D \approx 25$ μm and $D \approx 18$ μm. The diffraction patterns were recorded on an X-ray CCD (Andor iKon-L, 2048 × 2048 pixel array, 13.5 × 13.5 μm^2 pixel size), as shown in Figs. 4.2(c) and 4.2(e), with a total exposure time of 30 minutes for each. The CCD was positioned at a distance of 44.6 mm from the circle of least confusion.

For experiments performed in this section, NA ≈ 0.23, and the calculated D/NA is 104 μm for Fig. 4.2(c) and 75 μm for Fig. 4.2(e), both of which are much greater than the thickness of the sample (≈ 150 nm), so Eq. (2.4) is valid. The electric field at (x, y) position on the detector plane is given in the paraxial Fresnel approximation by

$$E_{t,\mathrm{Det}}(x,y) = \frac{e^{i\frac{2\pi}{\lambda}z}}{i\lambda z} e^{i\frac{\pi}{\lambda z}(x^2+y^2)} \iint_{-\infty}^{\infty} e^{-i\frac{2\pi}{\lambda z}(xx'+yy')} e^{i\frac{\pi}{\lambda z}(x'^2+y'^2)} E_{t,\mathrm{Smp}}(x',y')\,\mathrm{d}x'\,\mathrm{d}y', \tag{4.1}$$

where z is the distance between the sample and the detector [45]. In the case of a binary sample with an opaque background level as used in this experiment, if we let t_c be the constant transmission value for the feature area, then $t(x',y')$ can be written as $t(x',y') = |t(x',y')|\exp(i\phi_{t_c})$, where ϕ_A denotes the phase of a complex quantity A. Then Eq. (4.1) is equivalent to

$$U = \mathcal{F}[e^{i\frac{\pi}{\lambda z}(x'^2+y'^2)} e^{i\phi_{E_{i,\mathrm{Smp}}}(x',y')} u(x',y')], \tag{4.2}$$

where U is defined as $U = E_{t,\mathrm{Det}}(x,y)\{\frac{1}{i\lambda z}\exp[i\frac{2\pi}{\lambda}z + i\frac{\pi}{\lambda z}(x^2+y^2) + i\phi_{t_c}]\}^{-1}$, having an amplitude proportional to the measured $|E_{t,\mathrm{Det}}|$, $\mathcal{F}$ is the Fourier transform, and $u(x',y') = |E_{i,\mathrm{Smp}}(x',y')t(x',y')|$ is the quantity to be reconstructed. This equation provides the required transform that relates the detector plane to the sample plane. The precise characterization of the incident beam $E_{i,\mathrm{Smp}}$ is possible through techniques such as ptychography CDI [42]; in this paper, we use an approximation:

we consider only the quadratic phase (including astigmatism) while ignoring higher order phases, thus $E_{i,\mathrm{Det}} = |E_{i,\mathrm{Det}}| \exp[i\frac{\pi}{\lambda}(x^2/z_{\mathrm{df_x}} + y^2/z_{\mathrm{df_y}})]$, where $|E_{i,\mathrm{Det}}|$ is the measured amplitude of the beam (with the sample out of the beam path) on the detector, $z_{\mathrm{df_x}}$ is the distance between the detector and the x-focus, and $z_{\mathrm{df_y}}$ is the distance between the detector and the y-focus. We then back-propagated $E_{i,\mathrm{Det}}$ to the sample plane to obtain $E_{i,\mathrm{Smp}}$.

Reconstruction of u was conducted using a modified RAAR algorithm [66]. We started from an initial guess of random phase for the diffracted wave, and each iteration was composed of the following three steps:

(1) Calculate u using the inverse transform for Eq. (4.2):

$u = \exp[-i\frac{\pi}{\lambda z}(x'^2 + y'^2) - i\phi_{E_{i,\mathrm{Smp}}}(x', y')]\mathcal{F}^{-1}U$;

(2) Apply the support constraint provided by the finite illumination, and a constraint of the phase of u to be within $[-\pi/4, \pi/4]$ rad, which is equivalent to the non-negativity constraint [26];

(3) Calculate U using the transform defined in Eq. (4.2) and apply the modulus constraint.

The algorithm iterates until a suitably low error is achieved or more importantly, the derivative of the error reaches a constant value; usually below 100 iterations. After the algorithm converged, 100 iterations were averaged together to produce the object domain reconstructions, as shown in Figs. 4.2(d) and (f) for region I and II respectively. Based on Abbe Theory [67], the theoretical resolution achieved in this first demonstration is $0.82\lambda/\mathrm{NA} = 102$ nm, which can easily be improved in the future by use of a shorter wavelength illumination or by increasing the NA.

The original implementation of keyhole CDI [62] made use of a FZP with a smaller diameter than the incident beam to constrain the extent of the illumination on the sample. A central beam-stop is required in this case, in order to prevent any unfocused light from illuminating the sample. This results in an annular beam. In the implementation of keyhole CDI discussed here, the FZP is replaced by a curved EUV multilayer mirror, which is generally more efficient. A detailed

discussion of the efficiency of EUV zone plates can be found in [68]. An ideal (without fabrication imperfections, with no substrate that introduces extra absorption) FZP of alternately opaque and transmissive zones has a theoretical efficiency (diffracted into +1 order) of $1/\pi^2 \approx 10\%$; while for an ideal phase reversal zone plate, the theoretical efficiency is $4/\pi^2 \approx 41\%$. Due to absorption of materials for the EUV wavelength, it is not possible to build a genuine phase reversal zone plate with transparent phase-shifting zones. Based on the results and with materials that "seem suitable" from [68], for 28.7 nm as used in this paper, an ideal FZP made of aluminum, assuming no oxidation in addition, has a calculated efficiency of 28%; while for 13 nm (the wavelength used in EUV lithography), an ideal FZP made of beryllium has a calculated efficiency of 24%. The efficiency will be even less for implementation in keyhole CDI due to the use of the central beam-stop. In comparison, our 28.7nm EUV mirror has a measured efficiency of 47%, and the 13 nm EUV mirror has a measured efficiency of 66%. In addition to the improved efficiency, EUV-mirror-based keyhole CDI does not require a central beam-stop; therefore the sample is more uniformly illuminated. To our knowledge, these results represent the first demonstration of a general and efficient tabletop coherent EUV microscope that can image extended (i.e. non-isolated) samples, as well as the first demonstration of keyhole CDI using a tabletop EUV source.

4.3 Keyhole CDI for semi-transparent samples

Next we performed EUV-mirror-based keyhole CDI on a sample with a semi-transparent background (Fig. 4.3). The HHG source and EUV mirrors were similar to those used in the previous measurements but with some improvements, such as the use of a higher laser repetition-rate of 5 kHz, and a larger, 200-μm-diameter waveguide. These improvements resulted in an enhancement of the HHG flux from $\approx 10^9$ to $\approx 10^{10}$ photons per second in a single harmonic at the exit of the waveguide. For the sample used in this section, which has less scattering efficiency than the previous sample, these improvements decrease the required exposure times for this experiment from about 2 hours to 14 minutes.

The second sample consists of 30 nm chromium deposited on a 45-nm-thick Si_3N_4 membrane.

The patterned features, etched in the Cr/Si_3N_4 sample by use of focused ion beam, are shown in the inset SEM image of Fig. 4.3(a). Unlike the first sample, this sample was $\approx 8.5\%$ transparent. As a result, the diffraction pattern contains a large amount of un-scattered light.

As discussed above, the non-normal incidence of the EUV beam on the curved mirror introduced astigmatism, with a separation between horizontal and vertical foci of 1.5 mm in this case. To implement keyhole CDI, a 200-μm-diameter pinhole aperture was placed in the beam 16 mm upstream of the circle of least confusion. Due to the transparent nature of this sample, the scattered light from the aperture was of similar amplitude to that from the sample and had to be removed. To accomplish this, a second 50 μm diameter pinhole aperture was placed between the first aperture and the sample to spatially filter most of the unwanted scattered light from the hard edge of the first pinhole (see the sketch of the experimental setup in Fig. 4.3(a)). This second aperture was placed 1.4 mm upstream of the circle of least confusion. As shown in Figs. 4.3(b) and 4.3(c), the second aperture removed the majority of the unwanted light scattered from the first aperture. The sample as positioned at the circle of least confusion, where the illumination spot size was 8 μm in diameter. The detector was placed 5.71 cm away from the sample. The measured diffraction patterns of the sample and the beam are shown in Fig. 4.3(d) and its inset, respectively, corresponding to an NA = 0.20, leading to a theoretical resolution of $0.82\lambda/\mathrm{NA} = 118$ nm.

In this experiment, the thickness of the sample($\approx$ 75 nm) is much less than $D/\mathrm{NA} = 40$ μm, so Eq. (2.4) is again valid. We write the total complex transmission function as: $t(x', y') = t_0(x', y') + \Delta t(x', y')$, where $t_0(x', y')$ is the transmission coefficient of the background unpatterned Cr/Si_3N_4 layers of the sample ($\approx$ 0.29), and $\Delta t(x', y')$ is the modification to the transmission of the sample due to the etched features. This reconstruction approach is similar to that used in Fresnel CDI [63]. We write $U = \mathcal{F}\{\exp[i\frac{\pi}{\lambda z}(x'^2 + y'^2)]E_{i,\mathrm{Smp}}(1 + \frac{\Delta t(x',y')}{t_0(x',y')})\}$ where U has a magnitude proportional to the measured magnitude of the electric field at the detector, and $\Delta t/t_0$ is the quantity to be reconstructed in the iterative algorithm. We first calculated the incident field $E_{i,\mathrm{Smp}}$ using the same approach explained in [69], with the sagittal and tangential slices through the propagated beam shown in Figs. 4.4(a) and 4.4(b). The quantity $\Delta t/t_0$ is non-zero only in the

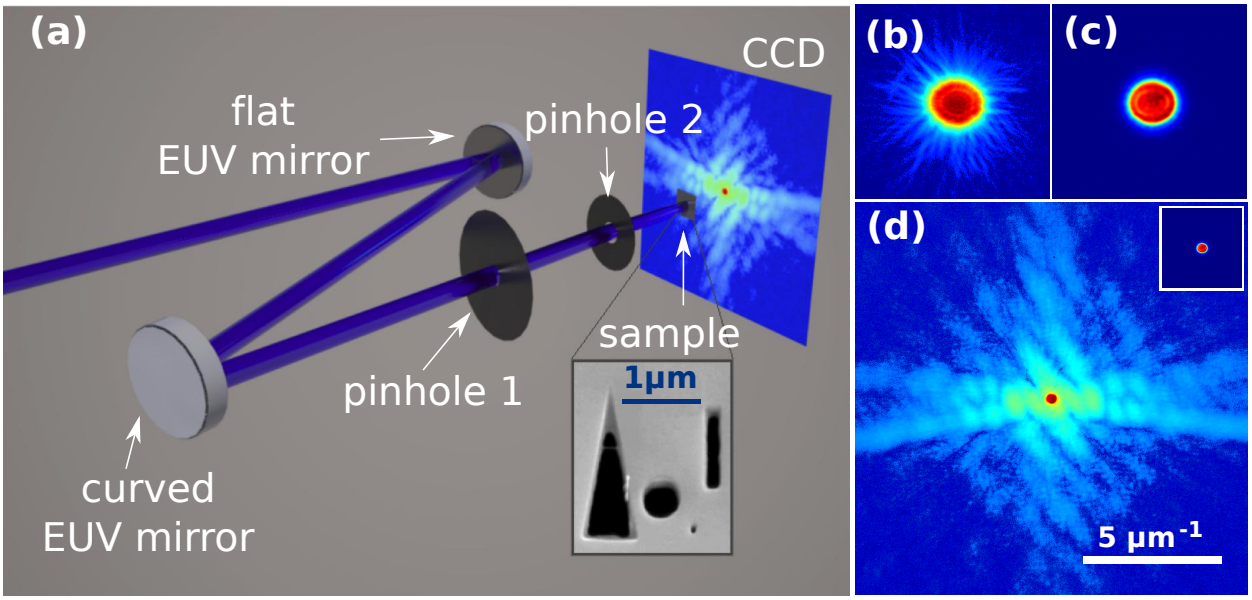

Figure 4.3: Tabletop EUV keyhole CDI of a sample with a semi-transparent background. (a) Schematic of the setup. A second pinhole is inserted into the beam to remove scatter light form the first pinhole. The inset shows an SEM image of the sample, composed of a 30 nm Cr film deposited on top of a 45-nm-thick Si_3N_4 membrane. (b) and (c) A zoomed view of the beam on the CCD before and after inserting the second pinhole. (d) Diffraction pattern (cropped and centered) from the sample shown to the 1/4 power. The inset shows the diffraction pattern of the beam when the sample is removed. Figure reproduced from Zhang *et al.* [27].

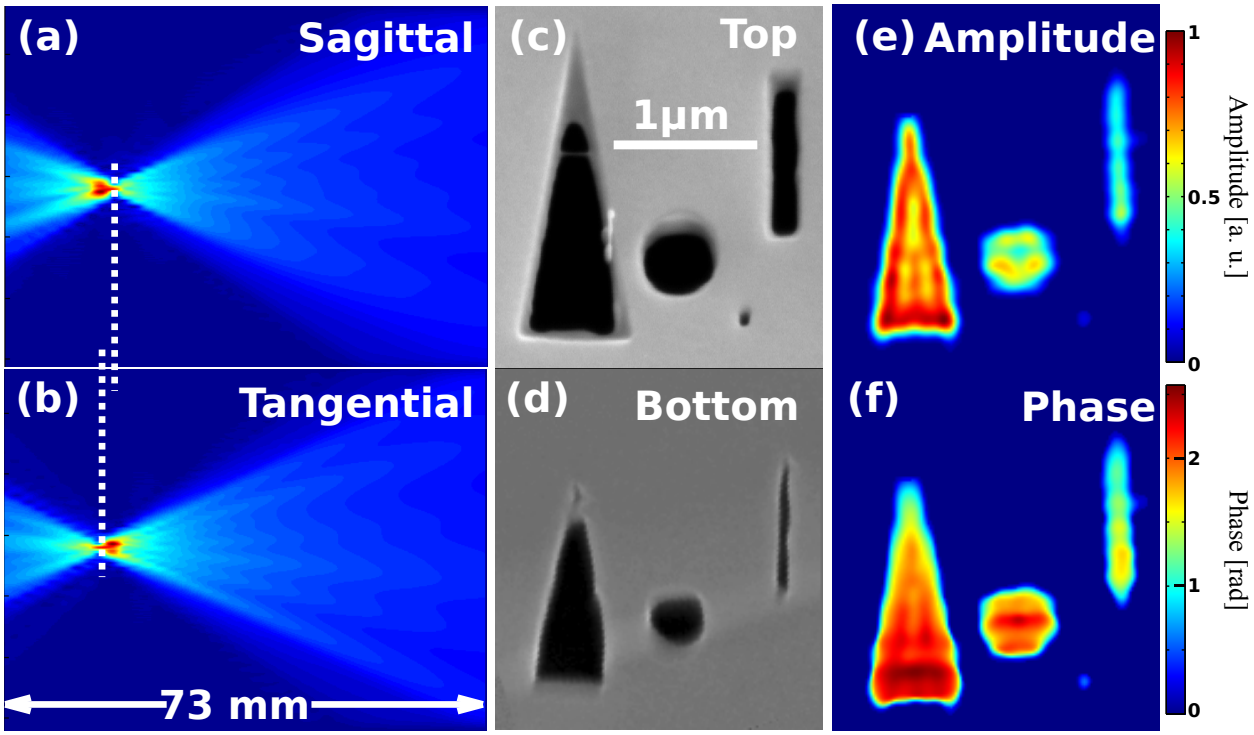

Figure 4.4: Image reconstruction results for a sample that has a semi-transparent background

Image reconstruction results for a sample that has a semi-transparent background. (a),(b) Sagittal and tangential slices through the focusing EUV beam. The dashed lines show the positions of the two foci. (c) SEM image of the top side of the sample (geometrically scaled to account for a 52° tilt of the sample plane). (d) SEM image of the bottom side of the sample. Only the darkest parts on the sample are completely etched through. (e), (f) Reconstructed amplitude (normalized to unity at maximum with arbitrary units) $|\frac{\Delta t}{t_0}|$ and phase $\phi_t(x', y')$ of the sample. (d) (e) (f) have the same scale bar as (c). Figure reproduced from Zhang *et al.* [27].

feature areas, allowing us to use the shrink-wrap dynamic support constraint [55]. An additional constraint on the phase of $\Delta t/t_0$ to be within $[\phi_0 - \Delta\phi/2, \phi_0 + \Delta\phi/2]$, where $\phi_0 = 2.0$ rad and $\Delta\phi = \pi/2$ rad were determined empirically, was found to significantly speed up the convergence of the iterative reconstruction. The magnitude of t_0 was determined from the ratio of the beam intensity on the CCD with the sample's Cr/Si_3N_4 layers in the beam and that of the sample out of the way. Starting with an initial guess of random phase on the detector, we typically used 20 to 100 iterations of the RAAR algorithm [57] followed by 10 iterations of the error reduction algorithm [25] to retrieve the sample diffraction phase on the detector. We averaged over 10 independent reconstructions, and the amplitude (normalized) $|\frac{\Delta t}{t_0}|$ and phase $\phi_t(x', y')$ (the phase of the background is chosen as the zero-phase reference) are shown in Figs. 4.4(e) and 4.4(f). They are in very good agreement with the SEM images shown in Figs. 4.4(c) (top) and 4.4(d) (bottom). Moreover, it was also possible to reconstruct the image of the small 50-nm-diameter hole, seen in the topside SEM image Fig. 4.4(c).

The ESW can be written as $E_t = E_i(t_0 + \Delta t)$. We see that a non-zero transmission factor t_0 produces a reference wave while Δt produces an object wave for the in-line holography geometry [5, 62]. Thus, for the sample used in this experiment, the diffraction pattern in Fig. 4.3(d) is in actuality an in-line hologram. However, since there is only a small area on the CCD where the reference wave has significant intensity to produce interference with the scattered wave from the sample, the image from a conventional in-line holographic reconstruction [5, 70] would not have as high resolution as CDI. Moreover, in-line holographic reconstructions also suffer from twin-image artifacts [71]. Using the known reference wave, CDI can be used to extract phase information about the object. Furthermore, with this extracted phase information, and the value(s) of index of refraction for the material, we can obtain thickness or depth information.

A reference topography measurement of the sample is shown in Fig. 4.5(a) by use of a Digital Instruments Dimension 3100 atomic force microscope (AFM), with a probe tip size of 3 nm and a scan step size of 16 nm. For comparison, we then calculate the depth map from the keyhole CDI reconstruction. For the sample used in this experiment, if we define the top plane (completely

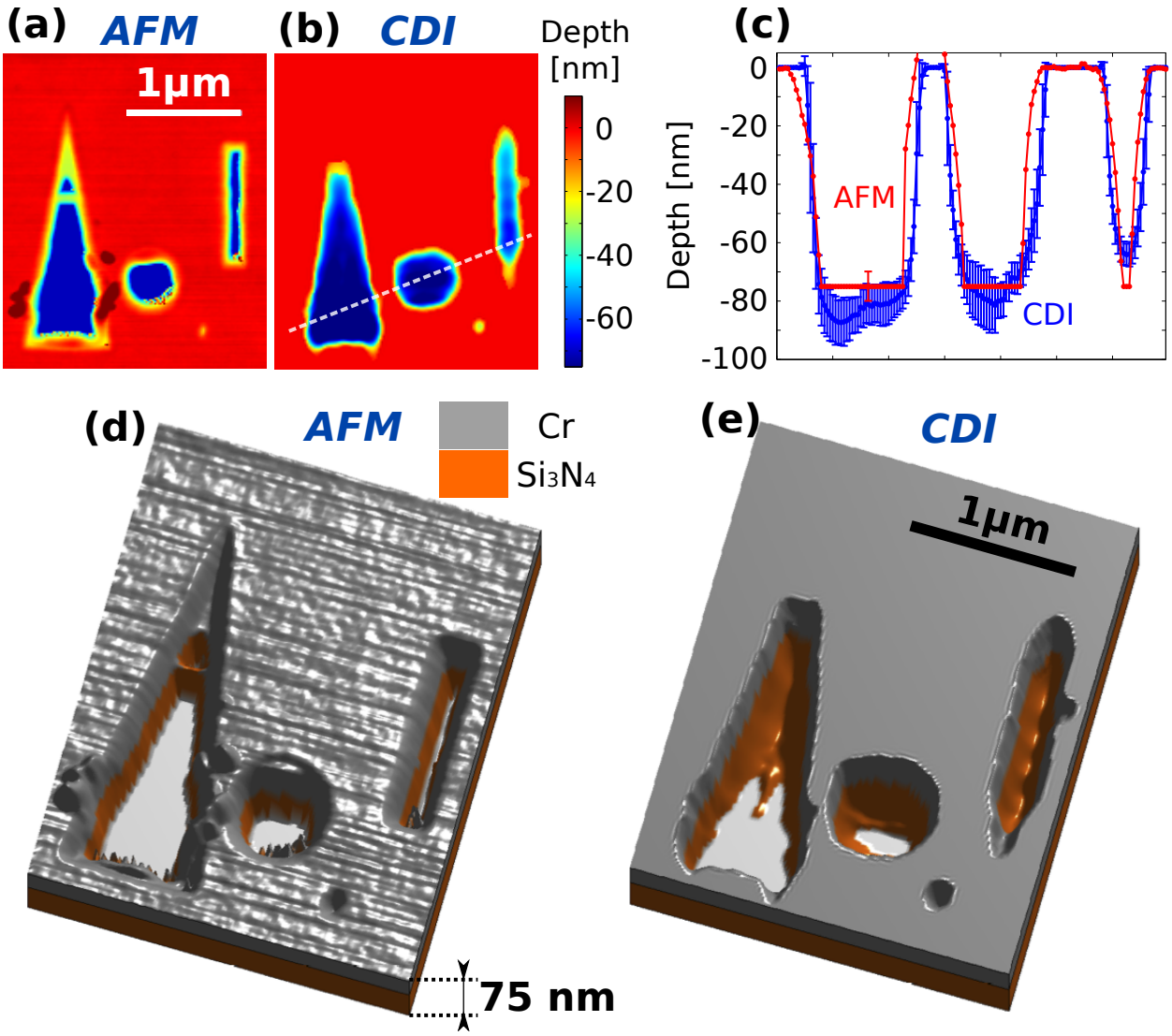

Figure 4.5: Height comparison between AFM and keyhole CDI. (a), (b) Depth maps of the sample using AFM and keyhole CDI respectively. (c) Comparison of lineouts along the dashed line in (b) with associated error bars. (d) and (e) 3D profiles of the sample based on the depth values in (a) and (b). The top 30 nm Cr layer and bottom 45 nm Si_3N_4 layer are shown in different colors. Figure reproduced from Zhang *et al.* [27].

unetched) as the zero depth level, and write the index of refraction for EUV as $n = 1 - \delta + i\beta$, then the phase of t as a function of the depth d (≤ 0) can be written as

$$\phi_t(d) = \begin{cases} -\frac{2\pi}{\lambda}\delta_{\mathrm{Cr}} \cdot d & \text{for} \quad -h_{\mathrm{Cr}} \leq d \leq 0, \\ -\frac{2\pi}{\lambda}[\delta_{\mathrm{Cr}} \cdot (-h_{\mathrm{Cr}}) + \delta_{\mathrm{Si_3N_4}} \cdot (d + h_{\mathrm{Cr}})] & \text{for} \quad d \leq -h_{\mathrm{Cr}}, \end{cases} \tag{4.3}$$

where h_{Cr} is the thickness of the top Cr layer. The deposited Cr film has a density of 6.55 g/cm^3 (8.9% less than the bulk Cr density 7.19 g/cm^3), determined from an X-ray reflectivity measurement. By use of the known δ_{Cr} and $\delta_{\mathrm{Si_3N_4}}$ values at the illuminating wavelength [72], as well as $h_{\mathrm{Cr}} = 30$ nm, we calculated the depth map of the sample from the reconstructed phase ϕ_t with Eq. (4.3). To determine the uncertainty of our quantitative analysis, we considered the major error sources. First, the ± 50 μm uncertainty in determining the positions of the two astigmatic foci results in an error in the calculated phase of the incident beam and thus the reconstructed sample phase and thickness. Second, the uncertainty in the wavelength (28.7 ± 0.7 nm due to the bandwidth of the multilayer mirrors) causes uncertainty in the values of index of refraction, leading to error in the thickness calculation. Third, the imperfect repeatability of reconstructions leads to small fluctuations in the calculations. We scanned the focus positions and the wavelength in their uncertainty range, and for each parameter set, we performed 10 independent reconstructions; from all reconstructions, we found the maximum and minimum depth at each position, with the mean values shown in Fig. 4.5(b). An AFM is a surface measurement device, meaning that those portions of the sample that are completely etched through will result in an artificially deep measurement. We find, using -75 nm as the lower threshold, that the AFM image gives the same shape in the completely etched regions as the SEM image of the bottom side of the sample, as shown in Fig. 4.4(d). These images confirm that the 50 nm wide hole and the edges of the larger features are not fully etched through. Fig. 4.5(c) compares the depth profiles along the dashed lines in Fig. 4.5(b) between keyhole CDI and AFM. The error bars plotted in Fig. 4.5(c) indicate the maximum and minimum depth values found within the range of uncertainty. We see good quantitative agreement between the AFM and tabletop EUV keyhole CDI images. The depth of the 50 nm wide hole is

20 ± 5 nm as measured by AFM, and 28 ± 9 nm from keyhole CDI. The AFM uncertainty of ± 5 nm is determined from a two-dimensional grating calibration standard with a 180 nm step height, and is given for a 95% confidence level.

Keyhole CDI illuminated by EUV high harmonics has several advantages in comparison with AFM. First, the depth profile from the entire FOV can be measured simultaneously so that point-by-point scanning is unnecessary. Thus, there is the potential for much higher data acquisition speeds, limited only by the illumination flux. Second, AFM images can be influenced by nonlinearity, hysteresis, creep of the piezoelectric material, and cross-talk between the x, y, and z axes. In practice, software enhancement and filtering are used to improve AFM image quality, but this post-processing can also flatten out real topographical features. Keyhole CDI has no such problems. Third, keyhole CDI allows a long working distance and no contact with the sample, thus avoiding potential sample damage. A limitation of our current technique is that it is only applicable to relatively thin samples; the sample should be thin enough so that the light can penetrate, and much thinner than D/NA as mentioned before. However, this limitation can be overcome in the future by extending tabletop keyhole CDI to reflection mode [59].

4.4 Conclusion

Using a new approach to keyhole coherent diffractive imaging, we have demonstrated a tabletop EUV microscope that can image extended, non-isolated, aperiodic samples for the first time. We achieve increased efficiency of the imaging system and a more uniform illumination at the sample when compared with previously reported methods based on Fresnel zone plates. Quantitative depth information about the object can also be retrieved, in very good agreement with AFM measurements and with significant added benefits such as non-contact, non-destructive measurement capabilities. In the future, when combined with advances in bright HHG sources with < 1 nm wavelength [18], this approach can be used to image nanoscale dynamics, including ultrafast spin, heat, strain and current flow [73–75] with combined few femtosecond time resolution and sub-10 nm spatial resolution, in thick samples, with elemental and chemical sensitivity.

Chapter 5

First Demonstration of General Reflection CDI

This chapter describes the work on extending the CDI technique form transmission geometry to reflection geometry. Although it seems straightforward for this extension, the truth is that only very limited successes had been achieved for reflection CDI. Previous work was either limited to highly reflective EUV lithography masks in a normal incidence geometry [76], restricted to low numerical aperture through the use of a transmissive mask [77], or restricted to isolated objects [78, 79].

5.1 Initial attempts

5.1.1 Apertured illumination CDI in reflection

Thw sample isolation requrement can be harder for reflection geometry: most of the materials do not have zero reflectivity, although they can have close to zero transmissivity as long as they are thick enough. So techniques that allow for imaging non-isolated objects are needed. We first tried the apertured illumination CDI approach.

We modified the transmission mode setup of apertured-illumination CDI so that the sample is at an angle $\alpha = 30$ degrees (Fig. 5.2(a)). The same detector and Fourier transform lens were used as in the transmission setup, but were repositioned such that they were aligned along the specular reflection from the sample (Fig. 5.2(a)). Thus the NA was kept at 0.22 and the resolution at 1.4 μm. The sample used was a positive 1951 USAF Resolution Target. Figure 5.1(a) shows a scatter pattern form the vertical bars of group 5 (element 1) of the resolution target. The black

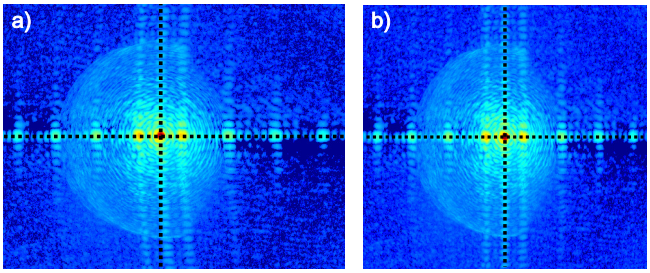

Figure 5.1: Mapping the diffraction from a tilted sample to a diffraction pattern linear in frequency space. (a) The raw data from light scattered by the sample at an angle of 30 degrees. (b) The data mapped onto a linear grid in frequency space. The dotted black lines are added to highlight the curvature seen in the tilted sample diffraction shown in (a). Both images have been scaled by the fourth root. Figure reproduced from Gardner *et al.* [59].

dashed lines are overlaid to illustrate the curvature in the diffraction resulting from a tilted sample. In Fig. 5.1(b) we show the scatter pattern after mapping the diffraction onto a grid that is linear in spatial frequency. After interpolation, the scatter pattern is proportional to the modulus of Fourier transform of the sample. Using the same iterative phase retrieval algorithm as mentioned in the previous section, we are able to reconstruct any arbitrary position of the target. These reconstructions are overlaid and shown in Fig. 5.2(b). An objective based bright-field microscopy image is also shown in Fig. 5.2(c) for comparison.

5.1.2 Imaging periodic samples in reflection

For a periodic sample, if an averaged image of a unit cell, instead of an image of every unit cell in the illumination area, is the goal, then the isolation requirement would mean for each unit cell, the feature area is less than 50%. So here we used a periodic sample to avoid the sample isolation requirement for initial attempts. This allows us to decouple the difficulties of satisfying isolation requirement and applying CDI to a reflection geometry.

The sample was a two-dimensional array of identical square, nickel nano-pillars, each $\sim 2\mu$m in width and 20nm high, patterned on a sapphire substrate. Rather than using AICDI, a slightly simpler geometry was used where the beam was loosely focused directly onto the object, with a spot size of approximately 25 μm, so that many pillars were illuminated (Fig. 5.3(a)). The incident

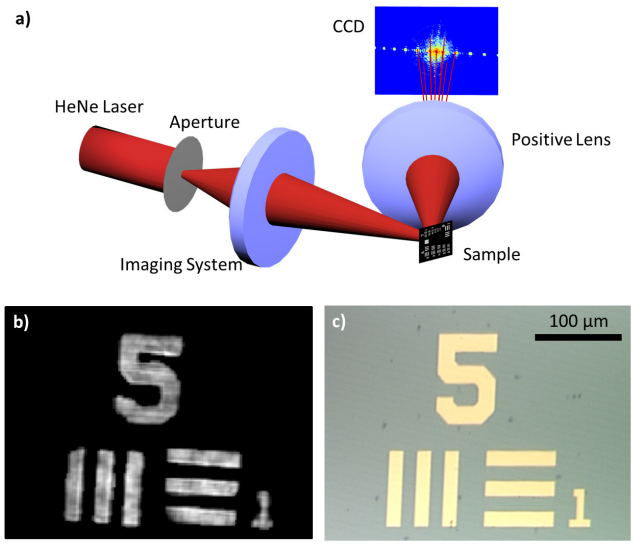

Figure 5.2: Visible laser apertured illumination and tilted sample correction by reconstructing a 1951 USAF resolution target in a reflection mode geometry. (a) A schematic of the setup. Note that a negative USAF pattern is shown, but a positive USAF was used in the experiment. (b) Several reconstructions with different scan positions are overlaid to show the AICDI reconstruction. (c) A traditional bright-field microscopy image of the sample. Figure reproduced from Gardner *et al.* [59].

angle of the HHG beam on the sample was 45 deg, and as a result the scatter pattern in Fig. 5.3(b) displays a high degree of asymmetry, making this specimen a good demonstration of the need for tilted plane correction. Figures 5.3(b) and 5.3(c) show uncorrected and corrected scatter patterns respectively. The 27.6 mm square detector with 13.5 μm pixels (Andor iKon) was placed 4.5 cm past the object, resulting in a NA of 0.29. An integration time of 20 minutes was required in order to obtain the diffraction pattern in Fig. 5.3(b). The missing center in the diffraction pattern is the result of a beam stop used to prevent saturation of the bright zero order peak. The beam stop was placed as close to the detector as possible ($\approx 2mm$) in order to minimize edge diffraction effects.

This specimen can be thought of as a convolution between a Dirac comb function with a single nickel nano-pillar of 1/4 duty cycle. With this in mind, and using the convolution theorem, we can consider the Fourier transform of this sample to be the product of the individual Fourier transforms of the Dirac comb and a single (averaged) nano pillar. This means that in the diffraction plane, a Dirac comb samples a sinc function, which is the Fourier transform of a single pillar. Using this idea we can increase the signal-to-noise ratio, after applying the tilted plane correction, by extracting the peak values (spaced by the period of the Dirac comb) of the scatter pattern and placing them on a new, coarser grid, shown in Fig. 5.3(d). This new grid was used in the averaged pillar reconstruction shown in Fig. 5.3(e), producing an image with ~ 100 nm theoretical resolution. The reconstructions were carried out in the same manner and with the same algorithm as in the case of the 632.8 nm illumination. Clearly this method of resampling the data onto a separate grid by extracting the peaks in the diffraction plane is only applicable for arrays of identical objects. However, provided a contrast mechanism exists, the same apertured illumination technique discussed above can be implemented more generally for full field imaging of nanostructures in the EUV.

5.2 First demonstration of a general purpose ptychography reflection microscope

After initial attempts of reflection CDI with apertured illumination CDI technique and with a periodic sample described in the previous section, this section describes our work using pty-

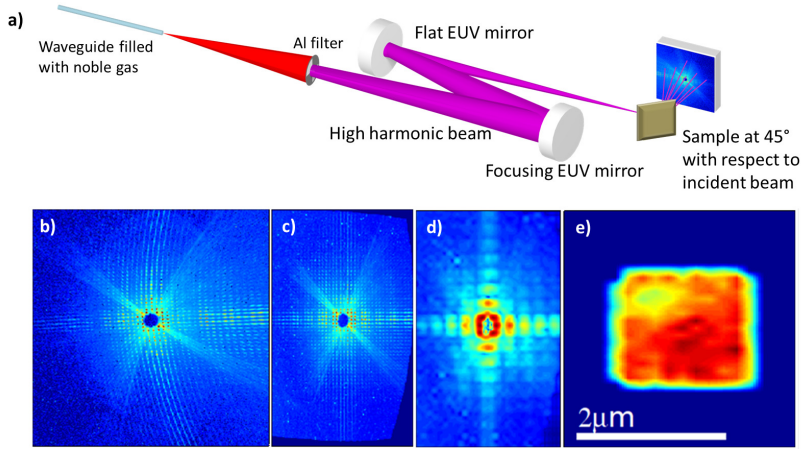

Figure 5.3: EUV microscope image in reflection mode of a 2D array of nickel nano-pillars.(a) A schematic of the setup. Uncorrected (b) and corrected (c) diffraction patterns. The data in (c) was resampled onto a coarser grid, shown in (d), containing only the peak intensity points. (e) Reconstructed image using the diffraction pattern in (d). The missing data shown in (b), (c) and (d) was left as a free parameter and is a result of a beam stop used to prevent saturation of the bright zero order peak on the camera. Figure reproduced from Gardner *et al.* [59].

chography CDI with a non-periodic sample for reflection CDI. We demonstrate the most general reflection-mode coherent diffractive imaging to date using any light source, by combining the ePIE algorithm [56] with curved wavefront illumination [80]. This allows extended (non-isolated) objects to be imaged at any angle, which will enable tomographic imaging of surfaces. This work also represents the first non-isolated-object, high fidelity, tabletop coherent reflection imaging, which expands the scope of applications for CDI significantly. This work demonstrates a powerful new capability that can impact a very broad range of science and technology. First, our approach removes restrictions on the numerical aperture, sample, or angle, so that general extended objects can be imaged in reflection mode at any angle of incidence. Second, illumination of the sample with a strongly curved wavefront removes the need for a zero-order beam-stop by reducing the dynamic range of the diffraction patterns. The curved illumination also allows the size of the beam to vary according to the sample size, alleviating the need for a large number of scan positions. This also results in fewer necessary scan positions when imaging a large field of view. Third, reflection ptychography produces surface images containing quantitative amplitude and phase information about the sample that are in excellent agreement with AFM and SEM images, and also removes all negative effects of non-uniform illumination of the sample or imperfect knowledge of the sample position as it is scanned [81]. The result is a general and extensible imaging technique that can provide a comprehensive and definitive characterization of how light at any wavelength scatters from an object, with resolution limited only by the wavelength and the numerical aperture of the system. This complete amplitude and phase characterization thus is fully capable of pushing full field optical imaging to its fundamental limit. Finally, because we use a tabletop high harmonic generation (HHG) 30 nm source [18], in the future it will be possible to image energy, charge and spin transport with nm spatial and fs temporal resolution on nanostructured surfaces or buried interfaces, which is a grand challenge in nanoscience and nanotechnology [74, 82].

5.2.1 Sample fabrication

The sample used in the experiment was fabricated on a super-polished silicon wafer. The wafer was rinsed with acetone, isopropanol, and methanol, and baked on a hotplate for 20 minutes at 250° C. It was then spin-coated with Microchem 2% PMMA in anisole, molecular weight 950 at 4000 r.p.m. for 45 seconds. Afterwards it was baked at 180° C for 90 seconds. Electron beam lithography was performed using a FEI Nova NanoSEM 640, using Nanometer Pattern Generation System (NPGS) software and patterns. The resist was then developed by immersion in a 1:3 solution of methyl-isobutyl-ketone:isopropanol for 30 seconds. Approximately 30 nm of titanium was evaporated onto the surface using a CVC SC3000 3-boat thermal evaporator. The lift-off step was accomplished in acetone using a sonicator.

5.2.2 Experiment

The experimental geometry for reflection mode Fresnel ptychography is shown in Fig. 5.4. A Ti:sapphire laser beam with wavelength ≈785 nm (1.5 mJ pulse energy, 22 fs pulse duration, 5 kHz repetition rate) is coupled into a 5 cm-long, 200 μm inner diameter, hollow waveguide filled with 60 torr of argon. Bright harmonics of the fundamental laser are produced near a center wavelength of 29 nm (27th harmonic) since the high harmonic generation process is well phase-matched [19], ensuring strong coherent signal growth and high spatial coherence. The residual fundamental laser light, which is collinear with the high harmonic beam, is filtered out using a combination of two silicon mirrors (placed near Brewster's angle for 785 nm light) and two 200 nm-thick aluminum filters. The EUV beam is then sent through an adjustable ≈1 mm aperture, placed ≈1 m upstream of the sample, to remove any stray light outside the beam radius. A pair of Mg/SiC multilayer mirrors then select the 27th harmonic of the Ti:sapphire laser at 29.5 nm. The first mirror is flat, while the second mirror has a radius of curvature of 10 cm. This mirror pair focuses the HHG beam onto the sample at an angle of incidence of 45°. The focus position is 300 μm downstream of the sample, so that the HHG beam wavefront at the sample plane has significant curvature. The

angle of incidence on the curved mirror is approximately 2°, which introduces small amounts of astigmatism and coma onto the HHG beam.

The sample consisted of ≈30 nm-thick titanium patterned on a silicon substrate using e-beam lithography. A scanning electron microscope (SEM) image of this object is shown in Fig. 5.5b. The scattered light from the object is measured using an EUV-sensitive CCD detector (Andor iKon, 2048×2048, 13.5 μm square pixels), placed 67 mm from the object, and oriented so that the detector surface was normal to the specular reflection of the beam. The sample was positioned 300 μm before the circle of least confusion along the beam axis, so that the beam diameter incident on the sample was approximately 10 μm. Diffraction patterns were measured at each position of 10 adjacent 3×3 grids, with 2.5 μm step size between positions. The positions were randomized by up to 1 μm in order to prevent periodic artifacts from occurring in the ptychographic reconstruction [83].

5.2.3 Image reconstruction

The process for obtaining the reconstruction was as follows:

(1) Tilted plane correction was applied to each of the 90 diffraction patterns in the full dataset.

(2) The standard ePIE algorithm [56] was applied to the corrected data, with subpixel scan position precision handled as in Maiden *et al.* [84]. A starting guess for the probe was calculated using knowledge of the sample-to-focus distance (300 μm). The object starting guess was set to unity and the probe guess was normalized to contain the same energy as the average diffraction pattern in the dataset. The algorithm was allowed to update the probe guess in parallel with the object guess at each sub-iteration. The algorithm was run in this way for 20 full ptychographic iterations, at which point the probe guess had made much more progress towards convergence than the object guess. The object guess was reinitialized to unity, and the algorithm was restarted using the new probe guess, and allowed to run for 100 iterations, long enough for both the object and probe to converge to stable solutions.

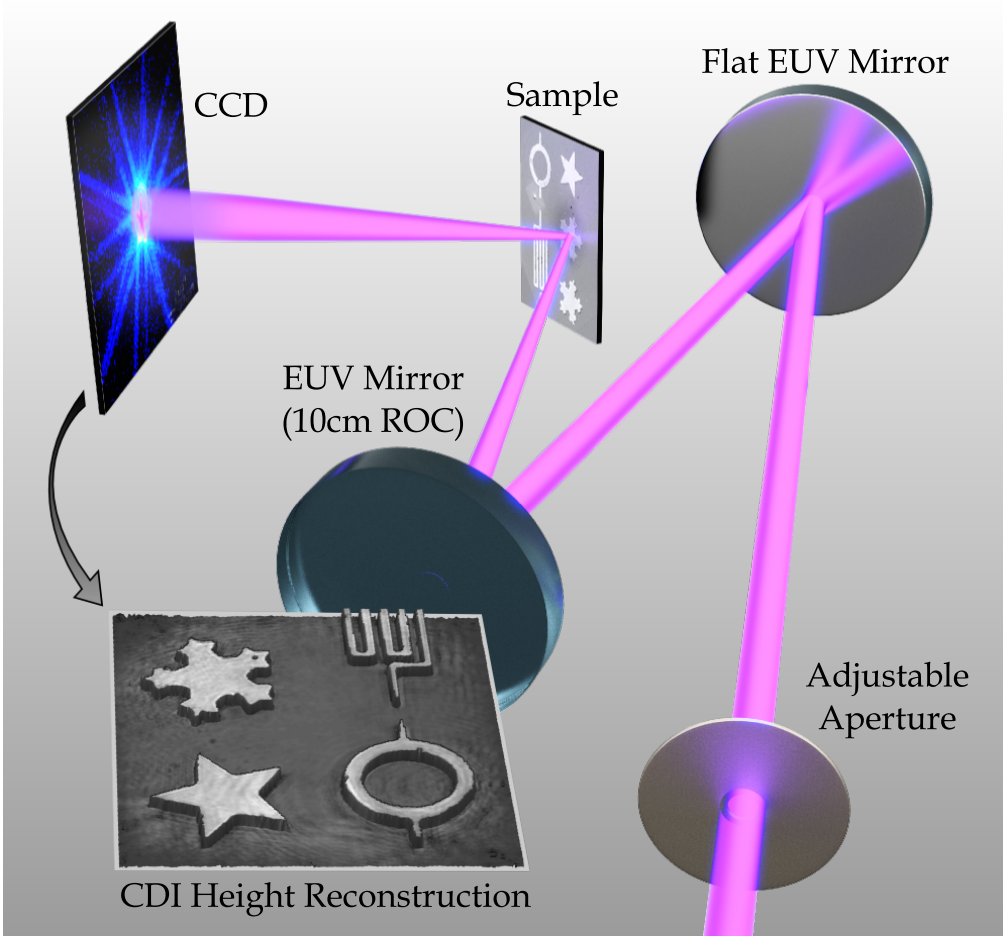

Figure 5.4: Experimental setup for reflection mode Fresnel ptychography. The EUV beam propagates through an adjustable ≈1 mm aperture, and a single harmonic is selected using a pair of multilayer mirrors centered at 29.5 nm, and focused onto the sample. The scattered light is collected on a CCD detector placed directly after the sample. The inset shows a height profile reconstructed through ptychography. Figure reproduced from Seaberg *et al.* [44].

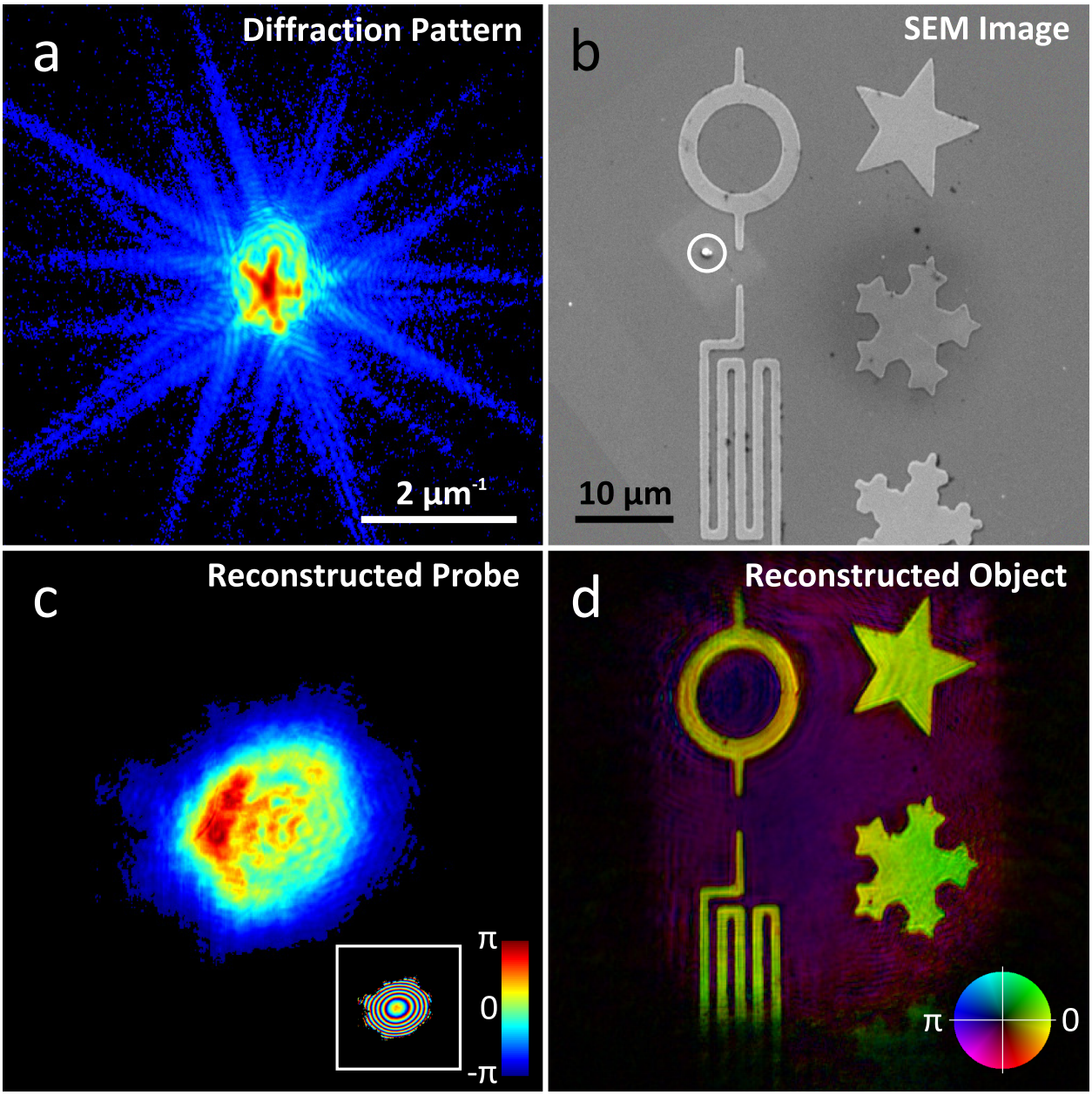

Figure 5.5: Diffraction data and ptychographic reconstruction. (a) Representative diffraction pattern, scaled to the $\frac{1}{4}$ power, taken from the 90-scan dataset. (b) SEM image of the Ti patterned Si sample. Note that the large defect circled in the SEM image resulted from contamination after the ptychography measurement. (c) Reconstructed amplitude (thresholded at 5%) of the HHG beam. The inset shows the reconstructed phase (displayed modulo-2π). (d) Ptychographic reconstruction of the object shown in (b). The reconstruction is plotted as the complex amplitude, where brightness represents reflected amplitude and hue represents the phase of the reconstruction. Note that the majority of defects seen in the SEM image of the Ti nanostructures are reproduced in the ptychographic reconstruction. The scale bar in (b) is shared among (b)-(d). Figure reproduced from Seaberg *et al.* [44].

(3) The object guess was re-initialized as described in step 2, and the probe guess was set to that found at the end of step 2. The subpixel position correction method [81] was applied to the ePIE algorithm, and the overlap constraint was applied with subpixel shifts of the probe [84]. The position correction feedback parameter β was started at a value of 50, and automated as in Zhang *et al.* [81]. The probe guess was not allowed to update during this step. Again, the algorithm was run for 100 iterations, until the position corrections converged to < 0.1 pixel.

(4) Finally, using the probe found in step 2 and the corrected scan positions found in step 3, and with the object guess reinitialized to unity, the algorithm was run for 200 iterations to achieve the final reconstruction.

Each full iteration (cycling through all 90 diffraction patterns) took approximately 30 seconds on a personal computer, leading to a total reconstruction time of 3.5 hours.

5.2.4 Oxide layer measurement

The thickness of the oxide layer on the Si wafer used for sample fabrication was determined through ellipsometry (Gaertner Scientific L117F300). The measurements were made at 70° angle of incidence using a He-Ne laser at 632.8 nm. The ellipsometric angles ψ and Δ were determined to be 10.20(0.04)° and 171.00(0.07)°, respectively. The angles are defined as

$$\frac{r_p}{r_s} = \tan\psi \; \mathrm{e}^{-i\Delta} \tag{5.1}$$

where r_p and r_s are the complex reflectivity coefficients for p- and s-polarized light, respectively. The thickness of the oxide layer was calculated by numerically solving the argument of Eq. (5.1), assuming an index of refraction for the oxide layer of 1.474(0.003) and an index of refraction for the silicon substrate of $3.89(0.02) + i\,0.011(0.009)$ at 632.8 nm wavelength. The result, was an oxide layer thickness of 3.0(0.1) nm.

5.2.5 Results and discussion

Due to the non-normal angle-of-incidence on the sample, the patterns must be remapped onto a grid that is linear in spatial frequencies of the sample plane, in order to use fast Fourier transforms (FFTs) in the data analysis. We used tilted plane correction to accomplish this [59]. An example of a corrected diffraction pattern is shown in Fig. 5.5a. The diffraction patterns were cropped such that the effective numerical aperture was 0.1, enabling a half-pitch resolution of 150 nm. The image was reconstructed using the ePIE, along with the sub-pixel position determination method [81, 84]. A starting guess for the probe was calculated based on the estimated distance of the sample from the focus. The reconstructed complex amplitude of the object is shown in Fig. 5.5d. During the course of the reconstruction, the algorithm was used to further solve for the complex amplitude of the probe as well, resulting in the illumination shown in Fig. 5.5c. The reconstructed probe is completely consistent with a measurement of the unscattered beam at the detector. The high fidelity of the CDI reconstruction is evident by the fact that the majority of small defects visible in the SEM image of the Ti patterns (Fig. 5.5b) are also clearly visible in the CDI reconstruction (Fig. 5.5d). Note that the large defect circled in the SEM image in Fig. 5.5b was the result of sample contamination after the ptychography measurement.

Ptychography solves for the complex amplitudes of both the object and the probe (or incident beam) simultaneously [56, 83]. As a result, reliable quantitative information about the object can be obtained from the reconstruction, since the effect of the probe on the diffraction patterns is essentially divided out. Quantitative surface relief information can be obtained from the phase of the reconstructed object as well. The titanium was patterned at a thickness of approximately 30 nm. The round trip path difference of the reflected light is $-2h\cos\theta$, where h is the height above a reference (such as the substrate) and θ is the angle of incidence. At 45° angle of incidence for a feature thickness of 30 nm, the round trip path length difference between the silicon substrate and the patterned titanium features is 42.4 nm. At 29.5 nm wavelength, this corresponds to between 1 and 2 wavelengths path length difference. Additionally, the phase change upon reflection can be

highly variable for absorbing materials. In the case of this sample, both silicon and titanium have native oxide layers which must be taken into account when calculating this phase change. Thus, some prior knowledge is required in order to retrieve the absolute height of the features. The method for calculating the phase change upon reflection from a thin-film system with complex indices of refraction is described in Born and Wolf [67]. The indices of refraction at 29.5 nm wavelength necessary for this calculation were obtained from the Center for X-Ray Optics (CXRO) [72]. The thickness of the silicon oxide layer was measured using ellipsometry to be 3.0(0.1) nm, and the thickness of the titanium oxide layer was assumed to be 2.9(0.2) nm based on the literature [85,86]. For the SiO_2/Si region, the phase change δ_{Si} was calculated to be $-1.22(.03)$ radians and the theoretical reflectivity was calculated to be 0.33%. For the TiO_2/Ti patterns, the phase change δ_{Ti} was calculated to be $-1.92(0.09)$ radians and the theoretical reflectivity was calculated to be 10.9%. The object reconstruction shows a ratio of $\approx$17 between the reflectivity of the titanium and the silicon surfaces based on a histogram of the reconstructed amplitude, in reasonably good agreement with the calculated values, which assumed no surface roughness.

A flattening method was applied to the reconstructed phase of the silicon substrate, similar to that used in atomic force microscopy, due to some residual phase curvature reconstructed on the flat substrate. The peak-to-valley height variation of the subtracted surface fit was < 4 nm over the full $35 \times 40 \mu\mathrm{m}^2$ field of view. After flattening, the reconstruction shows an average of 4.26 radians of phase difference between the titanium and silicon surfaces, corresponding to a 46.2(0.7) nm path length difference (when 2π is added and after taking the phase changes upon reflection into account). This corresponds to a 32.7(0.5) nm average thickness of the titanium patterns. A height map of the sample could then be produced by assuming that 2π should be added to any part of the reconstruction that exhibited an amplitude above 25% of the maximum (based on the relative reflectivities of titanium and silicon, as discussed above). Additionally, the reflection phases δ_{Si} and δ_{Ti} were subtracted from the Si and Ti regions using the same criteria. The result of this analysis is displayed in Fig. 5.6a, and represents a significant improvement in image quality compared with all tabletop coherent reflective imaging to date. After the ptychography measurements were taken, an

independent height map of the sample was obtained using a Digital Instruments Dimension 3100 AFM. The resulting AFM height map is shown in Fig. 5.6b, after applying the same flattening method as that used for the CDI reconstruction. The AFM measurement shows an average height for the titanium features of 32.7 nm, which agrees exactly with the ptychography result within error bars.

Many small pieces of debris are visible in the AFM image shown in Fig. 5.6b, with heights above that of the patterned titanium. None of the EUV work was done in a cleanroom environment. The reason these are not visible in the CDI height map (Fig. 5.6a) is that the 3D information relies on the phase difference of light reflecting from the substrate versus the features (at 45°) and not on the absolute height difference. While the debris locations are still evident in the CDI reconstruction (Fig. 5.5d), the modulo 2π ambiguity of the phase information combined with the very short wavelength prevents us from extracting the absolute height information of all features. However, a tomographic or multi-wavelength approach would enable full 3D reconstructions of all features on a surface [87].

Finally, we note that previously it was believed that full knowledge of the probe was necessary when using Fresnel (curved wavefront) ptychography for phase retrieval [80]. However, we find that for ptychographic grids of 3×3 and larger with sufficient overlap between adjacent probe positions (60-70% area overlap [56]), the algorithm converges to a consistent result for the probe provided that the phase curvature of the starting guess differs by no more than 50% of the actual phase curvature. Even this condition is relaxed entirely in the case of isolated objects. To demonstrate this, we performed a separate ptychographic retrieval of the probe by scanning a 5 μm diameter pinhole across the beam near the focus. The probe that is retrieved using this method can be propagated to the sample plane for comparison to the probe found in the course of the sample reconstruction. We found very good agreement between the two probe reconstructions, independent of the accuracy of the starting guess for the probe.

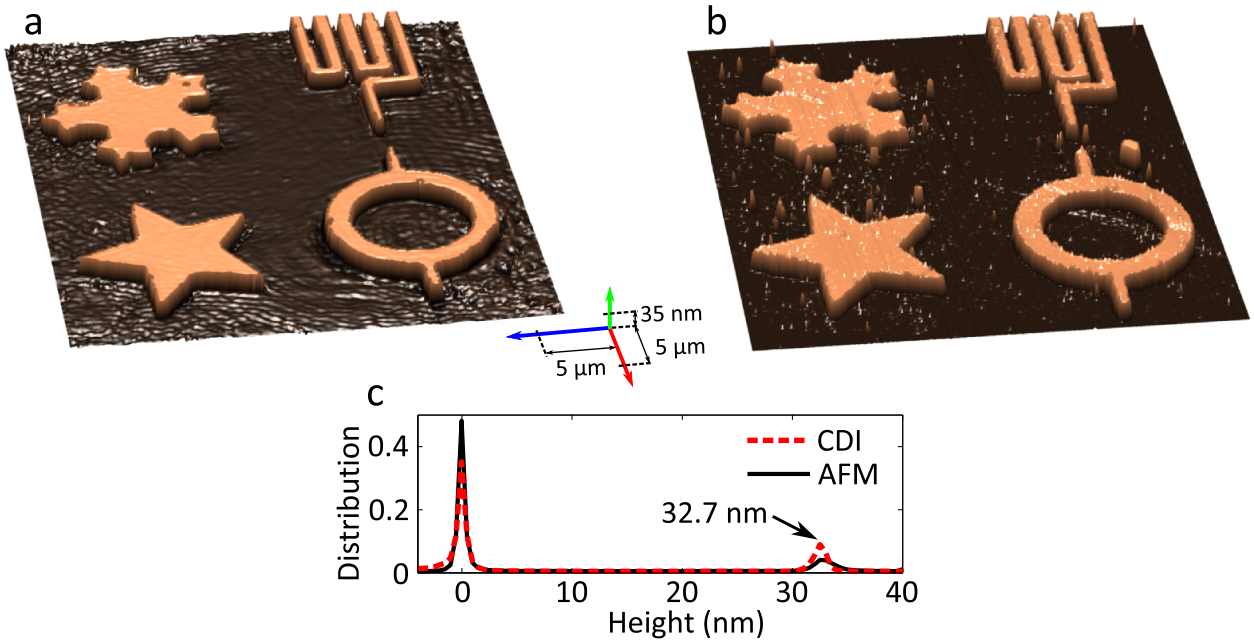

Figure 5.6: Height profile comparison between CDI and AFM. (a) 3D profile of the object based on ptychographic reconstruction. (b) 3D profile of the object based on an AFM measurement. Any features taller than 40 nm were thresholded to 40 nm for the 3D rendering. (c) Histograms of the height profiles shown in (a) and (b). The histograms were used to calculate the average feature thickness of 32.7 nm based on the both the CDI and AFM measurements. The scale axis shown in (a) is shared by both (a) and (b). Note that the large debris spot on the right of the AFM image was introduced after the CDI image was taken.Figure reproduced from Seaberg *et al.* [44].

5.2.6 Comparison between CDI reconstruction and SEM and AFM images

There are a number of defects visible in the sample image reconstructed through ptychographic coherent diffractive imaging (CDI) which are also visible in scanning electron microscope (SEM) and atomic force microscope (AFM) images. A visual comparison between the three techniques is shown in Fig. 5.7. Of the 7 defects pointed out in the figure, only defects 1-5 are visible in all of the images. The 6th and 7th defects are only visible in the CDI phase image and the AFM image. This is a demonstration of the fact that CDI has both amplitude contrast (analogous to SEM) and phase/height contrast (analogous to AFM).

5.2.7 High harmonic beam characterization through ptychography

To ensure that our recovery algorithm was correctly retrieving the probe illumination, we first characterized the extreme ultraviolet (EUV), high harmonic generation (HHG) beam by scanning a 5 μm diameter pinhole across the beam near its focus and reconstructed the illumination using ptychography. In this case, the pinhole can be thought of as the probe, while the beam is an effective object. The scan consisted of a 6 x 6 grid with 1 μm step size between adjacent scan positions. The reconstructed beam is shown in Fig. 5.8a.

The reconstructed beam was propagated to the sample position (200 μm upstream of the pinhole probe location) and calculated on the tilted plane (at 45°) using tilted plane correction, shown in Fig. 5.8b. Immediately after this ptychography scan, the pinhole probe was removed and the sample was translated such that the beam illuminated one of the star patterns on the sample (with reconstruction shown in Fig. 5.5d). We performed a 3 x 3 ptychographic scan across the star feature, with 2.5 μm step size. In this case, a probe starting guess consisting of a Gaussian amplitude profile with random phase sufficed to consistently retrieve the probe amplitude shown in Fig. 5.8c. As can be seen by comparison of Figs. 5.8b and c, the two beam characterization methods show very good agreement between both the phase and the amplitude. It should be noted that the HHG beam drifted slightly inside the adjustable aperture during the course of the two

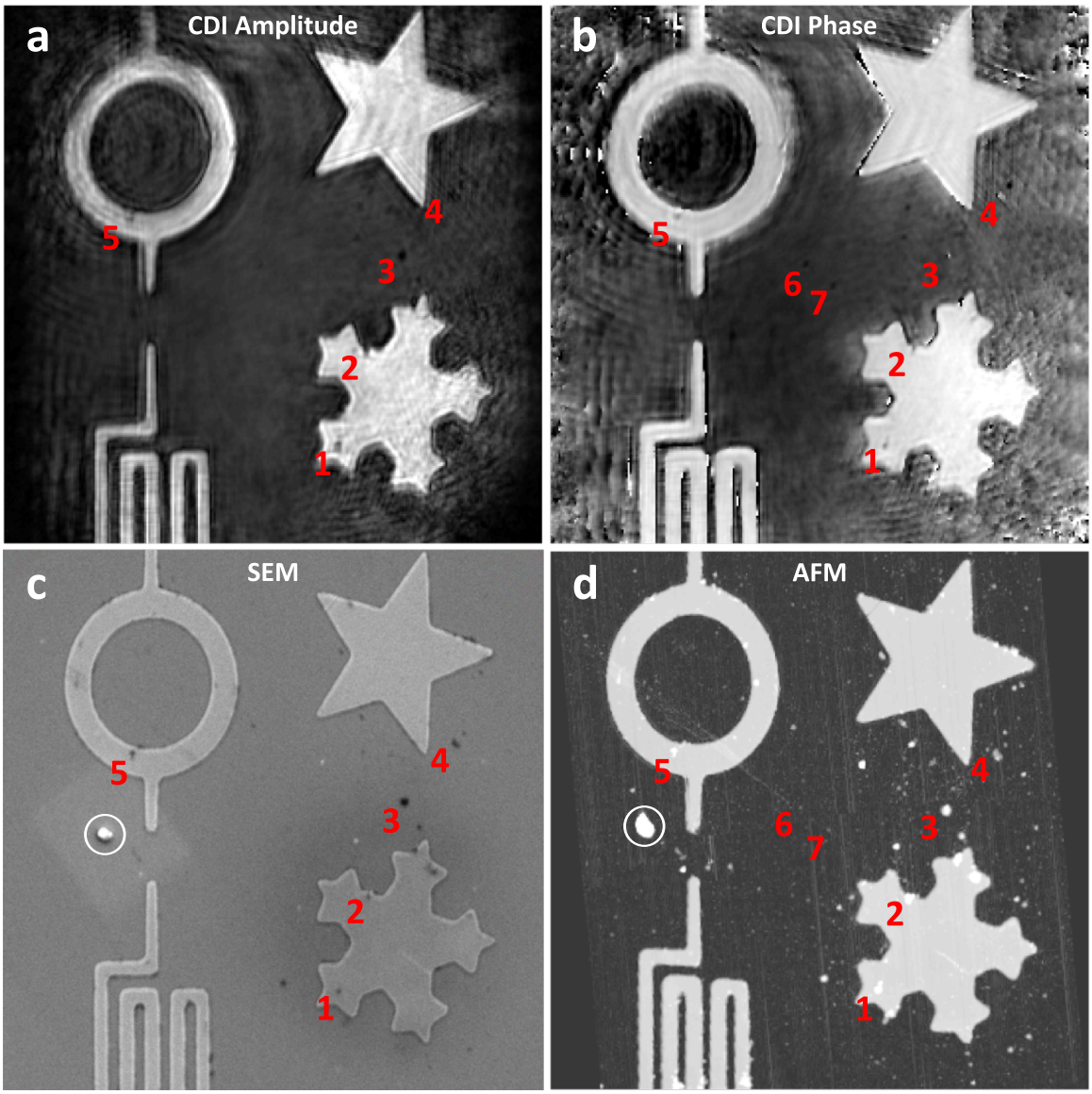

Figure 5.7: A visual comparison between the reconstructed CDI amplitude and phase with images obtained using SEM and AFM. (a) Reconstructed CDI amplitude image of the sample. (b) Phase of the reconstructed image. (c) SEM image of the sample. (d) AFM image of the sample. In the above images, 7 defects have been pointed out (located above and to the right of each number). Defects 1-5 are visible in all of the images, whereas defects 6 and 7 are only visible in the reconstructed phase and in the AFM image. The circled defect in (c) and (d) was a result of contamination after the CDI measurements were taken.Figure reproduced from Seaberg *et al.* [44].

scans, resulting in slightly different beam structure during the two measurements.

As a further consistency check, the probe reconstruction (shown in Fig. 5.5c) was propagated to the detector, and the tilted plane correction was undone in order to examine the result in the real coordinates of the detector. The result of these steps is shown in Fig. 5.9a. A comparison was made with a direct measurement of the unscattered beam by translating the sample to a featureless region of the silicon substrate, shown in Fig. 5.9b. As can be seen in Figs. 5.9a and b, while it is evident that, as in the above sample plane comparison, some beam drift occurred during the course of the ptychographic scan, the reconstructed probe is entirely consistent with the high harmonic beam used to illuminate the sample.

5.2.8 Conclusions

We have demonstrated the first general, tabletop, full field reflection mode CDI microscope, capable of imaging extended nanosurfaces at arbitrary angles in a non-contact, non-destructive manner. This technique is directly scalable to shorter wavelengths and higher spatial and temporal resolution, as well as tomographic imaging of surfaces. By combining reflection-mode CDI with HHG sources in the keV photon energy region, it will be possible to capture nanoscale surface dynamics with femtosecond temporal and nanometer spatial resolution.

5.3 Keyhole CDI in reflection

We had tried reflection keyhole CDI, even before reflection ptychography actually. The great challenge for we had met is that our knowledge of the probe beam is not accurate enough with previous methods. In transmission keyhole CDI discussed in Chapter 4, we obtain the probe beam by measuring foci positions, and assuming a spherical phase centered at these foci when it propagates to the detector. This method proves to be good enough with the two transmission results shown in Chapter 4. Accurate knowledge of the probe beam was not needed in those two results probably because: (a) for the first result, the sample is a binary object, allowing us to put on a strong amplitude support and phase constraint; (b) for the second result, the features are

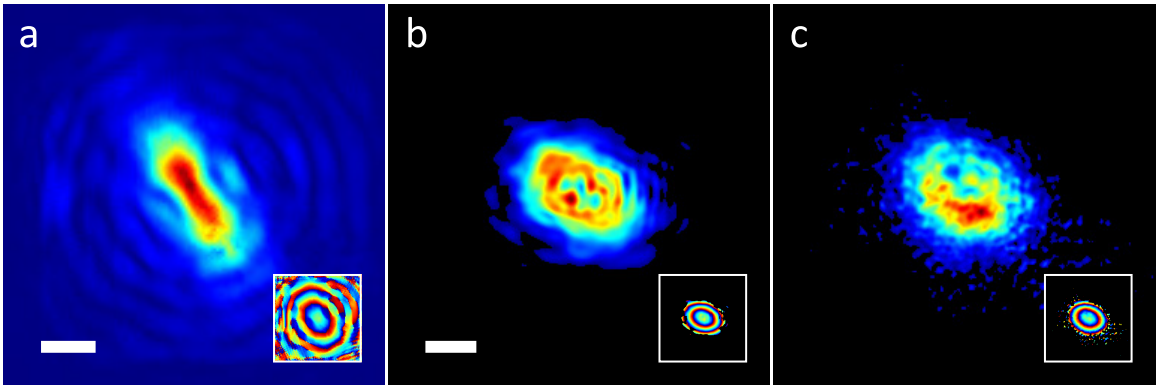

Figure 5.8: A comparison of separate reconstructions of the HHG illumination beam, using the beam as the object in one case and as the probe in the second case. (a) Reconstruction of the HHG beam near the focus using a 5 μm diameter pinhole probe. The main image displays the amplitude and the inset displays the phase. The scale bar has width 2 μm. (b) The result of propagating the reconstructed beam from (a) to the tilted sample plane. Again, the main image shows the amplitude and the inset shows the phase. The scale bar has width 5 μm. (c) The amplitude (main image) and phase (inset) of the reconstructed probe based on a 3 x 3 ptychographic scan across the one of the features on the titanium sample discussed in the text. The scale bar is shared with (b). Note that the beam amplitudes in (b) and (c) are displayed in the tilted sample coordinates, resulting in elongation in the horizontal direction. Figure reproduced from Seaberg *et al.* [44].

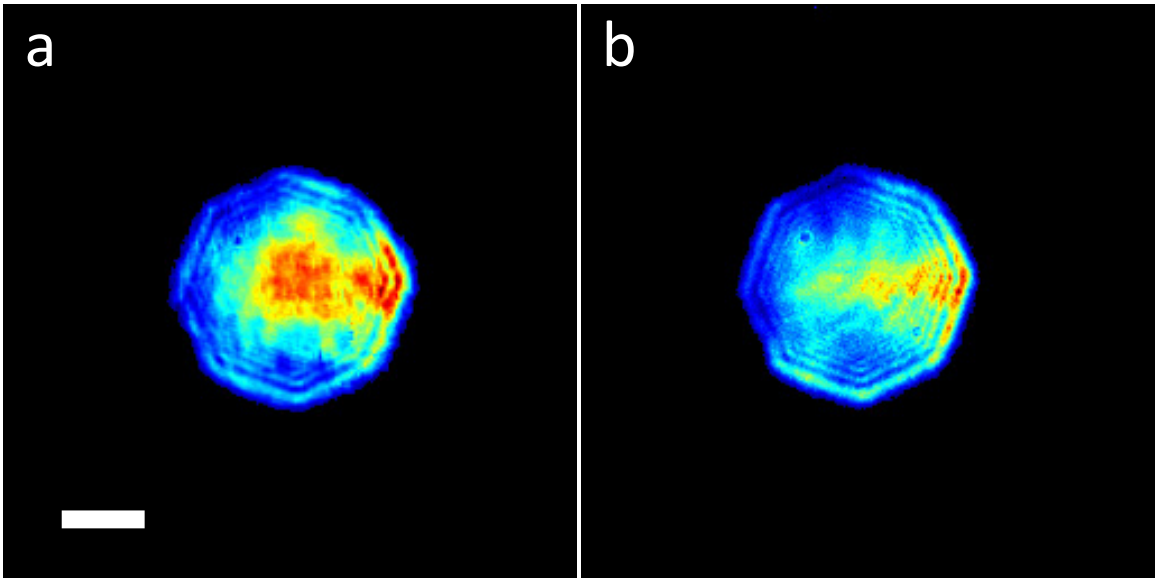

Figure 5.9: Comparison between the illumination reconstructed as a ptychographic probe and propagated to the detector, and the unscattered illumination measured directly on the detector (raw data). (a) The probe reconstruction from Fig. 5.5c, propagated to the detector plane. (b) The HHG beam measured directly on the detector by translating the sample to a featureless region of the silicon substrate. The scale bar in (a) has width 1 mm and is shared by (a) and (b). Figure reproduced from Seaberg *et al.* [44].

located within in an area that is much smaller than the beam size, thus the beam can regarded as uniform anyway. For the sample used in reflection ptychography in the last section, these two conditions are not met, and very accurate knowledge is necessary for the success of the keyhole CDI approach.

Thanks to ptychography, which reconstructs not only the object, but also the probe beam, with high accuracy, this challenge is overcome. With the beam reconstructed from the ptychography, we achieved the first reflection-mode keyhole CDI result on a tabletop in conjunction with the first general full-field demonstration of reflection ptychography CDI.

To reconstruct the image using keyhole CDI, tilted plane correction was first performed on one of the diffraction patterns, and the reconstruction was then achieved using the method described in [27]. First, a random phase was generated at the detector, and then the electric field was propagated back to the sample plane. The total reflectivity r was separated into two parts: a constant baseline reflectivity r_0 (the reflectivity of the substrate) and the difference in reflectivities between the features and substrate, Δr. The magnitude of r_0 can be found either by trial-and-error, or from the ptychographic reconstruction. Next, the product of the beam and r_0 is subtracted from the total exit surface wave (ESW). This quantity is then multiplied by the conjugate of the probe phase, which gives the exit surface wave of just the object. We used the shrink-wrap approach [55] to the field at the sample plane to apply the support constraint. The reconstructed sample is shown in Fig. 5.10b.

While the ptychography approach typically offers higher quality images than the keyhole CDI approach thanks to information redundancy in the multiple scans with overlap, it is impossible, difficult, or not desirable to perform ptychography scanning for certain situations. For example, in the "diffraction before destruction" regime, a single pulse is enough to damage the sample, not allowing the original sample to be scanned and illuminated with successive pulses. In these situations, it is preferable to use the keyhole CDI approach. One can simply use ptychography CDI as a beam characterization step, while the goal of sample reconstruction is achieved using keyhole CDI.

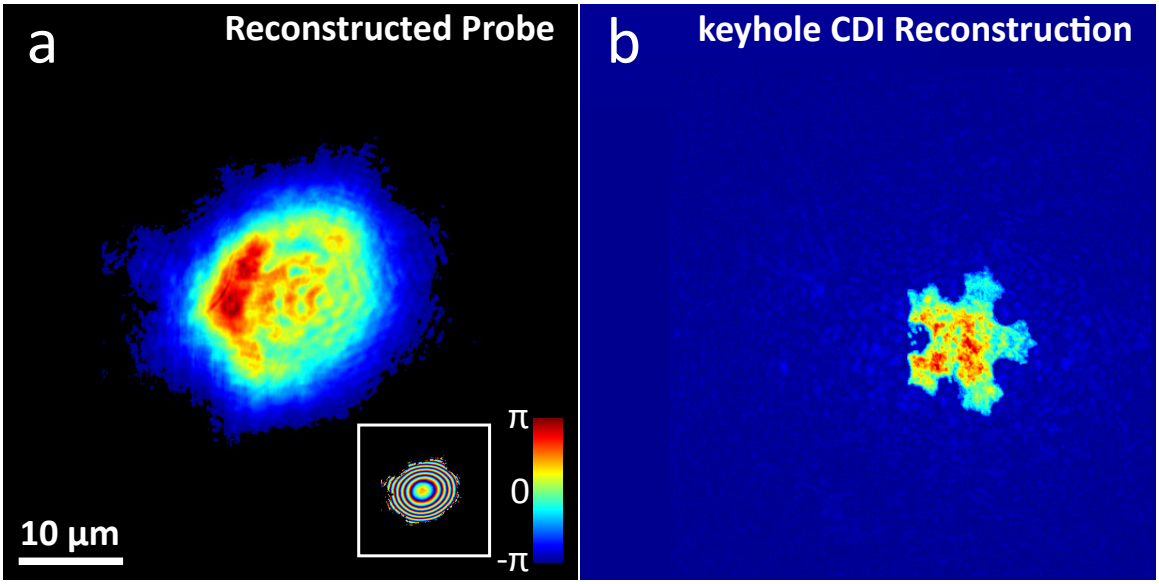

Figure 5.10: Reflection keyhole CDI reconstruction with the probe reconstructed from ptychography. (a) Reconstructed probe from ptychography. Adapted from Seaberg *et al.* [44]. (b) Reconstructed sample using only one diffraction pattern using the keyhole CDI approach. Scale bar, 10 µm, shared by (a) and (b).

Chapter 6

Surface Nano-imaging with High Lateral and Axial Resolution Using Tabletop EUV Ptychography

Building on the work described in the previous chapter, the work in this chapter is on surface nano-imaging with high lateral and axial resolution, and unprecedented image quality. The images from our tabletop EUV ptychography compare favorably with SEM and AFM, which are well-established techniques for imaging surfaces with nanometer resolution. This is achieved by performing reflection ptychography with a HHG source at a high numerical aperture (around 0.4). It works in a parallel, area-by-area scanning mode, providing powerful quantitative contrast, capable of capturing composition and topographical variation. Short wavelength illumination and high angle scatter leads to a very high, 40 nm by 80 nm (half-pitch), lateral resolution while quantitative phase information enables surface profilometry with ultra-high, 6-angstrom, axial resolution.

6.1 Experiment

To drive the HHG process, we focus ultrashort pulses from a titanium doped sapphire amplifier (central wavelength around 780 nm, pulse energy of 1.4 mJ, repetition rate of 5 kHz, 22 fs) into a 150 μm diameter hollow waveguide filled with argon (36 torr backing pressure) generating phase-matched, spatially coherent harmonics at wavelengths near 29 nm. After the waveguide, the HHG beam and CDI microscope were in medium vacuum ($\approx 10^{-6}$ torr) to avoid absorption of the EUV light. We use a pair of silicon rejecter mirrors set near Brewster's angle for 780 nm ($|r| \approx 0.36$, 29 nm) and two 200 nm thick aluminum filters to completely extinguish the fundamental light. As

shown in Fig. 6.1a , two 45° angle-of-incidence (AOI) flat multilayer mirrors select the 27th harmonic (29 nm) which is then focused near the sample by an ellipsoidal nickel-coated mirror set at 5° grazing incidence. The beam illuminates the sample at 50.57° AOI, and has a slight negative phase curvature due to the position of the sample relative to the focus. In this work the sample was titanium shapes patterned with E-beam lithography on a silicon substrate (SEM image shown in Fig. 6.1b). During the period after the sample was fabricated, incredibly fine height variations caused by contamination formed over the surface of the sample. As a demonstration of the quantitative contrast mechanism in CDI we measure the height of these variations with unprecedented accuracy in a non-destructive, non-contact manner and compare them to AFM and SEM for verification. An EUV sensitive CCD (Andor iKon-L, 2048×2048 pixel array, 13.5×13.5 μm^2 pixel size) is positioned 3.17 cm away from the sample and perpendicular to the specular reflection, leading to a high nominal numerical aperture of about 0.4. The sample is scanned with a step size of about 3 μm in both x- and y-directions, on a 18×11 rectangular grid (random offsets within 20% of the step size). With each exposure taking 0.1 seconds and 3 accumulated exposures for each of the 198 diffraction patters, the total exposure time was less than 1 minute for the whole 65 μm x 40 μm field of view, corresponding to 44 μm^2 per second exposure speed. To account for the non-normal incidence on the sample and the high angle scattering, tilted-plane correction [59, 79] must be performed to obtain the Fourier transform of the reflected exit surface wave on a linear grid of spatial frequencies. We employ an advanced, proprietary version of the correction for each of the 198 diffraction patterns. A representative measurement is shown in Fig. 6.1c, and the corrected amplitude is shown in Fig. 6.1d. The simple effect of tilting the sample away from normal incidence results in an increased geometric field of view with decreased resolution. As shown in Fig. 6.1d, the actual NA in x-direction is significantly reduced, compared with y-direction, resulting in decreased resolution in x-direction. The dashed rectangle in Fig. 6.1d shows the actual spatial frequency window we used for the reconstruction corresponding to a pixel size of 76 nm in x- and 38 nm in y-direction, sampled at 512 × 1024 with the same sampling frequency in both directions.

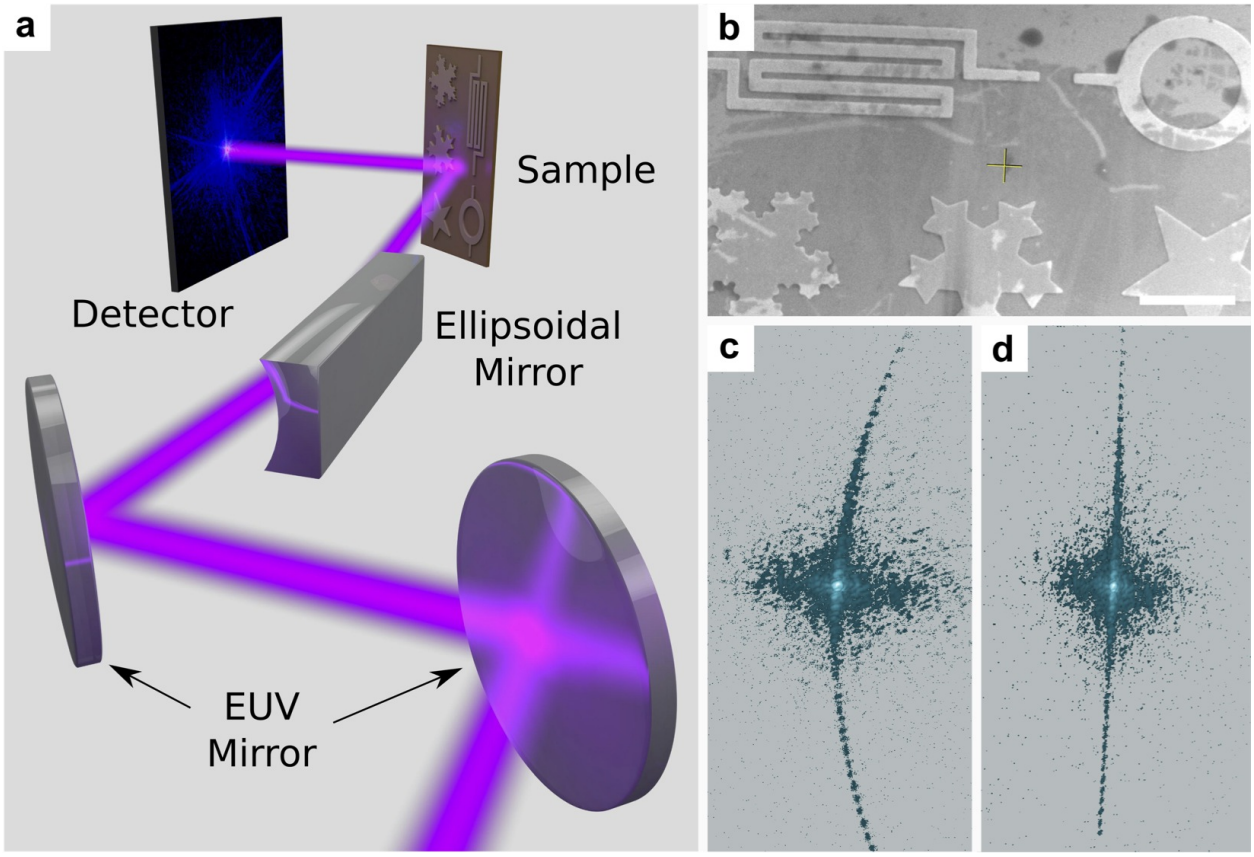

Figure 6.1: High NA reflection EUV ptychography experiment. (a) Schematic of the tabletop EUV microscope. (b) SEM of the sample (scale bar 10 μm). (c) Representative diffraction pattern. (d) Diffraction pattern after tilted plane correction.

6.2 Image reconstruction

To obtain the initial guess of the probe (beam), we measured the far-field beam reflected from a flat, substrate area. We assume a quadratic phase with x- and y-radius taken as the distance from the measured x- and y-focus to the detector [27]. We performed tilted plane correction on the beam field guess and then back-propagate to the sample plane to produce the initial probe guess. We use a constant value for the initial object guess. We use the ePIE [56] algorithm, and update only the object in the first two iterations. In the following 30 iterations, we update both the object and the probe. For the next 50 iterations, we update the object with position refinement [81]. For the next 600 iterations, we update the object, the probe and use position refinement. We finish the reconstruction procedure with 150 iterations of object update only. Our ePIE algorithm is implemented in C++, with OpenCV library support, on a NVIDIA Tesla K40c GPU. Each iteration takes at most 4.6 second (with probe, object update and position refinement on) for all the 198 diffraction patterns, each of which has a grid size of 512 by 1024. Main features become clear at less than 32 iterations (2.5 minutes), and the whole 832 iterations take less than one hour.

The reconstructed object has complex values proportional to $|r|\exp[\phi_r + i2\pi/\lambda \cdot (-2h\cos\theta_i)]$, where r is the complex Fresnel reflection coefficient of the sample with amplitude $|r|$ and phase ϕ_r, λ is the illumination wavelength, h is the height distribution of the sample, and θ_i is the angle of incidence. Due to the asymmetry in pixel x- and y-dimension, we interpolated the image to up-sample in x-direction by a factor of 2. The reconstructed amplitude and phase are shown in Fig. 6.2a and b, and for comparison Fig. 6.2c shows an SEM (model: FEI Nova NanoSEM 630) measurement. We find excellent agreement with the SEM in both the ptychography amplitude and phase images; while ptychography captures details of the slight surface variation that the SEM does not. In the highlighted region shown as a black rectangle in Fig. 6.2c, we compare images from 4 different measurements: ptychography amplitude, ptychography phase, SEM (with higher resolution and smaller field of view than Fig. 6.2 c) and AFM, in Fig. 6.2d-g respectively. We see that all measurements agree quite well except very faint details, such as slight height variation of

the surface due to debris, circled in white and red (dashed), which are clearly discernable in the ptychographic amplitude and phase but are nearly invisible to the SEM. The features circled in red (dashed), are completely unrecognizable in the SEM image while easily visible in the ptychographic phase image. It is evident that reflection mode CDI provides a powerful technique for surface profiling, enabling clear visualization of composition and topography with high contrast. The amplitude and phase of the reconstructed beam are shown in Fig. 6.2h and i. The beam had a $1/e^2$ diameter of ≈ 8 μm in x- and 6 μm in the y-direction. The majority of height variations within the sample area are mostly within 30 nm (except for sparse debris), much smaller than D/NA (D is the beam diameter), justifying modeling the exit surface wave as a multiplication of incident wave and the object response [42].

6.3 Lateral resolution characterization

We present three methods to characterize the lateral resolution: the phase retrieval transfer function (PRTF) [28,52,88], the modulation transfer function (MTF) (that is, the Fourier transform of the point-spread-function (PSF)), and the knife-edge assessment (10%-90% edge width).

The PRTF is the counterpart of MTF in coherent diffractive imaging. In conventional imaging, the MTF describes the response of an imaging system to various spatial frequencies. In coherent diffractive imaging the image forming hardware is replaced by a phase retrieval algorithm and correspondingly, the PRTF plays a similar role to the MTF by quantifying the repeatability and accuracy of the retrieved phase as a function of spatial frequency. The PRTF evaluates the combined effect of the signal-to-noise-ratio (SNR) of the diffracted wave and systematic errors that corrupt the convergence of the retrieval algorithm. Non-normal incidence causes a significant asymmetry of the measured range of spatial frequencies in the horizontal versus the vertical directions so we evaluate the PRTF in these two directions separately; PRTF is calculated as:

$$\mathrm{PRTF}(f_{1\mathrm{D}}) = \frac{\langle\langle|\langle E_{i,j}^{\mathrm{rec.}}(f_x, f_y)\rangle_i|\rangle_j\rangle_{1D}}{\langle\langle|E_j^{\mathrm{meas.}}(f_x, f_y)|\rangle_j\rangle_{1D}} \tag{6.1}$$

where $|E_j^{\mathrm{meas.}}(f_x, f_y)|$ is the magnitude of the measured electric field on the detector corresponding

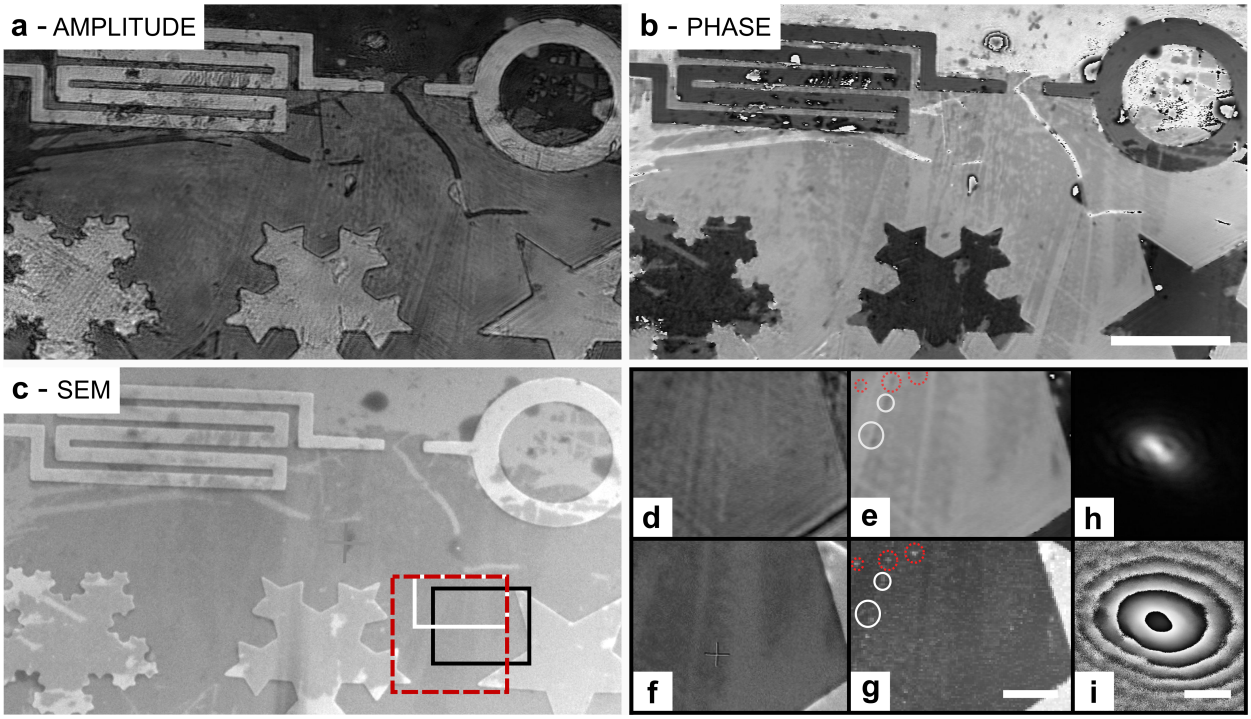

Figure 6.2: Images reconstructed from ptychography and comparison with SEM and AFM. (a) Ptychographic amplitude reconstruction. Scale bar: 10 μm, shared with (a-c). (b) Ptychographic phase reconstruction. (c) SEM for comparison. The area enclosed in the black rectangle is zoomed in and compared with the ptychography amplitude (d), ptychography phase (e), higher resolution SEM (f), and AFM (g) with 80 nm sampling step. Scale bar in (g), 2 μm, shared by (d-g). Areas highlighted in circles are compared in detail for the 3 techniques. (h) and (i) are the amplitude and phase of the reconstructed, incident high harmonic beam. Scale bar, 10 μm. The red and white rectangular regions are used later in the text.

to spatial frequency (f_x, f_y) and the j^{th} scan position, $E^{\text{rec.}}_{i,j}(f_x, f_y)$ is the reconstructed electric field at the i^{th} iteration, corresponding to spatial frequency (f_x, f_y) and the j^{th} scan position, $\langle\ \rangle_i$ and $\langle\ \rangle_j$ are averages over iterations and scan positions respectively, $\langle\ \rangle_{1\text{D}}$ means average over one direction to transform a 2-dimensional signal to a 1-dimensional signal. We average over all different f_y values when evaluating PRTF($|f_x|$), and over all different f_x values when evaluating PRTF($|f_y|$). We started with the 832nd iteration, which we considered the converged reconstruction. We averaged 100 iterations during which time only the object was updated. The calculation result is shown in Fig. 6.3 a. We observe that the PRTF values only slightly decrease with increasing spatial frequency in both horizontal and vertical directions and are still above 0.98 at the maximum spatial frequencies. This large PRTF value is a manifestation of good SNR across the whole frequency range and accurate measurement of parameters. We conclude that the PRTF approach supports a spatial resolution of 73.2 nm in horizontal direction and 36.6 nm in vertical direction but is not sufficient to fully characterize the lateral resolution.

In the second method, we evaluated the modulation transfer function of our CDI microscope. In the region of interest shown in Fig. 6.2 c (red dashed rectangle), we took a corresponding AFM measurement with a 10 nm probe diameter, and 40 nm sampling step (model: Digital Instruments Dimension 3100). Fig. 6.3c shows the power spectral density (PSD) of the two images from the ptychography phase measurement and AFM measurement plotted together (ptychographic PSD in fine dashing). By taking a square root of the ratio of the ptychographic phase PSD and the AFM PSD, we obtain a relative MTF: the MTF of the ptychography phase imaging divided the MTF of the AFM image. In the absence of a much higher resolution AFM image, we are limited to claiming a relative MTF rather than absolute. However, if we reasonably assume the AFM image has a MTF value above 50% at the highest spatial frequency (39.1 nm, half pitch), the fact that the relative MTF is above 22% in both x- and y- directions at the maximum spatial frequency (clearly above 11%; which is the Rayleigh resolution contrast level) allows us to conclude our resolution is 73.2 nm in horizontally and at least 39.1 nm vertically. Finally, we characterize the resolution of our microscope by measuring the 10% to 90% width of two edges. Compared with AFM, where

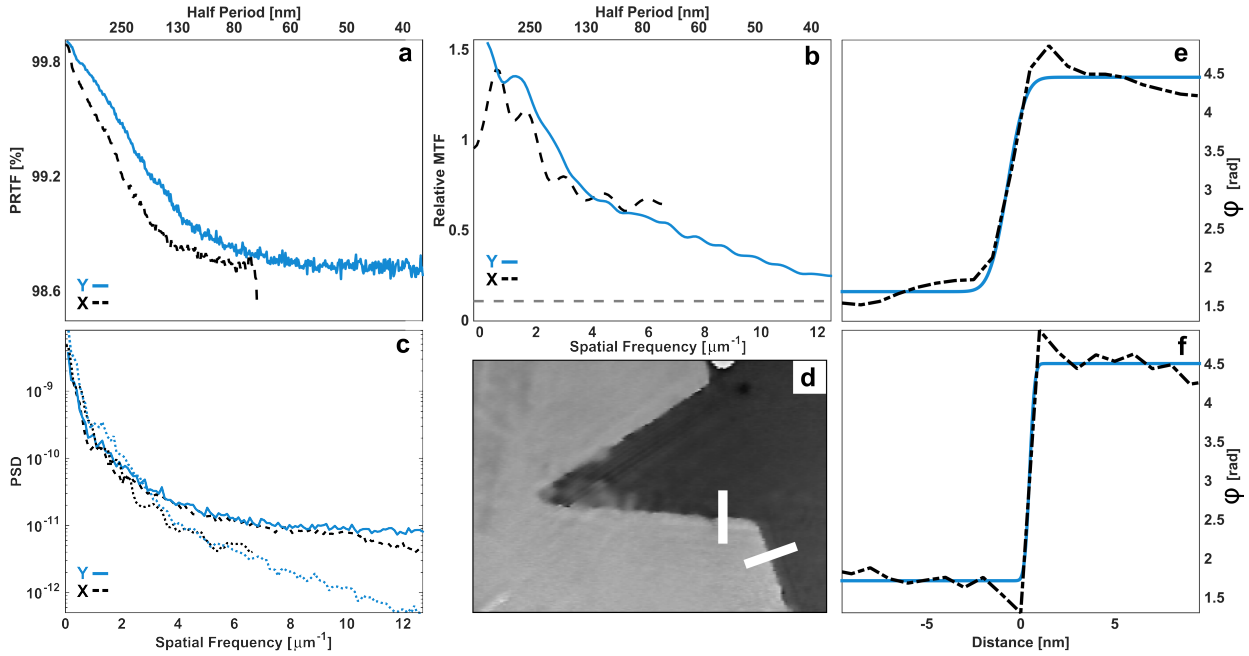

Figure 6.3: Characterization of the lateral resolution. (a) Phase retrieval transfer function. (b) Relative modulation transfer function of the ptychographic phase and AFM (grey dashed (horizontal) line: 11% contrast level corresponding to Rayleigh resolution). (c) Power spectral density. Both AFM and CDI PSDs are shown; lines with fine dashing are CDI. (d) shows the edges where we measure the 10% to 90% edge width of the phase reconstruction. (e) Profile measured nominally in the x-direction. (f) Profile measured nominally in the y-direction. Fits to the error function compliment, and are also shown in (e-f) as solid lines (blue) (both R^2 values ≈ 0.99).

the image contrast comes solely from height differences, ptychography derives its contrast from the reflected complex exit surface wave. We choose two profiles nominally in the x-direction and nominally in the y-direction (shown as white solid lines in Fig. 6.3 d). The feature edges along these profiles are clean, sharp, and near the center of the ptychographic scan area avoiding insufficient overlap that can cause decreased reconstruction quality at the egdes. The phase along these two profiles are shown in Fig. 6.3e andf respectively. We see that in x-direction, the 10%-90% width occurs across $\approx$ 2 pixels (73.2 nm), and the y-direction rises in only 1 pixel (36.6 nm). The two rising edges agree well with the error function compliment (ERFC) fit that have 10%-90% widths of 73.2 nm and 20.9 nm (smaller than 36.6 nm) respectively. (The R^2 value in either ERFC fits was $\approx$ 0.99). The resolution characterized via three different approaches all support the conclusion that we have spatial resolution of 73.2 nm in horizontal direction and 36.6 nm in vertical direction, corresponding to the highest measured spatial frequencies.

6.4 Axial resolution characterization

In reflection CDI, we can calculate the height from the reconstructed phase in a similar way to holography. The reconstructed phase is the sum of the geometric phase that is proportional to height, $2\pi/\lambda \cdot (-2h\cos\theta_i)$, and the phase of the complex reflection coefficient ϕ_r. Figure 6.4a shows the reconstructed phase in a selected region, and Fig. 6.4b shows the calculated height. Due to the lack of an absolute reference in CDI only relative phase values are accessible so when the reflecting material is monolithic, the retrieved phase is purely geometric and ϕ_r cancels exactly. When considering features that have different composition, ϕ_r is also different and must be taken into account. In the white rectangular area shown in Fig. 6.2c, the region between the stars has the same composition, a contamination layer above the Si substrate, thus we consider only the reflection from this top layer and neglect the contribution from the silicon substrate since it has a much weaker reflection (less than 10 % determined from Fig. 6.2 a). Visually, the ptychographic height measurement (Fig. 6.4d) shows good qualitative agreement with the AFM (Fig. 6.4e). To characterize the axial resolution of our microscope we examine surface variations highlighted in the

white rectangular region, shown in Fig. 6.2c. It is important to note that we do not expect the lateral ptychographic resolution to be comparable with the AFM resolution in this area: because wide-angle diffraction from weakly scattering features has poor SNR, the combination of strong signal from the titanium features and detector saturation leads to a loss of fidelity in this region. However, this does not affect the reconstructed height when the ratio of the feature width to the width of the PSF is much greater than unity, which is true for these surface features. On the other hand, this condition is not met for the very fine debris apparent in the AFM image. In order to more accurately compare the height variations measured by either AFM or ptychography we apply two filters. First, we simply remove points outside the wide, trench features using a histogram filter in both the AFM and ptychographic images, shown in Fig. 6.4g. Second, we convolve a Gaussian PSF ($\sigma = 70$ nm) with the AFM measurement. The width of the Gaussian PSF was chosen to minimize the overall error between the AFM and ptychographic reconstruction. The results of either the histogram-filtering or PSF-filtering are shown in Fig. 6.4f and g; these are compared against the ptychographic height map, Fig. 6.4d. The three panels shown in Fig. 6.4c are a histogram of the height difference between the ptychographic reconstruction and the AFM image for different filters. The top-most histogram and corresponding Gaussian fit with reported width, $\sigma = 4.3$ Å compares the unfiltered AFM (Fig. 6.4e) directly to the ptychographic reconstruction. The center histogram and corresponding Gaussian fit with reported width, $\sigma = 3.7$ Å compares the histogram-filtered, ptychographic height map to the histogram-filtered AFM (Fig. 6.4f). The bottom-most histogram and corresponding Gaussian fit with reported width, $\sigma = 3.2$ Å compares the ptychographic height map to the Gaussian-PSF filtered AFM image (Fig. 6.4g). Two representative profiles are shown in Fig. 6.4c corresponding the white dashed line in Fig. 6.4e. The top-most panel is a direct comparison between the unfiltered AFM and ptychographic height reconstruction. The bottom-most panel compares the PSF-filtered AFM with the ptychographic reconstruction. The three comparisons (Fig. 6.4c) are in good relative agreement however; the fact that both filtered version of the AFM image show lower relative difference results from the omission of spurious debris.

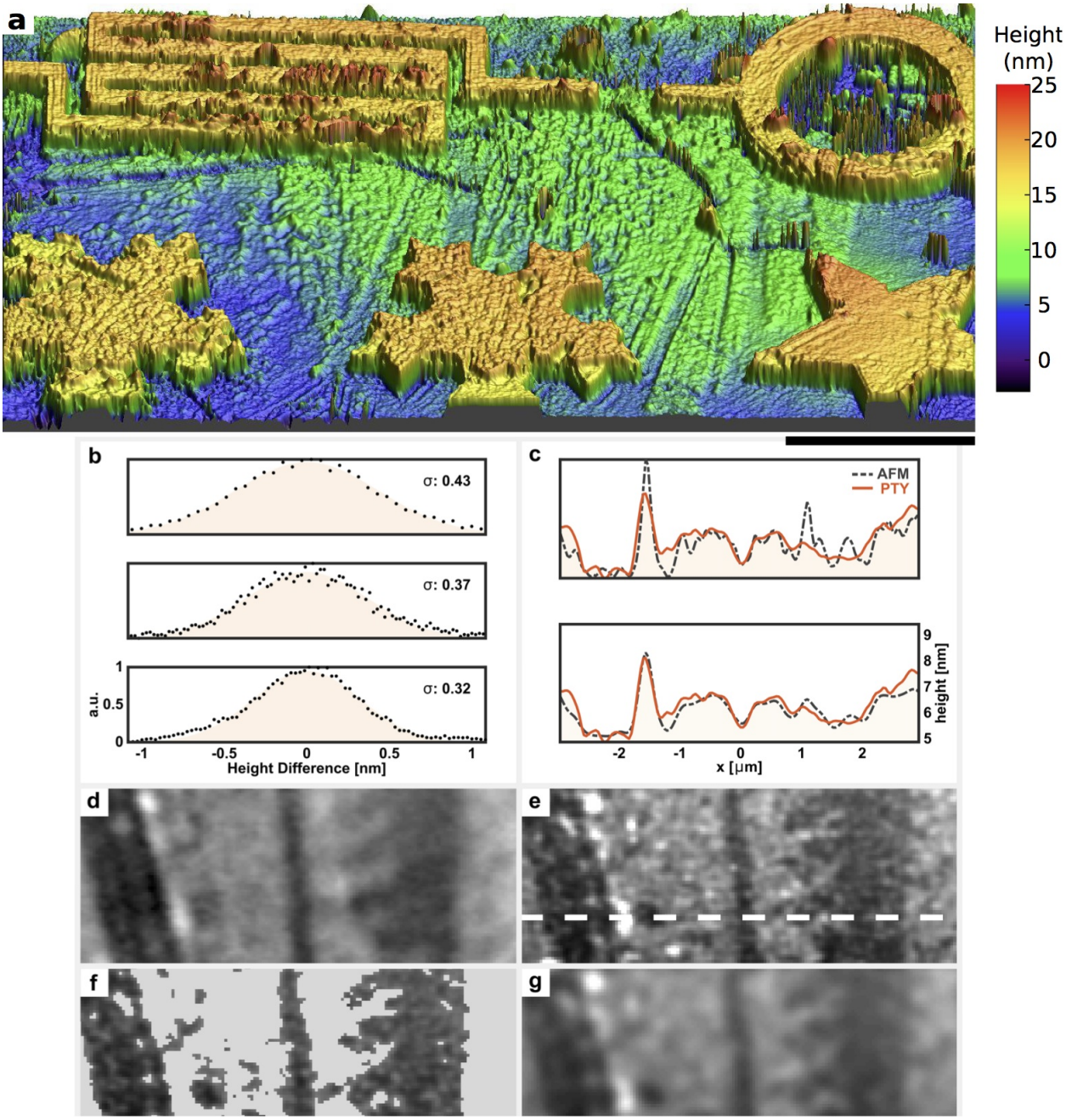

Figure 6.4: Height calculated from the reconstructed phase. (a) Three-dimensional rendering of surface features imaged by ptychographic CDI. Scale bar, 10 μm. (b) Histograms of the height differences measured by ptychography and AFM. The top panel includes no filtering (comparing (d) to (e) directly). The middle panel uses a histogram filter to remove values outside the trench features (comparing (d) to (f)). The bottom panel used a Gaussian-PSF to smooth fine debris in the AFM (comparing (d) to (g)). Scale bar, 2 μm shared with (d-g). (c) Comparative profiles taken along the dashed (white) line in (e). The top panel compares (d) to (e). The bottom panel compares (d) to (g). After smoothing, the 2-σ (95% confidence interval) width, in height difference is $\approx$ 6 Å.

6.5 Discussion

We have demonstrated surface imaging with unprecedented fidelity comparing favorably with well-established techniques such as SEM and AFM. We achieve a lateral resolution of 40 nm vertically by 80 nm horizontally, and a sub-nanometer axial precision. EUV reflection provides a powerful imaging contrast mechanism; it has composition sensitivity unlike AFM, and improved contrast compared to SEM. Instead of serial, point-by-point scanning, EUV ptychography employs parallel, area-by-area scanning for imaging, significantly decreasing the time for scanning, making source flux the only practical limit for high volume imaging. The increase of the imaging speed makes this tool attractive for real applications involving large-area imaging, such as semiconductor inspection. In contrast to AFM that works in a contact or tapping mode, this microscopy provides a long working distance: in this work, only limited by sample-detector distance (31.66 mm). Ptychography CDI does not require the sample to be conductive as SEM does. The resolution reported in this work can be improved with shorter wavelengths, although for most materials, this will come at the cost of decreased reflectivity. At smaller grazing incidence angle, by taking an additional data set with the sample rotated at 90 degrees, we can ensure high resolution in both directions.

Chapter 7

Hyperspectral Imaging with Harmonic Combs and Ptychography

While previous chapters present the work on removing obvious roadblocks on the way of making HHG CDI a general microscopy tool, this chapter discusses a powerful capability of ptychography CDI that is unexpected from the early beginning – the capability to decompose incoherent superposition of different modes, due to information redundancy provided by the overlap in the scanning.

This chapter will first introduce the principles of decomposing incoherent superposition with ptychography. Then preliminary results of our ongoing work are presented on decomposing incoherent superposition from different wavelengths in a multi-order HHG source. These results represent a proof-of-principle demonstration of hyperspectral imaging using a HHG source and the ptychography method.

7.1 Decomposing incoherent superposition with ptychography

We have seen in the previous chapters that information redundancy provided by the overlap in the scanning have brought several unique capabilities to this technique: the reconstruction of the sample is more robust; not only the sample but also the illuminating beam itself can be reconstructed; some measurement errors in the experiment, such as position errors in the scanning stages, can be automatically corrected. Recently, another advantages have been added to the list: there can be enough redundant information in ptychography to decompose incoherent superposition on the detector. In 2013, Thibault and Menzel published a paper titled "Reconstructing state

mixtures from diffraction measurements" [89]. In this paper, they demonstrated experimentally the diffractive imaging of a sample with X-ray that has only partial spatial coherence. They also successfully decomposed simultaneously the five dominant spatial modes in the X-ray beam. This is a conceptually surprising result: as the name indicates, CDI relies on high spatial coherence of the illumination for imaging; but for ptychography, partially coherent illumination source can also work. There is enough information provided by the overlap in the scanning to decompose the incoherent superposition into its individual coherent components.

Several sources of decoherence in scattering experiments are identified in Ref. [89], such as spatial and temporal incoherence of the probing radiation, vibration of the sample, etc. Other sources include superposition of different polarizations. The case of temporal incoherence is very interesting: if a multi-colored illumination is used, can ptychography diffractive imaging separate the responses of the sample to different colors simultaneously? A positive answer to this question was given by Batey, *et al.* [87]. In their experiments, wavelengths of 410 nm, 530 nm, 632 nm from three laser diodes illuminated the sample at the same time. They successfully recovered the sample response for each of these three colors with ptychography. They called this technique "ptychographical information multiplexing" (PIM).

It is apparent that the modulus constraint used in multi-color diffractive imaging should be different from that used in monochromatic CDI as shown in Eq. 3.46. The projection to this new modulus constraint can be written as [87]:

$$\tilde{P}_{m,\mathrm{MC}} U_j = \frac{|U|_m}{\sqrt{\sum_j |U_j|^2}} U_j \tag{7.1}$$

where $\tilde{}$ indicates the projection happens in the Fourier space instead of the real space, subscript "MC" indicates multicolor, U_j is the field on the detector plane for the jth color, $|U|_m$ is the measured modulus of the field. This formula works for other sources of incoherence too, in which case j means the jth mode, or state.

7.2 Experiment and results

In our work, we combined the PIM technique with our EUV HHG source. The experimental setup is shown in Fig. 7.1(a). The HHG process is driven using a Ti:sapphire amplifier system (KMLabs Dragon, 785 nm, 5 kHz, 1.5 mJ, 22 fs). The laser is coupled into a 150 μm inner diameter hollow-core waveguide, which is filled with argon at 60 torr to produce several phase-matched harmonics near 29 nm. In contrast to previous experiments, this experiment does not not use any EUV multilayer mirror to select one harmonic; instead all the four phase-matched harmonics are sent onto the sample. A low-resolution spectrum measured by a two-dimensional grating on the same plane as the sample is shown in Fig. 7.1(b). For the multiple-wavelength hyperspectral measurement, the harmonics are refocused using an elliptical mirror at 5° glancing incidence. The sample (titanium features patterned on silicon) was placed at the beam focus at 50° angle of incidence, where all the harmonic beams have diameter ≈10 μm. The incoherent superposition of the diffraction intensity from all four colors was measured by an EUV-sensitive CCD detector placed 55 mm away from the sample. The detector was positioned normal to the specular reflection of the beam from the sample. The hyperspectral ptychographical data set consisted of scatter patterns collected at 150 different scan positions, with a step size of 1 μm between positions.

We use the PIM technique to reconstruct the sample's response to each of the four harmonic orders, with the amplitudes shown in Fig. 7.1 (c-f) and phases shown in Fig. 7.1(g-j) for four colors respectively. These reconstructions seem to have degraded quality compared with single color reconstruction. The probable reason is that while the signal-to-noise ratio for the sum of all four colors is about the same as for the single-color situation, after divided, or decomposed into four colors, each color has much lower SNR leading to lower image quality. This is especially true for the fourth color. As seen from the spectral weights in Fig. 7.1b, the fourth color is much weaker than other three colors; and as shown in the reconstructions, the sample is not recognizable for the fourth color.

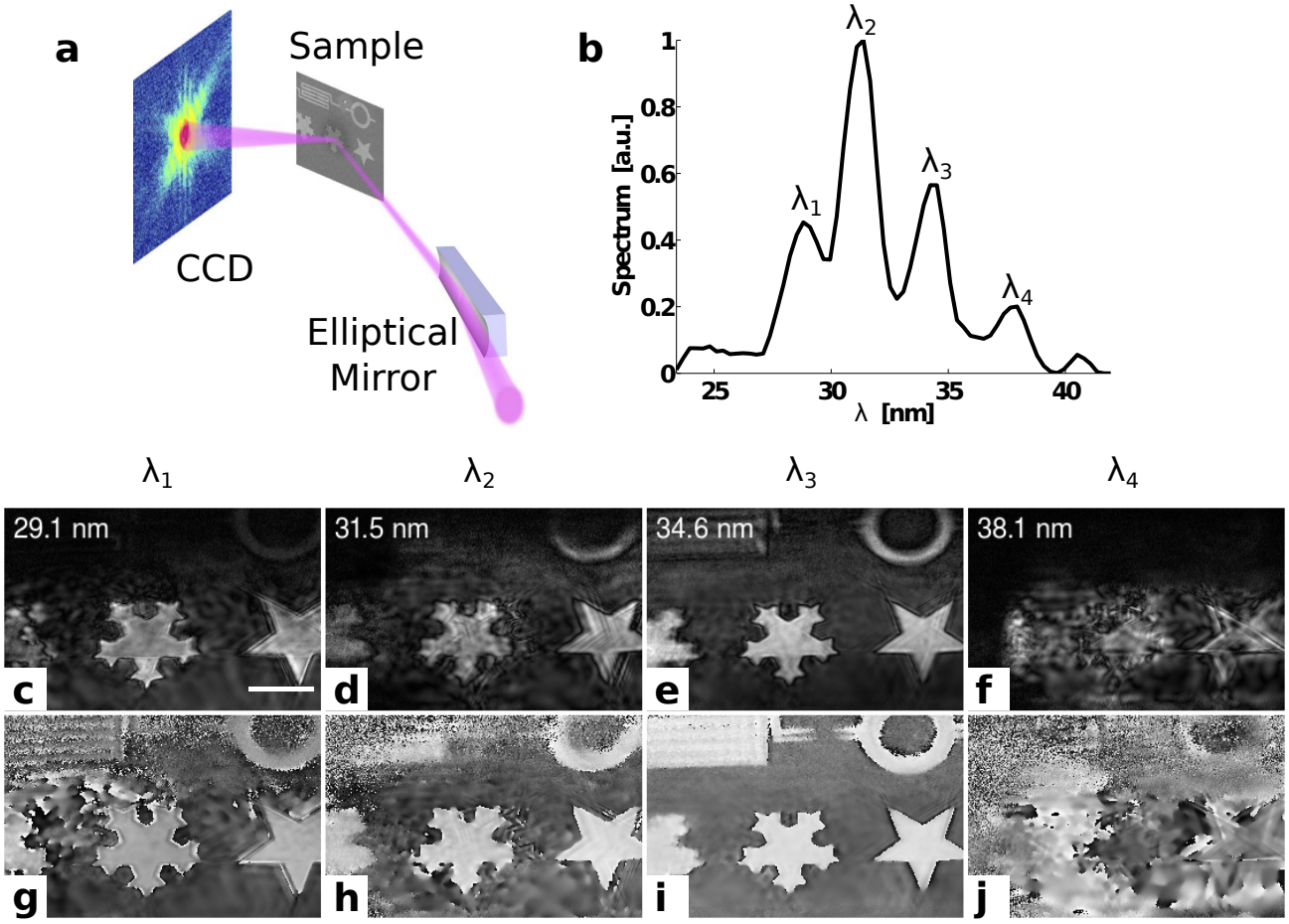

Figure 7.1: Setup and results of hyperspectral imaging with four harmonic orders using ptychographical information multiplexing. (a) Experimental setup. (b) Measured spectrum with a low resolution 2D grating sample. Simultaneous reconstructions for the four wavelengths are shown in (c-f) for the amplitude and (g-j) for the phase. Scale bar: 10 μm, shared by (c-j).

7.3 Conclusion

Here the source in our experiment has a $\lambda/\Delta\lambda$ of $\approx 27\%$. Before the invention of the technique used in this chapter, it is extremely difficult to use such a broadband light source to perform diffractive imaging. It represents a great step forward to reconstruct anything with a broadband source, but even more is achieved here: ptychography allows for individual reconstruction of the colors that illuminate the sample simultaneously, which represents a simple yet powerful approach for hyperspectral imaging, or spectro-microscopy.

More colors bring more information and less ambiguity in imaging, a capability that color-vision brings to humankind. For the specific experiment in this chapter, with phase reconstructed for more than one color, the calculated height has less ambiguity resulting from the 2π phase wrapping problem [87]. In the future, this technique promises to enable spectroscopic EUV/X-ray imaging by taking advantage of the various element-specific absorption edges at EUV wavelength. For example, when combined with this technique, the water window wavelengths generated from HHG [16] can be used to obtain elemental contrast in biological specimens.

Chapter 8

Future

Work presented in the previous chapters opens up various applications for this HHG CDI microscope. At the top of the list is ultrafast dynamic imaging that makes use of the ultrashort, femtosecond pulse duration of the HHG source. Investigating ultrafast dynamics at the nanometer scales can find applications in the study of ultrafast heat transport and surface acoustic wave dynamics at the nanoscale [73, 74, 90], ultrafast magnetic dynamics [75, 82, 91, 92], fracture dynamics, shock formation, ablation, plasma formation under extreme conditions. Two methods exist to exploit the ultrashort pulse duration of a HHG source. The first is the pump-probe method, which relies on repeatable excitation of the sample. This method with a HHG source has been applied to study of dynamics of ultrafast heat transport and surface acoustic wave , and ultrafast magnetics [75,82,91,92]. These studies can be extended to an imaging mode to investigate the local behavior. When radiation-induced damage and intrinsic sample movement prevent the repeatable excitation of the sample, the single-shot method is desirable. Proof-of-principle experiments have been demonstrated on both FEL [93, 94] and HHG [95] sources. Single-shot experiments typically requires high photon counts from a single pulse, but the photon count requirement can be dramatically lowered in some cases with advanced algorithms such as the expectation maximization algorithm [96]. It seems possible to apply these algorithms to a current HHG source to perform single-shot experiments.

Any improvement on the HHG probe, or the CDI image-forming method, can bring improvements to the microscopy that combine these two elements. On the HHG probe side, it has been

demonstrated that this source can generate water-window photons (between the carbon and oxygen K-shell absorption edges at 284-540 eV) [16]. This spectral range is of particular importance for biological imaging as in this range water appears transparent while nitrogen and other biological elements are absorbing. In 2012, Popmintchev, Chen *et al.* further extended the HHG photon energy to above 1.6 keV [18]. Sub-nanometer resolution is promised if this new high photon energy HHG source can be applied to CDI, which would face two challenges: limited flux at this high energy, and the supercontinua, ultra-broadband spectrum: it has a continuous spectrum ranging from 200 eV all the way to 1.6 keV. Either it needs to be monochromatized, or certain imaging algorithm, such as the PIM algorithm shown in Chapter 7 that deals with broadband illumination needs to be applied to the diffraction data. A third interesting development in the HHG source is the generation of circularly polarized HHG [14]. Combined with CDI, it would enable imaging of magnetic nanodomains based X-ray magnetic circular dichroism [97]. On the CDI image-forming side, Chapter 7 provides a proof-of-principle demonstration of hyperspectral imaging, where the difference in contrasts for each color comes from the phase relative to the surface profile. One possible extension of hyperspectral imaging would be to image the distribution of different elements inside the spectrum.

Looking further ahead, the microscopy that combines HHG and CDI in this thesis is poised to image with nanometer spatial resolution and femtosecond temporal resolution, studying the world at the ultrasmall space limit and the ultrafast time limit.

Bibliography

[1] Richard P Feynman. There's plenty of room at the bottom. Engineering and science, 23(5):22–36, 1960.

[2] Anne Sakdinawat and David Attwood. Nanoscale X-ray imaging. Nature photonics, 4(December), 2010.

[3] Henry N. Chapman and Keith A. Nugent. Coherent lensless X-ray imaging. Nature Photonics, 4(12):833–839, December 2010.

[4] Rolf Erni, Marta Rossell, Christian Kisielowski, and Ulrich Dahmen. Atomic-Resolution Imaging with a Sub-50-pm Electron Probe. Physical Review Letters, 102(9):096101, March 2009.

[5] D. Gabor. A new microscopic principle. Nature, 161(4098):777–778, May 1948.

[6] Jianwei Miao, Pambos Charalambous, Janos Kirz, and D Sayre. Extending the methodology of X-ray crystallography to allow imaging of micrometre-sized non-crystalline specimens. Nature, 400(July):342–344, 1999.

[7] Richard L Sandberg, Ariel Paul, Daisy A Raymondson, Steffen Hädrich, David M Gaudiosi, Jim Holtsnider, Raanan I Tobey, Oren Cohen, Margaret M Murnane, Henry C Kapteyn, Changyong Song, Jianwei Miao, Yanwei Liu, Farhad Salmassi, and Steffen Ha. Lensless Diffractive Imaging Using Tabletop Coherent High-Harmonic Soft-X-Ray Beams. Physical Review Letters, 99(9):098103, August 2007.

[8] Matthew D Seaberg, Daniel E Adams, Ethan L Townsend, Daisy A Raymondson, William F Schlotter, Yanwei Liu, Carmen S Menoni, Lu Rong, Chien-Chun Chen, Jianwei Miao, Henry C Kapteyn, and Margaret M Murnane. Ultrahigh 22 nm resolution coherent diffractive imaging using a desktop 13 nm high harmonic source. Optics Express, 19(23):22470–9, November 2011.

[9] D Attwood. Soft X-Rays and Extreme Ultraviolet Radiation: Principles and Applications. Cambridge University Press, 2007.

[10] D Paganin. Coherent X-Ray Optics. Oxford Series on Synchrotron Radiation. OUP Oxford, 2006.

[11] J Bokor, P. H. Bucksbaum, and R. R. Freeman. Generation of 355-nm coherent radiation. Optics Letters, 8(4):217, April 1983.

[12] A. McPherson, G Gibson, H Jara, U Johann, T S Luk, I. A. McIntyre, K Boyer, and C K Rhodes. Studies of multiphoton production of vacuum-ultraviolet radiation in the rare gases. Journal of the Optical Society of America B, 4(4):595, April 1987.

[13] P. Corkum. Plasma perspective on strong field multiphoton ionization. Physical Review Letters, 71(13):1994–1997, September 1993.

[14] Ofer Kfir, Patrik Grychtol, Emrah Turgut, Ronny Knut, Dmitriy Zusin, Dimitar Popmintchev, Tenio Popmintchev, Hans Nembach, Justin M. Shaw, Avner Fleischer, Henry Kapteyn, Margaret Murnane, and Oren Cohen. Generation of bright phase-matched circularly-polarized extreme ultraviolet high harmonics. Nature Photonics, 9(February):99–105, December 2014.

[15] Charles G Durfee Iii, Andy R Rundquist, Sterling Backus, Catherine Herne, Margaret M Murnane, Henry C Kapteyn, and Charles Durfee. Phase Matching of High-Order Harmonics in Hollow Waveguides. Physical Review Letters, 83(11):2187–2190, September 1999.

[16] M.-C. Chen, P. Arpin, T. Popmintchev, M. Gerrity, B. Zhang, M. Seaberg, D. Popmintchev, M. M. Murnane, and H. C. Kapteyn. Bright, Coherent, Ultrafast Soft X-Ray Harmonics Spanning the Water Window from a Tabletop Light Source. Physical Review Letters, 105(17):173901, October 2010.

[17] Randy A Bartels, Ariel Paul, Hans Green, Henry C Kapteyn, Margaret M Murnane, Sterling Backus, Ivan P Christov, Yanwei Liu, David Attwood, and Chris Jacobsen. Generation of spatially coherent light at extreme ultraviolet wavelengths. Science, 297(5580):376–378, 2002.

[18] Tenio Popmintchev, Ming-Chang Chen, Dimitar Popmintchev, Paul Arpin, Susannah Brown, Skirmantas Alisauskas, Giedrius Andriukaitis, Tadas Balciunas, Oliver D Mücke, Audrius Pugzlys, Andrius Baltuska, Bonggu Shim, Samuel E Schrauth, Alexander Gaeta, Carlos Hernández-García, Luis Plaja, Andreas Becker, Agnieszka Jaron-Becker, Margaret M Murnane, Henry C Kapteyn, Skirmantas Ališauskas, Tadas Balčiunas, and Andrius Baltuška. Bright coherent ultrahigh harmonics in the keV x-ray regime from mid-infrared femtosecond lasers. Science (New York, N.Y.), 336(6086):1287–91, June 2012.

[19] R. A. Bartels, A. Paul, M. M. Murnane, H. C. Kapteyn, S. Backus, Y. Liu, and D. T. Attwood. Absolute determination of the wavelength and spectrum of an extreme-ultraviolet beam by a Young's double-slit measurement. Optics Letters, 27(9):707–709, May 2002.

[20] JM Rodenburg. Ptychography and Related Diffractive Imaging Methods. Advances in Imaging and Electron Physics, 5670(07):87–184, 2008.

[21] D Sayre. Some implications of a theorem due to Shannon. Acta Crystallographica, page 843, 1952.

[22] D Sayre. Imaging Processes and Coherence in Physics. Springer, Berlin, 1980.

[23] J R Fienup. Reconstruction of an object from the modulus of its Fourier transform. Optics Letters, 3(1):27, July 1978.

[24] R H T Bates. Fourier phase problems are uniquely solvable in mute than one dimension. I: Underlying theory. Optik, 62(3):247–262, 1982.

[25] J R Fienup. Phase retrieval algorithms: a comparison. Applied optics, 21(15):2758–69, August 1982.

[26] Veit Elser. Phase retrieval by iterated projections. Journal of the Optical Society of America. A, Optics, image science, and vision, 20(1):40–55, January 2003.

[27] Bosheng Zhang, Matthew D. Seaberg, Daniel E. Adams, Dennis F. Gardner, Elisabeth R. Shanblatt, Justin M. Shaw, Weilun Chao, Eric M. Gullikson, Farhad Salmassi, Henry C. Kapteyn, and Margaret M. Murnane. Full field tabletop EUV coherent diffractive imaging in a transmission geometry. Optics Express, 21(19):21970, September 2013.

[28] David Shapiro, Pierre Thibault, Tobias Beetz, Veit Elser, Malcolm Howells, Chris Jacobsen, Janos Kirz, Enju Lima, Huijie Miao, Aaron M Neiman, and David Sayre. Biological imaging by soft x-ray diffraction microscopy. Proceedings of the National Academy of Sciences of the United States of America, 102(43):15343–15346, October 2005.

[29] Jianwei Miao, Tetsuya Ishikawa, Qun Shen, and Thomas Earnest. Extending X-ray crystallography to allow the imaging of noncrystalline materials, cells, and single protein complexes. Annual review of physical chemistry, 59:387–410, January 2008.

[30] I. Robinson, I. Vartanyants, G. Williams, M. Pfeifer, and J. Pitney. Reconstruction of the Shapes of Gold Nanocrystals Using Coherent X-Ray Diffraction. Physical Review Letters, 87(19):195505, October 2001.

[31] G. Williams, M. Pfeifer, I. Vartanyants, and I. Robinson. Three-Dimensional Imaging of Microstructure in Au Nanocrystals. Physical Review Letters, 90(17):175501, April 2003.

[32] Mark A Pfeifer, Garth J Williams, Ivan A Vartanyants, Ross Harder, and Ian K Robinson. Three-dimensional mapping of a deformation field inside a nanocrystal. Nature, 442(7098):63–6, July 2006.

[33] Brian Abbey, Garth J. Williams, Mark A. Pfeifer, Jesse N. Clark, Corey T. Putkunz, Angela Torrance, Ian McNulty, T. M. Levin, Andrew G. Peele, and Keith A Nugent. Quantitative coherent diffractive imaging of an integrated circuit at a spatial resolution of 20 nm. Applied Physics Letters, 93(21):214101, 2008.

[34] W Hoppe. Diffraction in inhomogeneous primary wave fields. 1. Principle of phase determination from electron diffraction interference. Acta. Crystallogr. A, 25:495–501, 1969.

[35] W Hoppe and G Strube. Diffraction in inhomogeneous primary wave fields. 2. optical experiments for phasedetermination of lattice interferences. Acta Crystallographica Section A Foundations of Crystallography, 25:502–507, 1969.

[36] W Hoppe. Diffraction in inhomogeneous primary wave fields. 3. amplitude and phase determination for nonperiodic objects. Acta Crystallogr. A, 25:508–515, 1969.

[37] Reiner Hegerl and W Hoppe. Dynamische theorie der kristallstrukturanalyse durch elektronenbeugung im inhomogenen prim{ä}rstrahlwellenfeld. Berichte der Bunsengesellschaft f{ü}r physikalische Chemie, 74(11):1148–1154, 1970.

[38] R Hegerl and W Hoppe. Phase evaluation in generalized diffraction (ptychography). Proc. Fifth Eur. Cong. Electron Microscopy, pages 628–629, 1972.

[39] Henry N. Chapman. Phase-retrieval X-ray microscopy by Wigner-distribution deconvolution. Ultramicroscopy, 66(3-4):153–172, December 1996.

[40] H. Faulkner and J. Rodenburg. Movable Aperture Lensless Transmission Microscopy: A Novel Phase Retrieval Algorithm. Physical Review Letters, 93(2):023903, July 2004.

[41] J. M. Rodenburg and H. M. L. Faulkner. A phase retrieval algorithm for shifting illumination. Applied Physics Letters, 85(20):4795, 2004.

[42] Pierre Thibault, Martin Dierolf, Andreas Menzel, Oliver Bunk, Christian David, and Franz Pfeiffer. High-resolution scanning x-ray diffraction microscopy. Science (New York, N.Y.), 321(5887):379–82, July 2008.

[43] J. M. Rodenburg. Ptychography: early history and 3D scattering effects. In Davide Bleiner, editor, Proc. of SPIE, volume 8678, page 867809, December 2012.

[44] Matthew D. Seaberg, Bosheng Zhang, Dennis F. Gardner, Elisabeth R. Shanblatt, Margaret M. Murnane, Henry C. Kapteyn, and Daniel E. Adams. Tabletop nanometer extreme ultraviolet imaging in an extended reflection mode using coherent Fresnel ptychography. Optica, 1(1):39, July 2014.

[45] Joseph W Goodman. Introduction to Fourier Optics. McGraw-Hill physical and quantum electronics series. McGraw-Hill, 2nd edition, 1996.

[46] J D Jackson. Classical Electrodynamics. Wiley, 1998.

[47] S Celozzi, R Araneo, and G Lovat. Electromagnetic Shielding. Wiley Series in Microwave and Optical Engineering. Wiley, 2008.

[48] J. Stratton and L. Chu. Diffraction Theory of Electromagnetic Waves. Physical Review, 56(1):99–107, July 1939.

[49] S. Schelkunoff. On Diffraction and Radiation of Electromagnetic Waves. Physical Review, 56(4):308–316, August 1939.

[50] WR Smythe. The Double Current Sheet in Diffraction. Physical Review, 72(11):1066–1070, December 1947.

[51] S. A. Schelkunoff. Some Equivalence Theorems of Electromagnetics and Their Application to Radiation Problems. Bell System Technical Journal, 15(1):92–112, January 1936.

[52] Henry N Chapman, Anton Barty, Stefano Marchesini, Aleksandr Noy, Stefan P Hau-Riege, Congwu Cui, Malcolm R Howells, Rachel Rosen, Haifeng He, John C H Spence, Uwe Weierstall, Tobias Beetz, Chris Jacobsen, and David Shapiro. High-resolution ab initio three-dimensional x-ray diffraction microscopy. Journal of the Optical Society of America. A, Optics, image science, and vision, 23(5):1179–200, May 2006.

[53] Martin Dierolf, Andreas Menzel, Pierre Thibault, Philipp Schneider, Cameron M Kewish, Roger Wepf, Oliver Bunk, and Franz Pfeiffer. Ptychographic X-ray computed tomography at the nanoscale. Nature, 467(7314):436–9, September 2010.

[54] M Holler, a Diaz, M Guizar-Sicairos, P Karvinen, Elina Färm, Emma Härkönen, Mikko Ritala, a Menzel, J Raabe, and O Bunk. X-ray ptychographic computed tomography at 16 nm isotropic 3D resolution. Scientific reports, 4:3857, January 2014.

[55] S. Marchesini, H. He, H. N. Chapman, S. P. Hau-Riege, A. Noy, M. R. Howells, U. Weierstall, and J. C. H. Spence. X-ray image reconstruction from a diffraction pattern alone. Physical Review B, 68(14):140101, October 2003.

[56] Andrew M Maiden and John M Rodenburg. An improved ptychographical phase retrieval algorithm for diffractive imaging. Ultramicroscopy, 109(10):1256–62, September 2009.

[57] D Russell Luke. Relaxed averaged alternating reflections for diffraction imaging. Inverse Problems, 21(1):37–50, February 2005.

[58] S Marchesini. Invited article: a unified evaluation of iterative projection algorithms for phase retrieval. The Review of scientific instruments, 78(1):011301, January 2007.

[59] Dennis F Gardner, Bosheng Zhang, Matthew D Seaberg, Leigh S Martin, Daniel E Adams, Farhad Salmassi, Eric Gullikson, Henry Kapteyn, and Margaret Murnane. High numerical aperture reflection mode coherent diffraction microscopy using off-axis apertured illumination. Optics Express, 20(17):19050–9, August 2012.

[60] Bosheng Zhang, Matthew D. Seaberg, Daniel E. Adams, Henry C. Kapteyn, and Margaret M. Murnane. Coherent diffractive imaging with arbitrary angle of incidence. Patent US 62/043,132 (Provisional), 2014.

[61] J. Rodenburg, A. Hurst, A. Cullis, B. Dobson, F. Pfeiffer, O. Bunk, C. David, K. Jefimovs, and I. Johnson. Hard-X-Ray Lensless Imaging of Extended Objects. Physical Review Letters, 98(3):034801, January 2007.

[62] Brian Abbey, Keith A. Nugent, Garth J. Williams, Jesse N. Clark, Andrew G. Peele, Mark A. Pfeifer, Martin de Jonge, and Ian McNulty. Keyhole coherent diffractive imaging. Nature Physics, 4(5):394–398, March 2008.

[63] G. Williams, H. Quiney, B. Dhal, C. Tran, K. Nugent, a. Peele, D. Paterson, and M. de Jonge. Fresnel Coherent Diffractive Imaging. Physical Review Letters, 97(2):025506, July 2006.

[64] J C H Spence, U Weierstall, and M Howells. Coherence and sampling requirements for diffractive imaging. Ultramicroscopy, 101(2-4):149–52, November 2004.

[65] H M Quiney, K A Nugent, and A G Peele. Iterative image reconstruction algorithms using wave-front intensity and phase variation. Optics letters, 30(13):1638–40, July 2005.

[66] Daniel E Adams, Leigh S Martin, Matthew D Seaberg, Dennis F Gardner, Henry C Kapteyn, and Margaret M Murnane. A generalization for optimized phase retrieval algorithms. Optics Express, 20(22):24778–90, October 2012.

[67] Max Born and Emil Wolf. Principles of Optics. null. Cambridge University Press, 7th edition, 1999.

[68] Janos Kirz. Phase zone plates for x rays and the extreme uv. Journal of the Optical Society of America, 64(3):301, March 1974.

[69] H. M. Quiney, A. G. Peele, Z. Cai, D. Paterson, and K. A. Nugent. Diffractive imaging of highly focused X-ray fields. Nature Physics, 2(2):101–104, January 2006.

[70] H J Kreuzer, M J Jericho, I A Meinertzhagen, and Wenbo Xu. Digital in-line holography with photons and electrons. Journal of Physics: Condensed Matter, 13(47):10729–10741, November 2001.

[71] Gabriel Koren, François Polack, and Denis Joyeux. Iterative algorithms for twin-image elimination in in-line holography using finite-support constraints. Journal of the Optical Society of America A, 10(3):423–433, March 1993.

[72] B.L. Henke, E.M. Gullikson, and J.C. Davis. X-Ray Interactions: Photoabsorption, Scattering, Transmission, and Reflection at E = 50-30,000 eV, Z = 1-92. Atomic Data and Nuclear Data Tables, 54(2):181–342, July 1993.

[73] Mark E Siemens, Qing Li, Ronggui Yang, Keith A Nelson, Erik H Anderson, Margaret M Murnane, and Henry C Kapteyn. Quasi-ballistic thermal transport from nanoscale interfaces observed using ultrafast coherent soft X-ray beams. Nature materials, 9(1):26–30, January 2010.

[74] Damiano Nardi, Marco Travagliati, Mark E Siemens, Qing Li, Margaret M Murnane, Henry C Kapteyn, Gabriele Ferrini, Fulvio Parmigiani, and Francesco Banfi. Probing thermomechanics at the nanoscale: impulsively excited pseudosurface acoustic waves in hypersonic phononic crystals. Nano letters, 11(10):4126–33, October 2011.

[75] Stefan Mathias, Chan La-O-Vorakiat, Patrik Grychtol, Patrick Granitzka, Emrah Turgut, Justin M Shaw, Roman Adam, Hans T Nembach, Mark E Siemens, Steffen Eich, Claus M Schneider, Thomas J Silva, Martin Aeschlimann, Margaret M Murnane, and Henry C Kapteyn. Probing the timescale of the exchange interaction in a ferromagnetic alloy. Proceedings of the National Academy of Sciences of the United States of America, 109(13):4792–7, March 2012.

[76] Tetsuo Harada, Masato Nakasuji, Yutaka Nagata, Takeo Watanabe, and Hiroo Kinoshita. Phase Imaging of Extreme-Ultraviolet Mask Using Coherent Extreme-Ultraviolet Scatterometry Microscope. Japanese Journal of Applied Physics, 52(6S):06GB02, June 2013.

[77] S Roy, D Parks, K A Seu, R Su, J J Turner, W Chao, E H Anderson, S Cabrini, and S D Kevan. Lensless X-ray imaging in reflection geometry. Nature Photonics, 5(April):243–245, 2011.

[78] Michael Zürch, Christian Kern, and Christian Spielmann. XUV coherent diffraction imaging in reflection geometry with low numerical aperture. Optics express, 4(May):118–123, 2013.

[79] Tao Sun, Zhang Jiang, Joseph Strzalka, Leonidas Ocola, and Jin Wang. Three-dimensional coherent X-ray surface scattering imaging near total external reflection. Nature Photonics, 6(September):586–590, 2012.

[80] D. J. Vine, G. J. Williams, B. Abbey, M. A. Pfeifer, J. N. Clark, M. D. de Jonge, I. McNulty, A. G. Peele, and K. A. Nugent. Ptychographic Fresnel coherent diffractive imaging. Physical Review A, 80(6):063823, December 2009.

[81] Fucai Zhang, Isaac Peterson, Joan Vila-Comamala, Ana Diaz, Felisa Berenguer, Richard Bean, Bo Chen, Andreas Menzel, Ian K Robinson, and John M Rodenburg. Translation position determination in ptychographic coherent diffraction imaging. Optics express, 21(11):13592–606, June 2013.

[82] Stefan Mathias, Chan La-o vorakiat, Justin M. Shaw, Emrah Turgut, Patrik Grychtol, Roman Adam, Dennis Rudolf, Hans T. Nembach, Thomas J. Silva, Martin Aeschlimann, Claus M. Schneider, Henry C. Kapteyn, and Margaret M. Murnane. Ultrafast element-specific magnetization dynamics of complex magnetic materials on a table-top. Journal of Electron Spectroscopy and Related Phenomena, 189(2013):164–170, August 2013.

[83] Pierre Thibault, Martin Dierolf, Oliver Bunk, Andreas Menzel, and Franz Pfeiffer. Probe retrieval in ptychographic coherent diffractive imaging. Ultramicroscopy, 109(4):338–43, March 2009.

[84] Andrew M Maiden, Martin J Humphry, Fucai Zhang, and John M Rodenburg. Superresolution imaging via ptychography. Journal of the Optical Society of America. A, Optics, image science, and vision, 28(4):604–12, April 2011.

[85] Toshiaki Ohtsuka, M Masuda, and N Sato. Ellipsometric study of anodic oxide films on titanium in hydrochloric acid, sulfuric acid, and phosphate solution. Journal of The Electrochemical Society, 132(4):787, 1985.

[86] Maria Advincula, Xiaowu Fan, Jack Lemons, and Rigoberto Advincula. Surface modification of surface sol-gel derived titanium oxide films by self-assembled monolayers (SAMs) and nonspecific protein adsorption studies. Colloids and surfaces. B, Biointerfaces, 42(1):29–43, April 2005.

[87] Darren J Batey, Daniel Claus, and John M Rodenburg. Information multiplexing in ptychography. Ultramicroscopy, 138:13–21, March 2014.

[88] R N Wilke, M Priebe, M Bartels, K Giewekemeyer, A Diaz, P Karvinen, and T Salditt. Hard X-ray imaging of bacterial cells: nano-diffraction and ptychographic reconstruction. Optics express, 20(17):19232–54, August 2012.

[89] Pierre Thibault and Andreas Menzel. Reconstructing state mixtures from diffraction measurements. Nature, 494(7435):68–71, February 2013.

[90] Qing Li, Kathleen Hoogeboom-Pot, Damiano Nardi, Margaret M. Murnane, Henry C. Kapteyn, Mark E. Siemens, Erik H. Anderson, Olav Hellwig, Elizabeth Dobisz, Bruce Gurney, Ronggui Yang, and Keith a. Nelson. Generation and control of ultrashort-wavelength two-dimensional surface acoustic waves at nanoscale interfaces. Physical Review B, 85(19):195431, May 2012.

[91] Chan La-O-Vorakiat, Mark Siemens, Margaret M Murnane, Henry C Kapteyn, Patrik Grychtol, Roman Adam, Claus M Schneider, Justin M Shaw, Hans Nembach, and T J Silva. Ultrafast Demagnetization Dynamics at the M Edges of Magnetic Elements Observed Using a Tabletop High-Harmonic Soft X-Ray Source. Physical Review Letters, 103(25):257402, December 2009.

[92] Emrah Turgut, Chan La-o vorakiat, Justin M. Shaw, Patrik Grychtol, Hans T. Nembach, Dennis Rudolf, Roman Adam, Martin Aeschlimann, Claus M. Schneider, Thomas J. Silva,

Margaret M. Murnane, Henry C. Kapteyn, and Stefan Mathias. Controlling the Competition between Optically Induced Ultrafast Spin-Flip Scattering and Spin Transport in Magnetic Multilayers. Physical Review Letters, 110(19):197201, May 2013.

[93] Henry N. Chapman, Anton Barty, Michael J. Bogan, Sébastien Boutet, Matthias Frank, Stefan P. Hau-Riege, Stefano Marchesini, Bruce W. Woods, Saša Bajt, W. Henry Benner, Richard A. London, Elke Plönjes, Marion Kuhlmann, Rolf Treusch, Stefan Düsterer, Thomas Tschentscher, Jochen R. Schneider, Eberhard Spiller, Thomas Möller, Christoph Bostedt, Matthias Hoener, David a. Shapiro, Keith O. Hodgson, David van der Spoel, Florian Burmeister, Magnus Bergh, Carl Caleman, Gösta Huldt, M. Marvin Seibert, Filipe R. N. C. Maia, Richard W. Lee, Abraham Szöke, Nicusor Timneanu, and Janos Hajdu. Femtosecond diffractive imaging with a soft-X-ray free-electron laser. Nature Physics, 2(12):839–843, November 2006.

[94] Rui Xu, Huaidong Jiang, Changyong Song, Jose a Rodriguez, Zhifeng Huang, Chien-Chun Chen, Daewoong Nam, Jaehyun Park, Marcus Gallagher-Jones, Sangsoo Kim, Sunam Kim, Akihiro Suzuki, Yuki Takayama, Tomotaka Oroguchi, Yukio Takahashi, Jiadong Fan, Yunfei Zou, Takaki Hatsui, Yuichi Inubushi, Takashi Kameshima, Koji Yonekura, Kensuke Tono, Tadashi Togashi, Takahiro Sato, Masaki Yamamoto, Masayoshi Nakasako, Makina Yabashi, Tetsuya Ishikawa, and Jianwei Miao. Single-shot three-dimensional structure determination of nanocrystals with femtosecond X-ray free-electron laser pulses. Nature communications, 5(May):4061, January 2014.

[95] a. Ravasio, D. Gauthier, F. Maia, M. Billon, J-P. Caumes, D. Garzella, M. Géléoc, O. Gobert, J-F. Hergott, a M. Pena, H. Perez, B. Carré, E. Bourhis, J. Gierak, a. Madouri, D. Mailly, B. Schiedt, M. Fajardo, J. Gautier, P. Zeitoun, P. Bucksbaum, J. Hajdu, and H. Merdji. Single-Shot Diffractive Imaging with a Table-Top Femtosecond Soft X-Ray Laser-Harmonics Source. Physical Review Letters, 103(2):028104, July 2009.

[96] Hugh T Philipp, Kartik Ayyer, Mark W Tate, Veit Elser, and Sol M Gruner. Solving structure with sparse, randomly-oriented x-ray data. Optics express, 20(12):13129–37, June 2012.

[97] S Eisebitt, J Lüning, W F Schlotter, M Lörgen, O Hellwig, W Eberhardt, and J Stöhr. Lensless imaging of magnetic nanostructures by X-ray spectro-holography. Nature, 432(7019):885–8, December 2004.